AN ABSTRACT OF THE THESIS OF

Roger West Brownlow for the degree of DOCTOR OF PHILOSOPHY

in MECHANICAL ENGINEERING presented on August 12, 1976

Title: WIND TUNNEL SIMULATION AND FIELD MEASUREMENTS OF FLOW OVER A COASTAL HEADLAND

Redacted for Privacy

Abstract approved: Robert E. Wilson

An experimental study was made of the average and turbulent wind characteristics of the flow over a model of a coastal headland. The scale of the model was 300:1, corresponding to a prototype size of 500 m.

The data for validation of the model study was obtained from instruments mounted on a 27.5 m tower constructed on the headland, Yaquina Head, for this experiment. Comparison is presented of average and turbulent flow characteristics over the model and the prototype under the conditions of neutral stability and wind velocities greater than 600 cm/s. The similarity of the two average velocity profiles was used to demonstrate that the model flow represented the prototype flow.

This has offered new information on scaling relations of similarity parameters necessary for wind tunnel terrain model flow studies.

Wind Tunnel Simulation and Field Measurements of Flow over a Coastal Headland

by

Roger West Brownlow

A THESIS

submitted to

Oregon State University

in partial fulfillment of
the requirements for the
degree of

Doctor of Philosophy

Completed August 1976

Commencement June 1977

APPROVED:

Redacted for Privacy

Professor of Mechanical Engineering

in charge of major

Redacted for Privacy

Head of Department of Mechanical Engineering

Redacted for Privacy

Dean of Graduate School

Date thesis is presented August 12, 1976

Typed by Clover Redfern for Roger West Brownlow

ACKNOWLEDGMENT

This research has been made possible through the help and encouragement of several people. Dr. Robert Wilson has shown great patience while providing advice and encouragement.

Dr. E. W. Hewson has supported my experimental work with meteorology equipment and technical help.

My wife, Doris, has provided that moral support so necessary for achievement.

Many other people contributed ideas and assistance to me while my work was in progress. Among them are my fellow students in the Mechanical Engineering Department, the Atmospheric Sciences Department, and the School of Oceanography.

Funds, which in part covered the costs of this investigation, were provided by the four Oregon Peoples Utility Districts of Central Lincoln, Tillamook, Clatskanie, and Northern Wasco County through the Oregon P. U. D. Directors' Association.

TABLE OF CONTENTS

Page

LIST OF FIGURES

LIST OF TABLES

NOMENCLATURE

Symbol	
A	Control surface area
C_{ij}	Correlation coefficient
C_v	Specific heat at constant volume
C_p	Specific heat at constant pressure
e	Energy
Ec	Eckert number
Eu	Euler number
f	Frequency - hertz
Fr	Froude number
$F(K/K_s)$	Universal spectral function for velocity
g	Body force, i.e., gravitational, magnetic, etc.
h	A reference height
H	Average heat flux
K_T	Thermal conductivity
K	Radian wave number
k	Von Karman constant
$\underline{K}$	Unit vector
L	Characteristic length
$\underline{n}$	Unit vector
$p = \overline{P} + p'$	Pressure - instantaneous and mean values
Pa	Pascal - stress

Pr	Prandtl number
Q	Total heat transfer
R	Ideal gas constant
R_c	Correlation function
Ro	Rossby number
Ri	Gradient Richardson number
Re	Reynolds number
Ri	Richardson number
S + s	Mean and fluctuating rate of strain
$T = T + T'$	Temperature - Instantaneous and mean values
T^*	Dimensionless form
t	Time
T_{ij}	Reynolds stress tensor
u_*	Friction velocity
$U_i = \overline{U}_i + u_i'$	Velocity Instantaneous and mean values
$\underline{U} = \underline{\overline{U}} + \underline{u}'$	Vector form
$U_i^* = \overline{U}_i^* + u_i^*$	Dimensionless form
V, v	Lateral velocity or velocity
V_L	Volume
w	Vertical velocity
x	Longitudinal distance and coordinate
y	Lateral distance and coordinate
z	Distance perpendicular to boundary and coordinate

Greek Symbols

α	Constant
β	Probability density function
ϵ	Turbulent energy
γ	Specific weight
γ	Specific heat ratio
δ_{ij}	Kronecker delta
Γ	Lapse rate
μ	Dynamic viscosity
θ	Potential temperature
ν	Kinematic viscosity
ρ	Density
τ	Wall shear stress
ω	Angular velocity or frequency
$\phi(\omega), \phi(K)$	Power spectral density

Subscripts

$(\ )_i$	i = 1, 2, 3 refer to longitudinal, lateral, vertical vector components
$(\ )_o$	Reference value
$(\ )_w$	Wall value
$\underline{(\ )}$	Vector
$(\ )_\infty$	Free stream conditions

Superscripts

$(\ )^*$	Dimensionless with respect to some scaling parameter
$\overline{(\ )}$	Time averaged
$(\ )^n$, $(\ )^m$	Sample number

WIND TUNNEL SIMULATION AND FIELD MEASUREMENTS OF FLOW OVER A COASTAL HEADLAND

I. INTRODUCTION

Recent interest in alternate sources of energy has increased research related activity in using wind as a power source. Research that has been completed prior to 1956 is carefully detailed by Golding (21) with an update presented by Hewson (24). Golding has pointed out that research and development fall into two general areas:

a. Construction and operation of the wind driven generators

b. Wind behavior in the region of wind driven generators.

This experiment applies to the area of wind behavior. The objective will be to predict, from a wind tunnel model, the wind speed in the atmospheric boundary layer as it moves over a coastal headland.

Theoretical Studies of Atmospheric Boundary Layer Flow

Observing the velocity at one elevation and predicting its value at a higher elevation in the boundary layer supplies useful information on wind forces on structures. The bibliography contains several references beginning with the exponential relation of Archibald (2) in 1883 and continuing with the logarithmic models of Hellman (23), Paeschke (32), Georgii (17), and the mixing length model of Prandtl (40). Each model is restricted to a limited range of flow conditions, while the thrust of the development is toward a general relation covering all flow conditions. Using the Reynolds shearing stress, τ, the friction velocity, $u_*^2 = |\tau/\rho|$, and a roughness reference length, Z_o, in Prandtl's equation, we obtain a relation as follows:

$$\frac{u}{u_*} = \frac{1}{k} \ln(\frac{z}{Z_o}) \qquad (1.1)$$

This equation was used by Ruggles (42) in the analysis of velocity data taken over a period of two months on a spar mounted over the Atlantic Ocean, off the coast of New England. Measurements were made at 1 m, 2 m, 5 m, and 10 m and fitted to the equation. Correlation coefficients of the fit of the data to equation (1.1) were determined. Criterion for satisfactory fitting of a logarithmic profile is a correlation greater than 0.94. Of approximately 300 mean wind profiles, greater than 90% fit equation (1.1).

The development of mean velocity prediction has included consideration of surface roughness and turbulence. Many attempts to include the variations in velocity due to thermal effects resulted in the Monin-Obukhov (29) equation:

$$u = \frac{u_*}{k} (\ln \frac{z}{Z_o} + \alpha \frac{z}{L}) \qquad (1.2)$$

The temperature effect is contained in the Monin-Obukhov length:

$$L = -\frac{\rho u_*^3 C_p T}{kgH} \tag{1.3}$$

The effect of the $\alpha(z/L)$ term is significant for superadiabatic conditions. For heights up to 50 m, the superadiabatic wind profiles do not differ greatly from adiabatic profiles (51), so that $\alpha(z/L) \ll \ln(z/Z_o)$ and is ignored up to 50m above the ground.

The validity of the mixing length hypothesis used in equation (1.1) is based on two postulates (47):

1. That the exchange coefficient involves a unique representative length and a representative fluctuating velocity.
2. That the length introduced is proportional to the quotient of the fluctuating velocity and the gradient of the mean velocity.

Batchelor (3) has pointed out that postulate (2) is equivalent to the assumption that the turbulence has a similar structure at all points in the field and that there is no diffusion of turbulent energy. A more realistic analysis of turbulent energy effects was necessary.

Continuing along a line of immediate import to this experiment is what is commonly called the change of terrain problem. This is similar to the transition problem of aerodynamics. The latter problem concerns transition from laminar to turbulent flow. The former problem is on transition of one turbulent structure to another, as indicated by Batchelor. In either case the average velocity profile is affected. The statistical theory of turbulence was well developed by Taylor (48) as early as 1935. Its application to observations in the atmosphere was delayed until the development of turbulence measuring, encoding, and data processing systems. Pioneering effort in the change of terrain problem was initiated by Elliott (13) who used a similarity method. Essentially, Elliott used equation (1.1) for the velocity profile both before and after the terrain roughness change. The difference in the two conditions being the shear velocity and the roughness length. Experiments in the neutral atmospheric boundary layer were made by Bradley (7) to verify Elliott's method. Only rough agreement was found. A criticism of Elliott's model is the sudden change in shear velocity at the surface roughness change. Several attempts to improve Elliott's model by including exchange coefficients were made. These were only slightly better in matching Bradley's observed data. Petersen (34) proposed that stress was proportional to turbulent energy. His theory postulates the flow to be governed primarily by the dominant terms of the horizontal-momentum, continuity, and turbulent energy equations. An important difference in Petersen's analysis from previous theories is that the predicted transition velocity-profiles contain an inflection point. Attempts to verify the theory with observed wind profiles were made by Petersen and Taylor (35). The observed profiles contain inflection points also, however, Petersen's theory did not exactly match these points. Failure of the theory was believed due to the fact that the model neglected dynamic pressure effects. What has been demonstrated here is the present trend of the theory on predicting turbulent flow. The theory has started with the first-order closure or mean-velocity-field closure expressing Reynolds stresses as functions of the mean velocity field as in the mixing length or eddy viscosity formulae. The publications of Petersen (34, 37) and Wyngaard et al. (55, 56) are examples of second order closure or Reynolds stress closure. This illustrates the essence of the problem of calculating turbulent shear flows. The calculation of turbulent shear flow requires an empirical representation of the Reynolds shear stress. The only alternative to this approach is a direct solution of the time dependent, three-dimensional Navier-Stokes equation which is, at present, beyond the capacity of even the largest computers (8). Shir (45) extended Petersen's method by implicitly treating pressure gradient and the vertical equation of motion through the vorticity equation. This method matched Bradley's observations better than Petersen's, especially in the rough to smooth transition.

The more complicated mean-turbulent-field closure has two subsets. One being the turbulent energy closure, similar to Bradshaw (8), and the other the Reynold's stress closure. All these techniques were summarized by Bradshaw (8). The Reynolds stress closure is the most recent and most complicated of the methods in use. This requires the solution of a differential equation for each component of the Reynolds stress tensor. This technique has only been possible with advances in computer technology. The application of the Reynolds stress closure to data in the atmospheric boundary layer for accuracy of prediction has been reported by Wyngaard (55). Prediction of the structure of turbulence from neutral to moderately stable stratification was considered successful as applied to the 1968 Kansas and the 1973 Minnesota data. Progress in the development of this technique has been summarized by Launder et al. (26).

Wind Surveys

The fact that wind power is proportional to the cube of velocity places accuracy of information of wind velocity characteristics at a particular site location in a position of prime importance.

The effect of pressure, density, and motion of the earth on the atmosphere is well known. This knowledge allows prediction of prevailing wind direction in many parts of the world with some confidence. Cyclonic depressions are superposed on the general system of atmospheric pressure to obscure these prevailing directions, however, continuous records show the general tendency of this behavior above approximately 500 meters. Below 500 meters, the wind is greatly influenced by topography, vegetation, and local temperature variations. It is for this reason that wind surveys are important to the success of wind as a power source since each site has unique characteristics influencing the wind in a very complex manner.

A short review of large scale wind surveys will indicate their complexity and resulting high costs. At the same time, the factors that are important to the model studies of wind flow will become more apparent.

The earliest large scale wind survey for a power source was by Putman (42). Preliminary estimates of wind velocities were computed as an aid in planning the installation of anemometers. Using the daily weather survey maps, a gradient wind was computed from the isobars. Making some arbitrary allowance for frictional effects, a velocity distribution was then estimated between the ground and the gradient wind level. Based on these estimates and theories on acceleration of wind flowing over crests, a topography was chosen that was thought to have a speed-up or acceleration of at least 1.2. A total of 20 anemometer towers were constructed around the area of interest. Anemometers were located between 12 meters and 56 meters above ground, depending on vegetation and the specific information required. These were operated for periods of 22 days to 1733 days, at the generator site. The large number of locations was necessary to survey the prevailing approach flow to the site as well as the site itself. The objective was to locate a site that yielded the maximum wind energy. The actual values of wind velocity indicated an acceleration factor of 0.9 rather than the estimated value of 1.2. A more careful analysis of the prevailing flows indicated turbulence generated in the approach flow could be the only unknown not considered in the estimates. This has been the factor dominating the theoretical models mentioned previously.

The second large scale wind survey for wind power sites was conducted by Électricité de France and reported by Aillevet (1). A total of 150 instruments were located at various sites throughout France at altitudes from 1 m to 1912 m. The results of this survey indicated more knowledge was necessary on variation of wind speed with height over flat ground and over various topographic configurations.

The third survey series was reported by Golding (21). Much of the report concentrates on velocity profile variations over the surface of hills. These profiles were found to be directly related to the approach flow and contour of the hill.

The fourth survey was reported by Frenkiel (15). Two sites were selected that reflected the results of a three year survey. These sites fitted into two broad topographically attractive categories suitable for large scale generation of electricity by wind power:

a. a mountain ridge athwart the prevailing wind direction with a steep leeward side, and

b. an isolated peak in a valley in the general direction of prevailing winds.

Frenkiel found that the isolated peak had a higher power potential than the ridge. He postulates that this is due to uniform slopes in all wind directions with an incline of 16° in the nearest few hundred meters from the hill top.

The final survey is that reported by Hewson (22). Based on the fact that the western coast of the North American continent is exposed to a strong prevailing wind pattern, as pointed out by Bourke et al. (6), a survey was initiated in Oregon by Hewson in 1971. In addition to the established wind stations, seven more stations were installed on mountain peaks and ridges near the coast and coastal headlands extending into the ocean with exposure to the full ocean surface prevailing wind. Yaquina Head is one of these stations. A topographic map, Figure 1.1, shows the extent of exposure to the predominantly northerly summer winds and southerly winter winds (6). The summary of the frequency distributions of speed and aximuth on Yaquina Head between January 1973 and July 1975 is given in Appendix C. Details on the survey at other sites is in reference (25).

Model Studies of Atmospheric Boundary Layer Flow

One of the early successful terrain model studies in a wind tunnel was a study of winds around the Rock of Gibralter (14). Fine

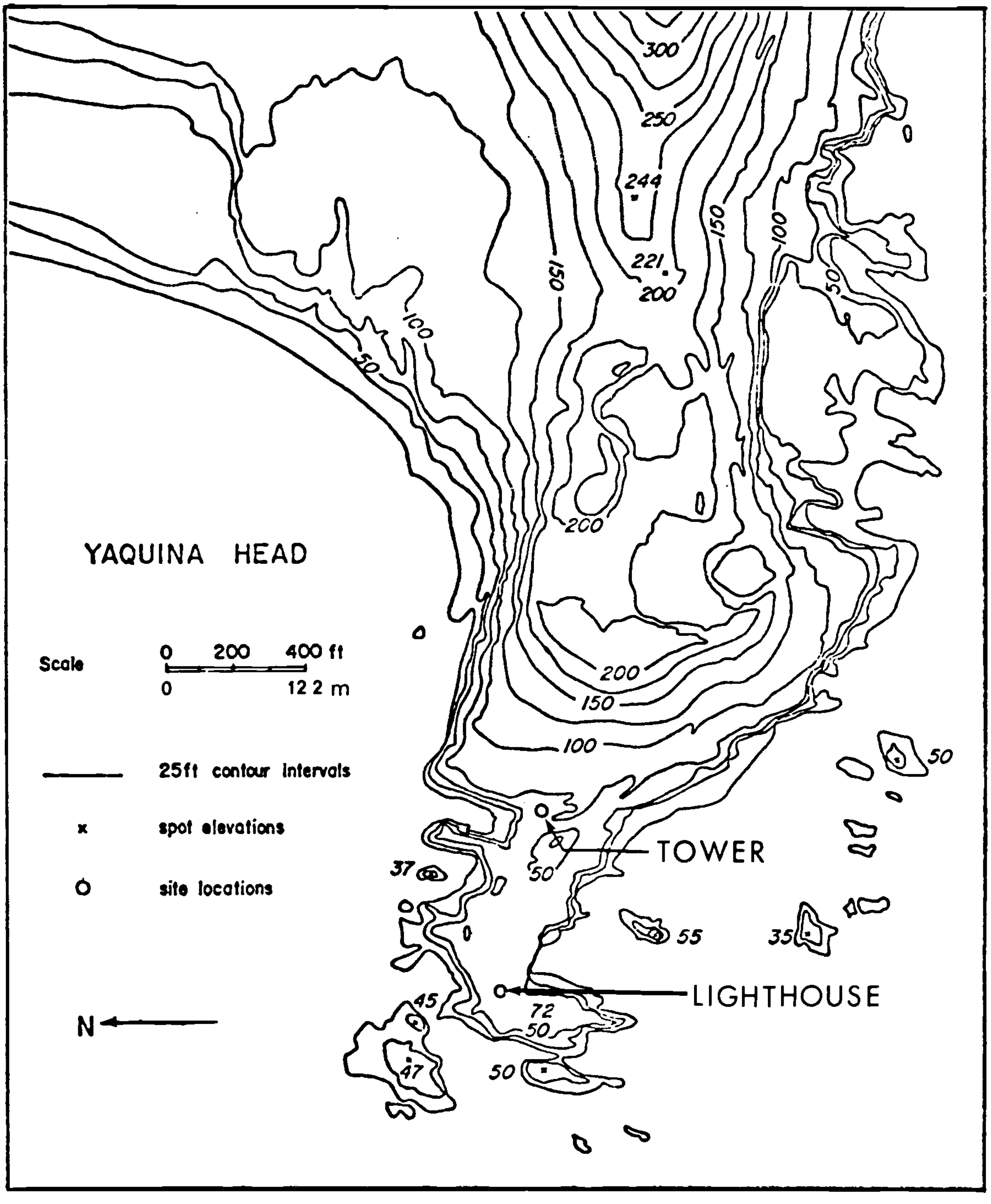

Figure 1. 1. Topographic map of Yaquina Head showing the location of the test tower for this experiment and the lighthouse.

wool fibers were placed so as to allow recording of streamline patterns over the model as wind direction varied from northeast to east to southeast. These were compared to 360 plottings of test balloons released over the prototype. Agreement was found in all but 24 cases.

A wind tunnel model test of mountain terrain was directed by Von Kármán (42) in 1939. Four separate mountains were scaled to a 1:5000 ratio. Although the surfaces of the models included artificial roughness for turbulence effects, there is no indication of simulation of turbulence to the approach and departure conditions of the prototype. It is assumed that thermal gradients were not considered. The main object of this research was to determine average wind velocity gradients over the model surface with the expectation of discovering the location of the maximum velocity. Errors of over 10% between the model predictions and prototype measurements were considered unacceptable for the intended purpose of the research and the work was discontinued.

Advances in instrumentation and the theory of boundary layer flow in the lower atmosphere have considerably improved the capability of predicting wind flow from wind tunnel methods. Success is dependent on strict adherence to the similarity parameters as recommended by Batchelor (4). The conditions for dynamical similarity established by Batchelor consist of atmospheric motions on a scale whose upper limit is of the order of the height of the atmosphere and whose lower limit is about 10 cm. He makes the following assumptions:

a. the Coriolis forces can be ignored,

b. the effects of viscosity and heat conductivity can be ignored,

c. the Mach number of the fluid is everywhere small,

d. the fluid is a perfect gas.

Batchelor then uses the dimensionless momentum, continuity, and energy equations to establish similarity when geometry and Richardson number are similar and the fluid is incompressible: i.e., the boundary layer is less than 100 m. The form of the Richardson number used by Batchelor is called the gradient Richardson number which contains variables that can be measured with relative ease. Batchelor (5) has also indicated the flux Richardson number which is derived from turbulent energy equations as a ratio of buoyant production to stress production of turbulent kinetic energy. If the absolute value of flux Richardson number is small, then it is equal to gradient Richardson number. Turbulence cannot be maintained for flux Richardson numbers greater than $|0.2|$ (50). Gradient Richardson number has been measured in the atmospheric boundary layer under many conditions (27,43). Except for conditions of very low velocity, observed Richardson numbers are generally less than $|0.2|$. This indicates that turbulence similarity is important in model studies at high Reynolds numbers, in addition to the similarity parameter of reference (4). This parameter is geometric similarity.

The measurement and control of turbulence in wind tunnels has been developed extensively (5, 9, 38, 44). Screens, rods and plates of various sizes and spacings can be used to control the turbulence and at the same time thicken the boundary layer. The similarity of velocity spectra in a wind tunnel, in the atmosphere, and in a tidal channel has been demonstrated by Cermak (9) and is shown in Figure 1.2. Additional thickening of the boundary layer is achieved by placing an exaggerated roughness over the first 3 or 4 m of the test section floor. In short tunnels, momentum sinks and vorticity generators are often used to help thicken the boundary layer. Cermak (10) has placed 1 m of coarse roughness then 5 m of fine roughness to obtain the velocity profile similarity shown in Figure 1.3.

Vertical temperature distributions can be controlled (9, 10, 30). The test section floor can be heated or cooled and the ambient air stream can be heated or cooled. An elevated inversion may be obtained by cooling the upwind portion of the test-section floor, heating the downwind portion and heating the ambient air stream during passage through the return flow section (10). Ogawa (30) produced four surface temperature conditions in modeling a sea breeze. These corresponded to neutral, stable, unstable, and elevated inversion

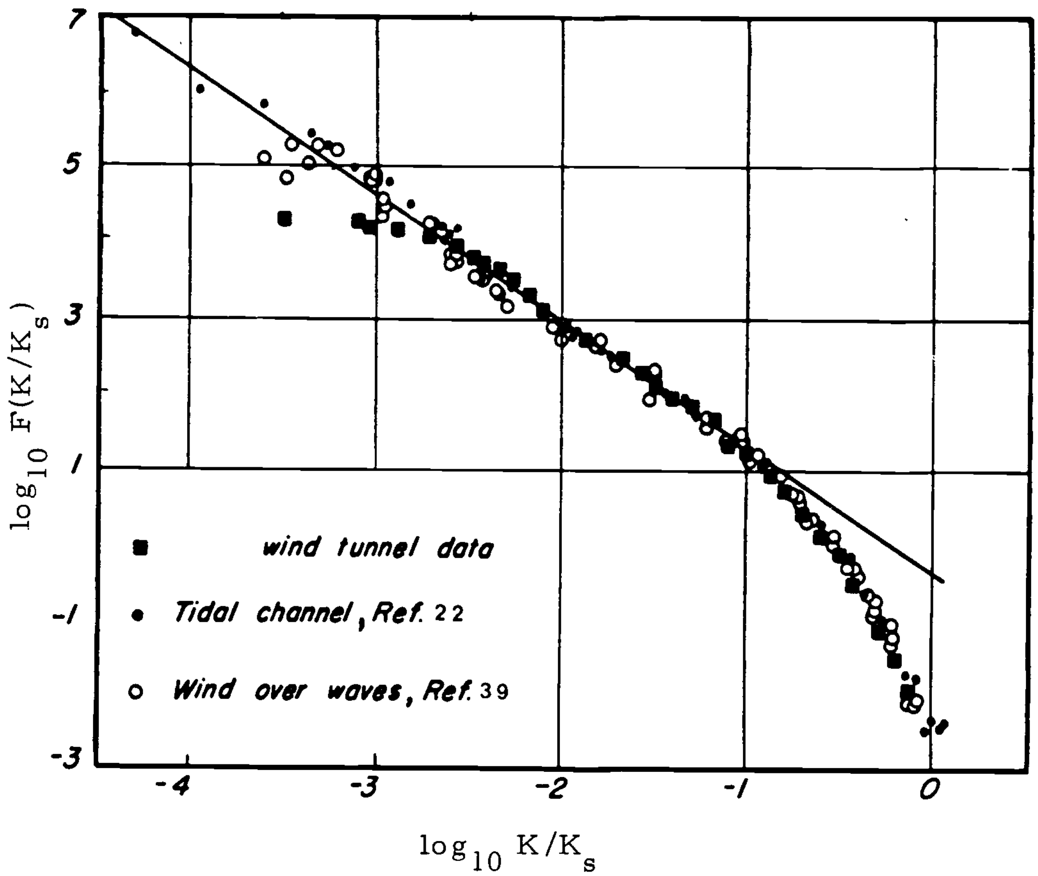

Figure 1.2. Comparison of spectra measurements from a meteorological wind tunnel, an ocean tidal channel and air flow over the sea surface, as reported by Cermak (9).

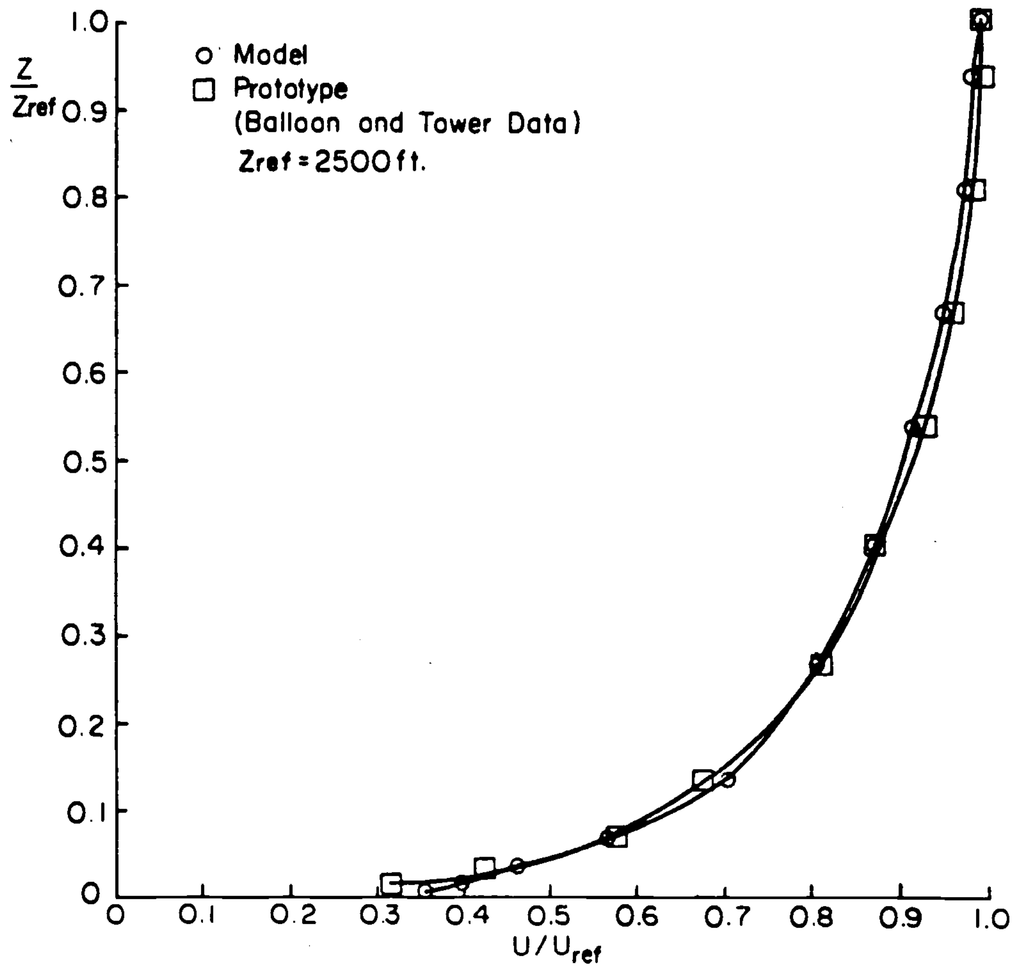

Figure 1. 3. Comparison of model and prototype velocity profiles approaching Fort Wayne, Indiana as reported by Cermak (10).

conditions. This experiment demonstrated the sea breeze effects on diffusion under the four conditions.

Plate (38) has summarized the present state of knowledge of the planetary boundary layer with a series of suggestions for future research. Although he recommends analytical studies associated with aspects of disturbed boundary layers as a general problem, he concludes that the added complexity of special terrain and its features increases the difficulty of analytical treatment to a point that the time and effort expended is no longer in reasonable proportion to the value of information obtained. It is for these complex boundary layer flows that wind-tunnel and actual terrain measurements must be made.

II. OBJECTIVE AND DESCRIPTION OF TEST EQUIPMENT OF PRESENT STUDY

The objective of this research is to predict, from a wind tunnel model, the wind speed in the atmospheric boundary layer as it moves over a coastal headland.

Design of Experiment

The basic similarity conditions necessary for fluid flow models are derived from the continuity, momentum, and energy equations. The atmospheric boundary layer flow over non-homogeneous terrain at high Reynolds numbers generates turbulence. Therefore, a turbulent energy budget equation is required to identify the turbulent flow characteristics necessary for modeling.

The importance of the thermal energy equation in this experiment was carefully considered. The question is basically what is the value of the flux Richardson number. Its dynamical significance lies in the fact that it gives a measure of the relative importance of the buoyancy force as compared to shear-production force. Richardson numbers near zero indicate buoyancy (thermal effects) have negligible effects on the fluid flow. The gradient Richardson number is easier to measure and where it is small, the flux and gradient Richardson numbers are considered equal (38). Measurements made by Ruggles (43) over the ocean indicated less than 6% of the Richardson numbers were over 0.03. This condition is the limit of the near-neutral state (28). Indications from measurements made over land, are that when horizontal velocities are greater than 6 m/s, the Richardson numbers are generally less than 0.03 (27). The choice of 6 m/s is based on optimization analysis of commercially feasible power generation related to wind turbine size and velocities as determined by Putnam (42) and Golding (21). Measurements made at the coastal headland (Yaquina Head) were in the near-neutral range for winds greater than 6 m/s. It was for these reasons that the thermal energy equation was not considered applicable to this experiment.

The necessary similarity conditions are:

a. For continuity-geometric similarity,

b. For momentum-Reynolds number similarity,

c. For turbulence-Reynolds stress, correlation coefficient, and Kolmogorov similarity hypothesis,

d. For mean and turbulent velocities, the approach flow of the model must be similar to the prototype,

e. The longitudinal pressure gradient in the approach must be zero.

The geometric similarity was satisfied by undistorted scaling of the model. All length variables are scaled to a reference length used to non-dimensionalize the conservation of mass equation. Reynolds number similarity cannot be obtained since the higher velocity will cause excessive turbulence and compression effects in the model. Noting that the turbulent contribution to shear stress is greater than the molecular contribution, except near the surface (53), we can expect some relation between turbulent Reynolds number (Re_t) and laminar Reynolds number. This relation is $(Re)_{model} \approx (Re_t)_{prototype}$. Typical ratios of eddy diffusivity to viscosity are approximately 10^3 (9). This allows Reynolds number similarity for model scales in the 10^2 to 10^3 range. The use of screens and boundary layer thickeners will develop the necessary velocity profile similarity and the shear velocities related to Reynolds stress, correlation, and Kolmogorov similarity.

The final approach flow requirement of zero longitudinal pressure gradient can be obtained by adjusting the variable ceiling in the wind tunnel until the condition is satisfied.

Model Study

Wind Tunnel

The Oregon State University Environmental Wind Tunnel is a closed return tunnel driven by a three-blade, variable-pitch aircraft propeller. Speed control is achieved through a vari-drive between a constant speed AC motor and the propeller. Both the rotational speed and propeller pitch can be changed from the control console which is located adjacent to the test section.

A schematic of the tunnel is shown in Figure 2.1. The test section is 1.52 meters wide by 1.22 meters high by 9.14 meters long. The 9.14 meter dimension is to allow for the build up of a thick turbulent boundary layer.

Wind speeds from 300 cm/sec to 1000 cm/sec can be obtained by the operator at the control console. The turning vanes in the 90° bend areas of the recirculating configuration reduce separation, allowing for a more uniform stream. The flow straightener is an aluminum honeycomb, 3.45 cm thick, with flow tubes of rectangular crossections that are approximately 0.63 cm x 0.63 cm. This breaks down the large eddies caused by the propeller into eddies of approximately the same dimension of the flow tubes. Following the flow straightener is an 18 x 14 mesh screen with wire size of 0.229 mm. This reduces the eddies to approximately 0.16 mm size. The smaller eddies are more easily dissipated by viscous action. The 9.14 m long test section is to allow this dissipation to take place. The resulting level of turbulence intensity is less than 0.3%.

A variable ceiling at the end of the test section where the model is located, allows adjustment of the axial static pressure gradient. For atmospheric boundary layer flow this gradient must be zero in the approach flow to the model. An operational view of the tunnel is shown in Figure 2.2. The direction of wind flow is from the section

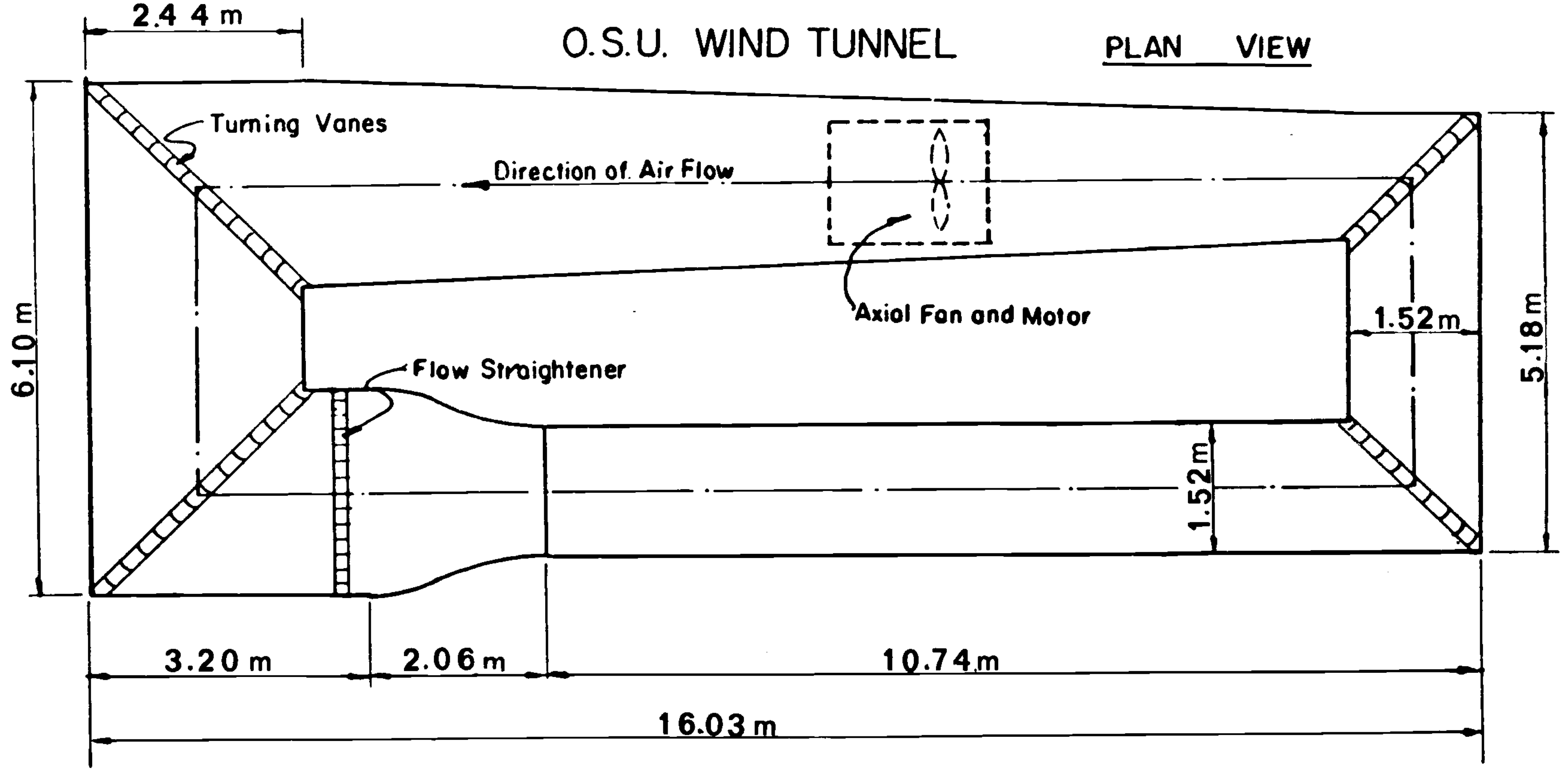

Figure 2. 1. Plan view--OSU wind tunnel.

of the tunnel on the left of the figure. Entering the test section, the wind first passes a pair of access doors with plexiglass view windows. Continuing through the 9.14 meter long by 1.52 m x 1.22 m section, the wind arrives at a second pair of access doors with plexiglass view windows. This is the section for terrain model studies. The movable control console is shown adjacent to this section.

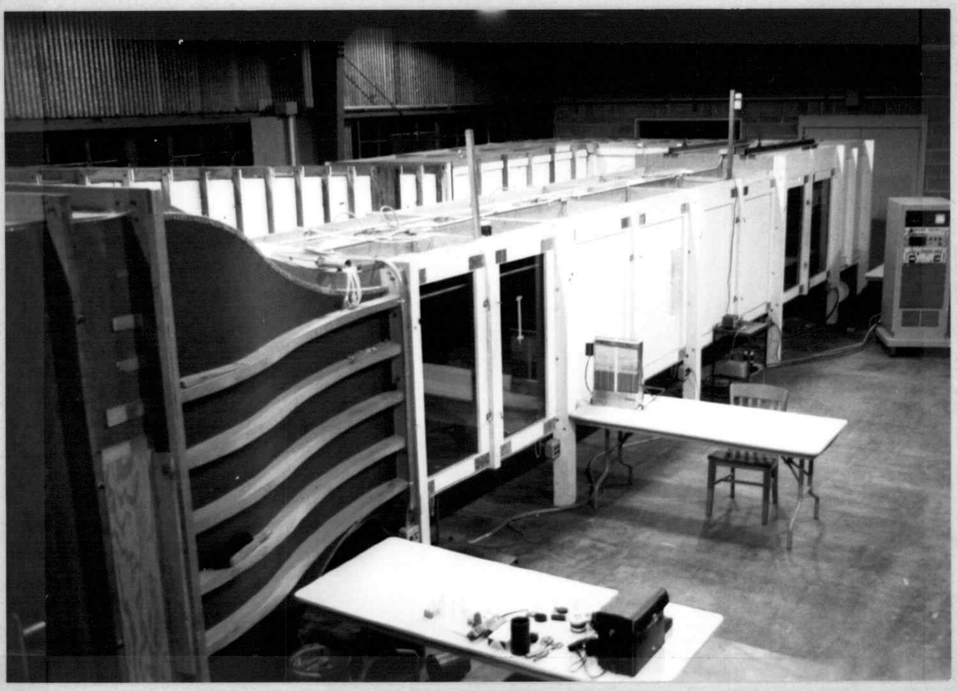

Figure 2.2. Operational view of the wind tunnel.

Velocity Sensor System

The average velocity was measured with a pitot tube and manometer. The pitot tube is 3.0 mm diameter stainless steel, with a 1.2 mm impact hole and four equally spaced 1.0 mm static holes. It is manufactured by Dwyer Instruments, model 167-6.

The manometer consists of a pressure sensor and indicator. The sensor is a variable capacitor sensor with bridge and preamplifier in a self-contained unit. The indicator supplies power to the sensor, and converts the preamplifier output to a proportional DC output of ± 10 V DC full scale. This can be read on a built-in meter scale or on an output to a digital voltmeter, recorder, or oscilloscope. The sensor capacity is 1 mm Hg. This allows readings of velocities from 152 cm/sec to 1460 cm/sec. The pressure-velocity relation is non-linear, resulting in more sensitivity at lower speeds. Response time is less than 0.3 secs. The sensor-indicator is calibrated to a linear voltage scale with an error of less than 4 mv. This is equivalent to 0.0004 mm Hg. The resulting error in velocity is 0.37 cm/sec. For the velocities in this experiment, this represents an error of 0.04%.

The manufacturer of the manometer is MKS Instruments, Inc. The indicator is the model 170 and the sensor is model 145.

The velocity versus position of the pitot tube above the model surface was recorded on an Esterline Angus Model XY530 differential recorder. Accuracy is ±0.2% of full scale. The scales are 1, 10, and 100 mv/in, 1 v/in and 10 v/in with continuously variable control between these calibrated positions. Repeatability is +0.1% of full scale and hysteresis of ±0.1% of full scale. The frequency response is DC to 5 Hz at 1 inch peak to peak, within ±3 dB.

Turbulence Sensor System

Turbulence measurements were performed using a Thermo-Systems, Inc., constant temperature control system, Figure 2.3. The probe consists of two film type sensors 90° to each other. A platinum film less than 1000 Angstrom units thick is deposited on a quartz rod that is 0.51 mm in diameter. The film length is 1 mm. The frequency response is enhanced by electronic compensation to allow 4×10^5 cycles/sec. This is a factor of 10^3 greater than the atmospheric turbulence. The temperature control system maintains the film temperature at a constant level by detecting the resistance change of the film as it is cooled by the flow of air over its surface. In other words, the electronic system senses any unbalance in the Wheatstone bridge due to film heat loss fluctuations and feeds current to the bridge to rebalance it. The relation between velocity and current is non-linear. Circuits to linearize the velocity simplify

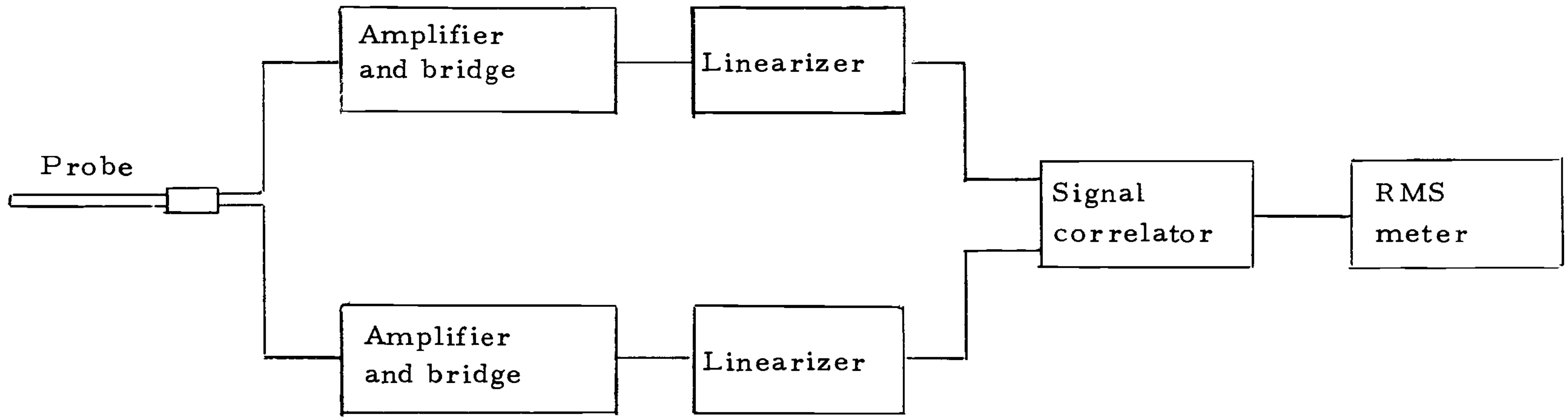

Figure 2.3. Block diagram of turbulence sensor system.

analysis of the signals for various turbulence parameters. The correlator contains amplifiers, summers, and differentiators to allow readout on the RMS meter of Reynolds stress, correlation of the two signals from the probe and sum and difference of the two signals. The sum is proportional to the turbulent longitudinal velocity and the difference is proportional to the lateral turbulent velocity.

A view of the turbulence sensor system in operation is shown in Figure 2.4. The wind tunnel control console is on the left, the TSI anemometer system on the table near the console, next to it an oscilloscope with the anemometer indicator on top and the remaining two instruments are recorders.

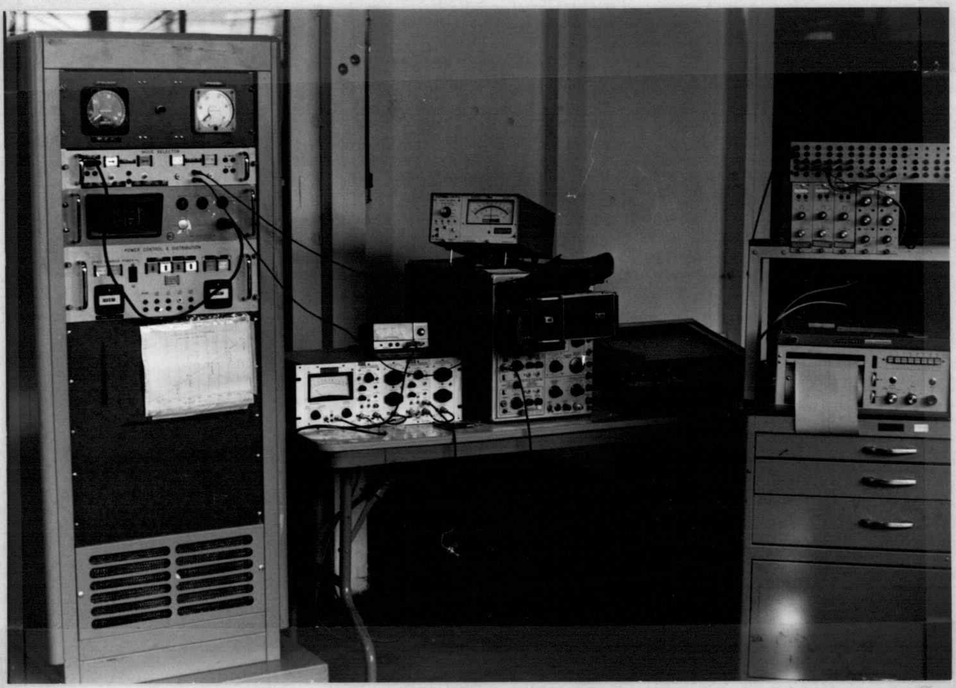

Figure 2.4. Wind tunnel test equipment.

Remote Sensor Position Apparatus

It is necessary to position the sensor both vertically and laterally from outside the wind tunnel and to indicate its position electrically. This arrangement allows recording the measured parameter as a function of position of the sensor. The survey carriage was designed and constructed for this experiment. A general view as installed in the wind tunnel is shown in Figure 2.5. The vertical guide rods and drive can be replaced by different lengths to suit the experimental conditions. The sensor position can be positioned to within 0.75 mm.

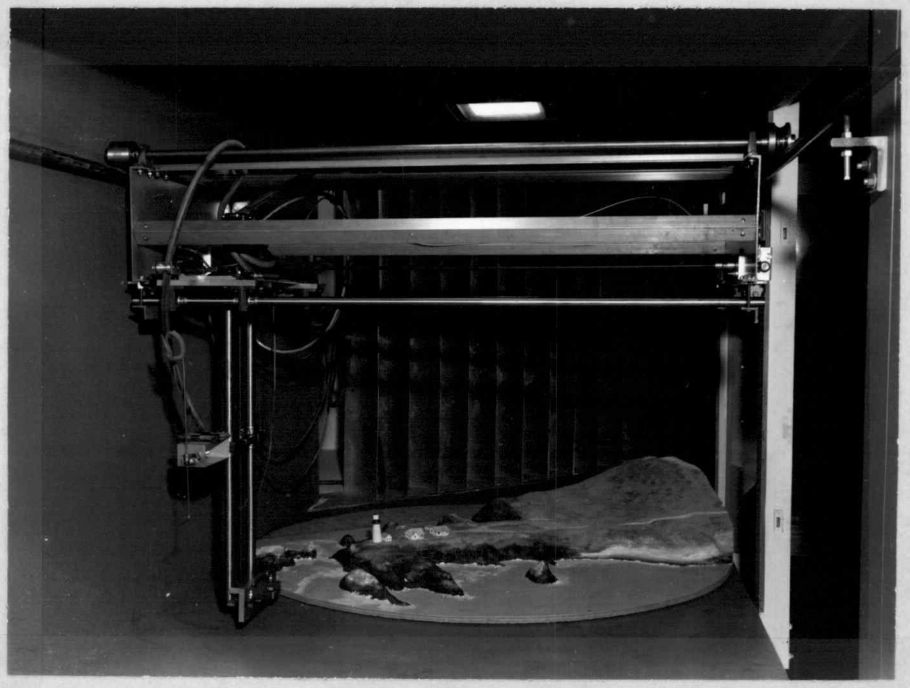

Figure 2.5. Survey carriage in the wind tunnel.

Model of Yaquina Head

A 300:1 scale model of Yaquina Head was constructed with 2.5 cm thick styrofoam sheets, cut and layered to match the topographical map. The surface was filled and sealed with Sculptamold, a commercial modeling material. The completed model prior to modifying for the wind tunnel is shown in Figure 2.6. To allow positioning of the model in the tunnel to various wind directions, it was cut in a 1.52 m diameter circle to match the tunnel width (Figure 2.7).

Prototype Study

Coastal Surveys

The coastal surveys recorded by Bourke et al. (6) were based on U.S. Weather Bureau Stations in and near cities on or close by the coast. For the ocean, data from merchant, naval, and research ships were obtained through the National Oceanographic Data Center. However, the data from lightships proved more reliable. The geostrophic winds were determined then corrected for surface effects to compare to the lightship data. Correlation was satisfactory for the annual distribution. This data indicated two peak periods for high velocity (greater than 600 cm/s) winds existing over 25% of the time. One in the winter with a prevailing southerly direction and the other in the

Figure 2.6. Yaquina Head model.

Figure 2.7a. Yaquina Head model installed in the wind tunnel.

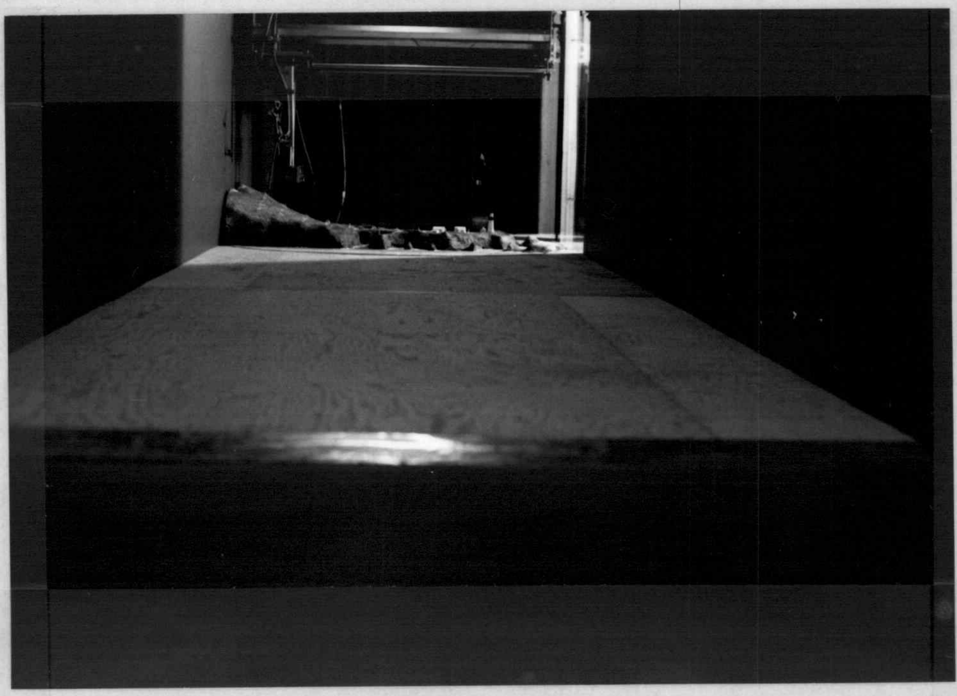

Figure 2.7b. Approach flow area to Yaquina Head model.

summer with a prevailing northerly direction. Yaquina Head extends westward and lies directly athwart these dominating winds. As a result of this type of information, the Oregon wind survey program, reported by Hewson et al. (25), established anemometer stations on Yaquina Head in 1973. Analysis of the data indicated that during the summer, over 16% of the time the winds from the north exceeded 600 cm/s. During the winter, over 16% of the time the winds from south to southeast exceeded 600 cm/s. This information was the basis of selection of the dominant wind directions for the model study (Appendix C).

Test Site

Plans to obtain field data involved several considerations. Ideally, a velocity profile survey at each intersection of a 30 m grid covering the western 370 m of the headland would supply information relative to the effect of several terrain variations on velocity. This would be conducted simultaneously with velocity profile surveys over the ocean approach flow to indicate the relative effects of surface geometry changes on established flow. Several methods of measuring the velocity profiles, including rocket smoke trails, balloon-theodolites, tethered instrumented blimps or kites, and a truck mounted telescoping boom were considered. All had drawbacks of cost, accuracy, availability and/or continuity of record. Realizing that a grid survey would only have merit if all data were recorded simultaneously to allow comparison between sites and that the complexity was beyond the material and personnel capability of the program, it was decided to concentrate on a careful study of one field site.

As noted in the introduction, instrumented towers have been found most useful for atmospheric boundary layer flow measurements. The decision to use a tower involved consideration of U.S. Coast Guard approval, available power, and minimum cost compatible with obtaining reliable data. An existing concrete pad 168 m east of the lighthouse provided a level, firm base for erecting a commercial steel scaffold. This was considered safe, if erected to 25 m and guyed at 6 m intervals. It was noted, after installation, that when winds above 12 m/s were blowing, the two legs of the scaffold on the upwind side were not touching the ground. This validated the decision to limit the height to 25 m. The tower location relative to the light house is shown in Figure 2.8. Detailed views are shown in Figures 2.9 and 2.10.

Velocity-Azimuth Sensor Systems

A total of four recording anemometers were located at elevations above the tower base of 8 m, 13 m, 20 m, and 27.5 m. Each of the lower three anemometers was mounted on a 2 m extension

Figure 2. 8. Instrumented tower installed on Yaquina Head.

Figure 2.9. Anemometers installed on the tower.

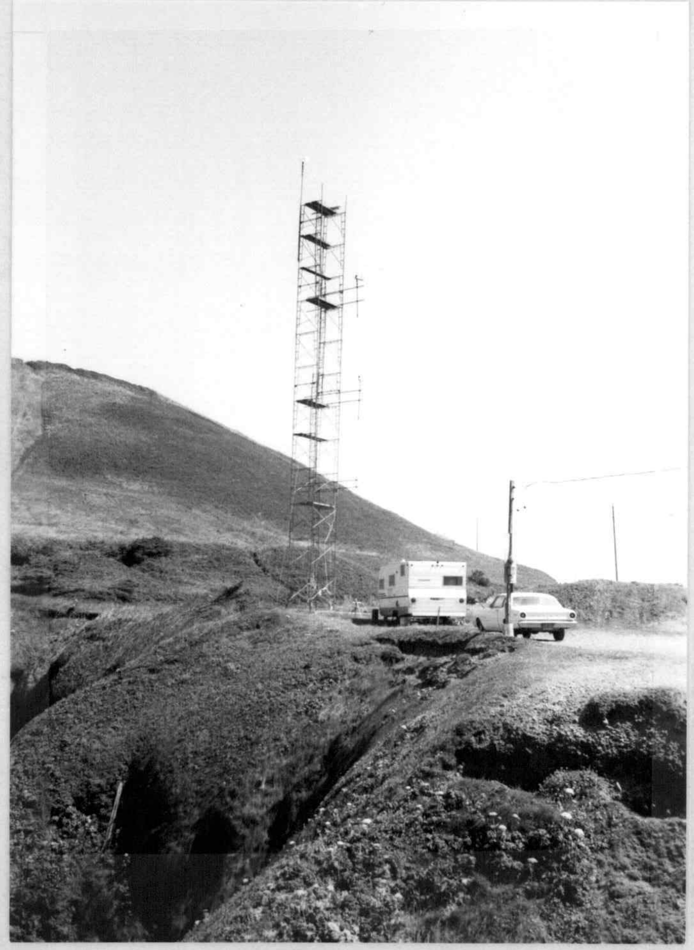

Figure 2.10. Anemometer tower with instrument trailer.

from the tower to prevent tower induced wind effects on the anemometers. The 27.5 m anemometer was mounted on a steel pole extending 2.5 m above the top of the tower. The installation is shown in Figures 2.9 and 2.10.

The lowest and highest anemometers were R.M. Young model 6101 3-cup units. Resolution of these units is ±22 cm/sec. The other two anemometers were the propellor or aerovane type, Belfort Type L, with resolution of ±89 cm/sec. The recorders for the Belfort units were Monmouth Electric Co. Inc., model RO-2C/GMQ. The recorders for the R.M. Young units were an Esterline Angus Model 602 and R.M. Young model 291. Recorder accuracies were ±1% of their full scale readings.

The recorders were installed in the instrument trailer shown in Figures 2.9 and 2.10. The interior view is shown in Figure 2.11.

As a backup for checking the recorders, a hand held anemometer was used. This was a Belfort Model 6052. Accuracy is 3% of the full scale. The two scales are 772 cm/sec and 3100 cm/sec. All instruments and recorders were calibrated prior to installation and after removal in the wind tunnel using the MKS velocity sensor system.

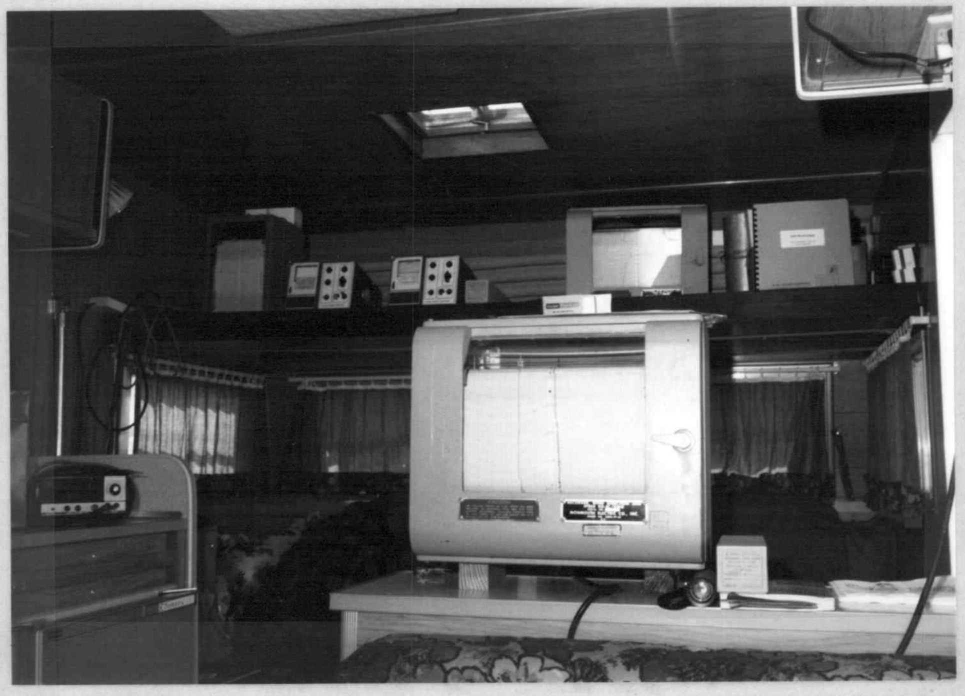

Figure 2.11. Anemometer recorders installed in the instrument trailer.

Turbulence Sensor System

This system was the same as the unit described in the section under model studies. Turbulence was measured at 3 meters and 8 meters above ground. This system is shown in Figure 2.12. On the right of the figure is the temperature sensor system and recorder. The two instrument consoles on the left are the turbulence anemometer system.

Figure 2.12. Turbulence anemometer and temperature sensor systems.

The linearized output of the anemometer was recorded by a Lockheed Electronics model Store 4 magnetic tape unit. This unit records up to four channels with bandwidths of 20,000 Hz and signal to noise 48 dB. At the tape speed used in this experiment, the bandwidth was 5000 Hz and signal to noise 48 dB. It was necessary to record the turbulence for spectral analysis in the laboratories of the Mechanical Engineering Department.

The length of coaxial sensor cables is limited to 8 m for impedence matching requirements. This required locating the turbulence system at the base of the tower during measurement periods only. To protect the instruments, they were kept in the Coast Guard building at Yaquina Head, as shown in Figure 2.12.

Temperature Sensor Systems

The temperature sensors were chromel-alumel, 0.0127 mm diameter, thermocouples. Sensitivity is approximately 2 mv per 100°C. This signal was amplified by an electronic system designed by the University of Washington for use in meteorology research conducted by the OSU School of Oceanography. Two sensors, 50 cm apart, are mounted in a probe holder shown with the electronics system in Figure 2.13.

The amplifier output was recorded on an Esterline-Angus model T171B, transistorized, self-balancing recorder. Accuracy of the recorder was ±0.5% of full scale. Recordings were made for 10 hour periods with the sensors located first at 20 cm above the ground and then 8 m above the ground.

In addition to this system, a Foxboro temperature-humidity recorder, model 10, was used to continuously record ambient conditions at approximately 2 m above the ground. The relative humidity recorder has an accuracy of 5% relative humidity and the temperature recorder an accuracy of 0.5% of 311°K.

As a check on these systems, a mercury in glass thermometer was used to check temperatures and a sling psychrometer to check relative humidity.

Ambient pressure was recorded continuously with an Instrument Corp. Micro-barograph model B211. Variations were less than 10 millibars during the test period.

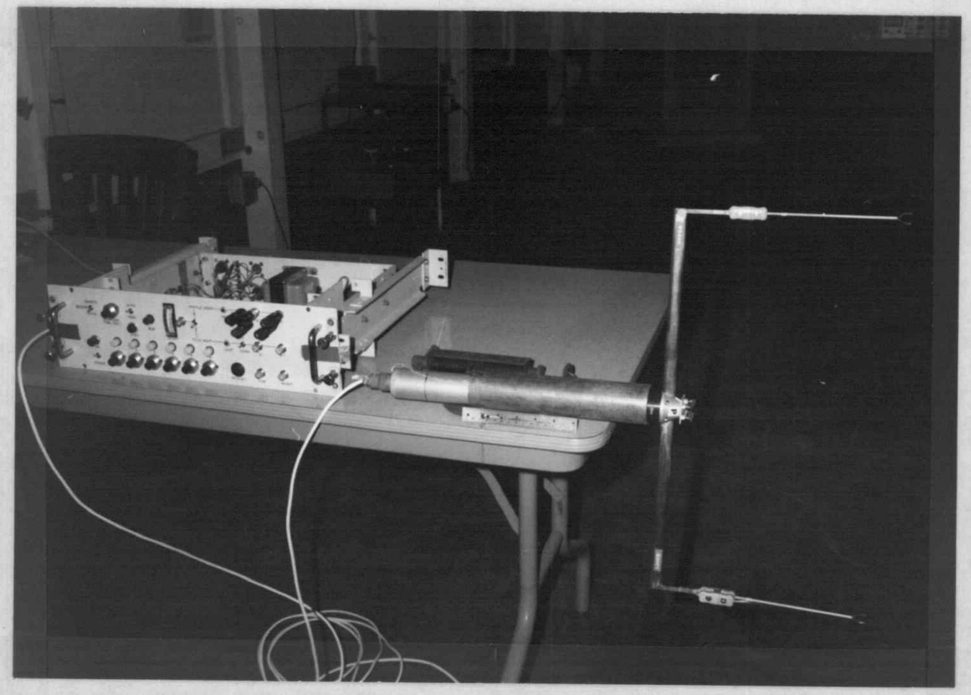

Figure 2. 13. Temperature sensor system.

III. METHOD OF TESTING

Wind Characteristics in the Wind Tunnel

The similarity conditions relative to this experiment require a high Reynolds number. The flow characteristics of the wind tunnel without models or boundary layer thickeners but with the high Reynolds number flow is shown in Figures 3.1 and 3.2. The minimum turbulence intensity along the axis of the tunnel: $u'/U = 0.26\%$ and the lateral turbulent intensity is: $v'/U = 0.19\%$. Cermak (9) has obtained turbulence of about 0.1%. As can be seen in Figure 3.1, this intensity is from the center out to the vicinity of the laminar boundary layer limit. The highest turbulence is where boundary layer effects dominate the flow. Turbulence drops to zero at the walls, as pointed out by Schlichting (44).

In Figure 3.2, the mean value of the product, $\overline{-u'v'}$, is equal to the turbulent shear stress when multiplied by density, ρ. The value of shear stress approaches zero near the center of the test section for reasons of symmetry, whereas its maximum occurs near the wall showing that turbulent friction has the largest value in that area. The correlation coefficient, C_{ij}, between the longitudinal and transverse fluctuations at each point is also shown in Figure 3.2. Strong correlation at the wall with a rapid drop to zero in the center of the tunnel is a reflection of the direct relation of the correlation

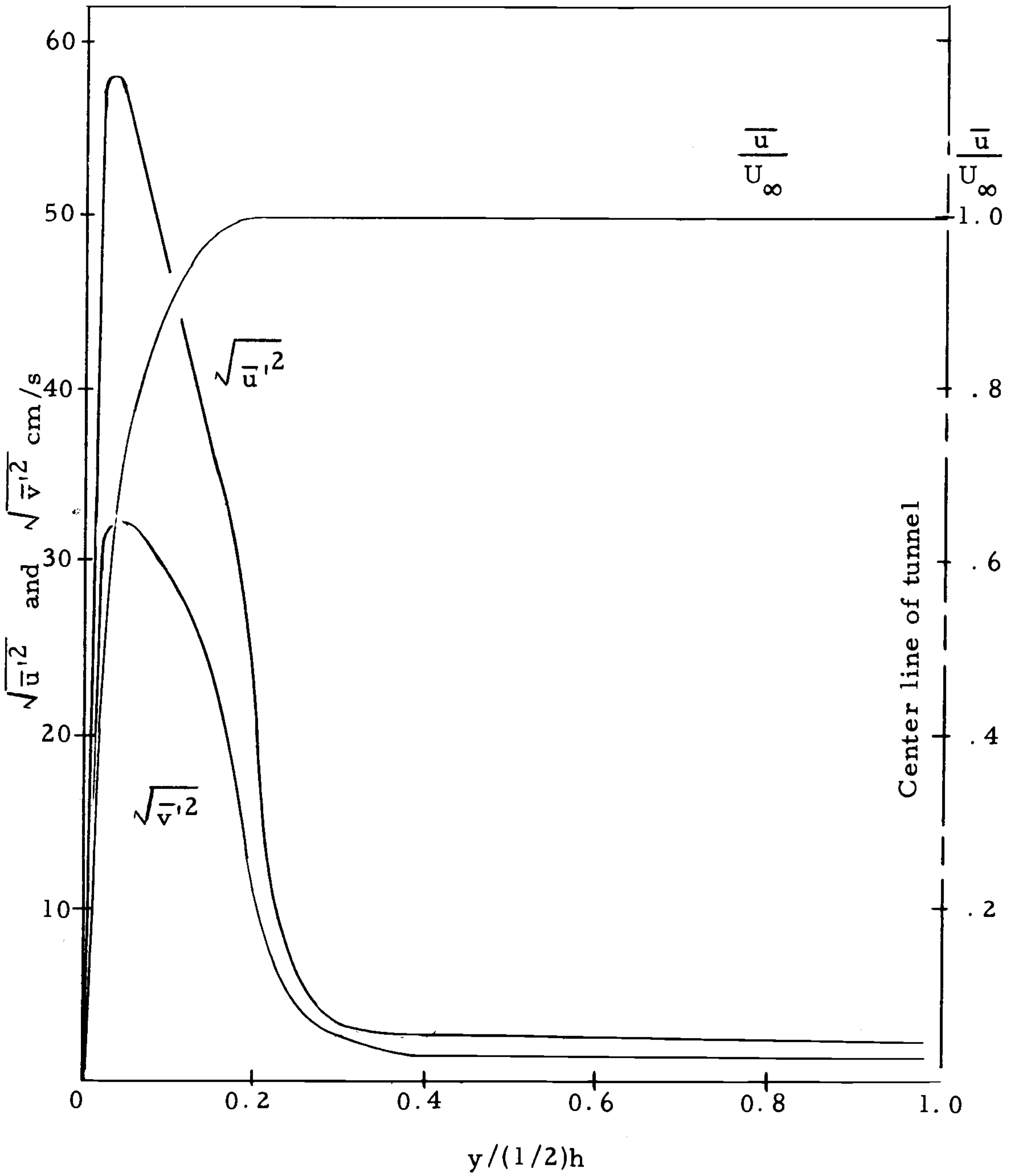

Figure 3.1. Average and turbulent wind characteristics in the wind tunnel for U_∞ = 975 cm/s.

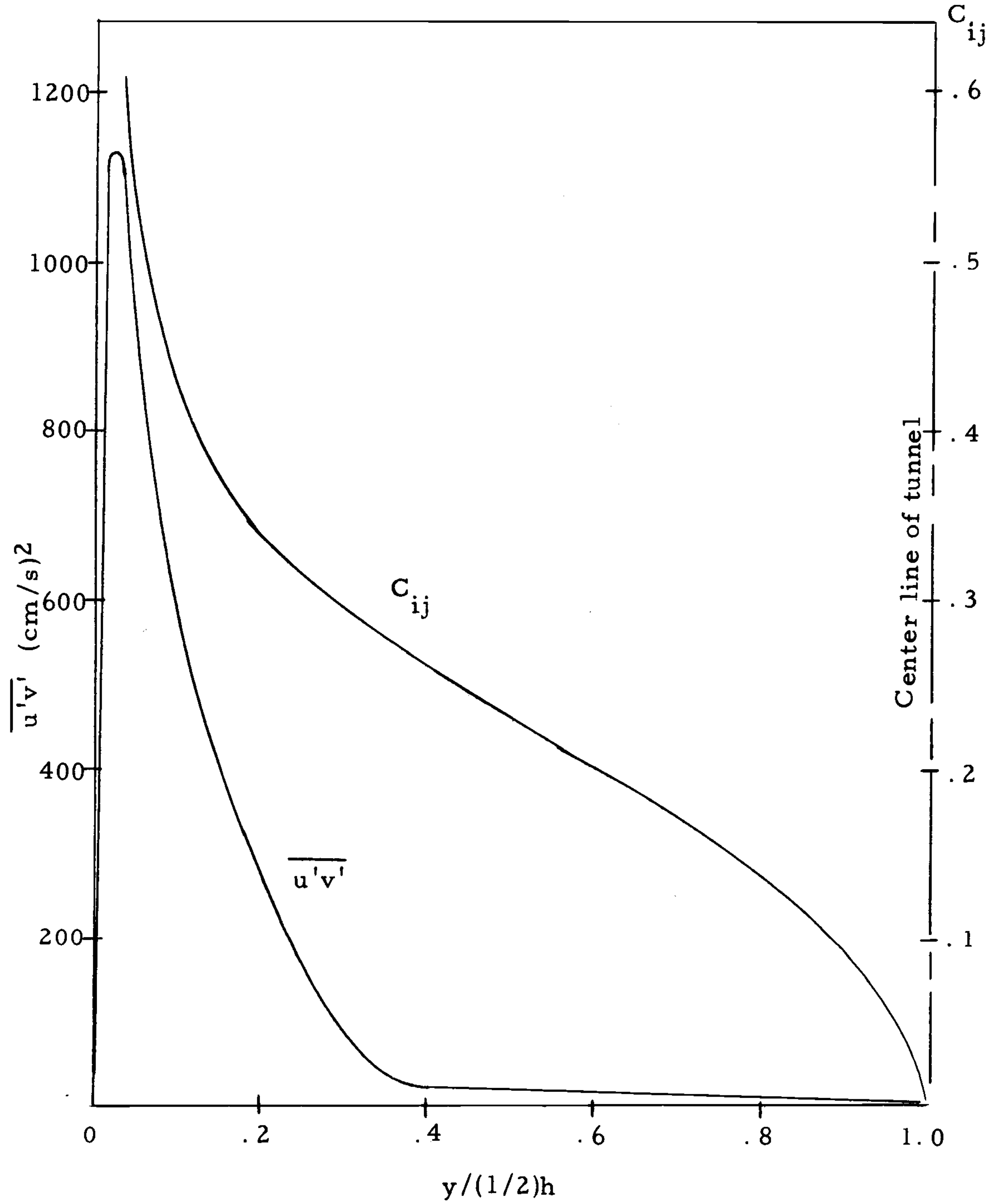

Figure 3.2. Turbulent shear stress and correlation coefficient in the wind tunnel.

coefficient to the turbulent shear stress.

Local isotropy requires that small-scale turbulence become spherically symmetrical at sufficiently large Reynolds numbers, according to Kolmogoroff (16). Local isotropy leads to the requirement that the spectral energy distribution of the small scale motion have the following relation:

$$\phi(\omega) = \frac{(\epsilon \nu^5)^{1/4}}{u} F(K/K_s)$$

The universal nature of the function F both in nature and in the laboratory is indicated in Figure 3.3. It should be pointed out that there is a minimum length of boundary layer development required before the turbulence becomes similar. The measurements in the OSU wind tunnel were made at the model test section, a distance of more than 10 m from the screen.

The dissipation of turbulent energy per unit mass, ϵ, has been observed in the atmosphere (39, 54) and laboratory (9). Table 3.1 lists the values and compares to the value obtained in the highly turbulent boundary layer of the wind tunnel. The very low turbulent intensity outside of the boundary layer did not exhibit isotropy. The scaling factor: $\epsilon_{windtunnel}/\epsilon_{atmosphere}$, for turbulent dissipation, ranges from 2 to 2350. For the specific relation of wind over water and the smooth surface OSU wind tunnel, the factor is 9. This type of

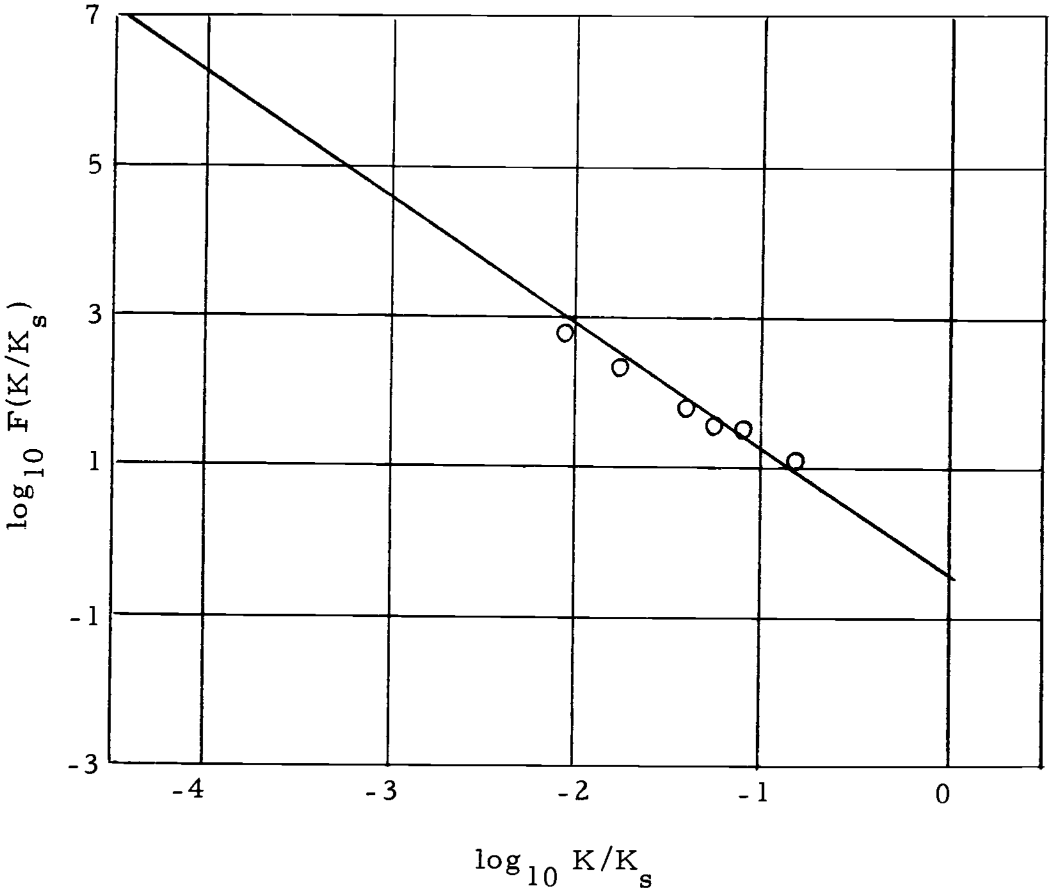

Figure 3. 3. Comparison of spectra from the OSU environmental wind tunnel with the Kolmogorov hypothesis.

scaling in wind tunnels has not been completely analyzed due to lack of information about this type of flow (10).

Table 3.1. Magnitudes of turbulent dissipation for atmospheric and laboratory flow conditions.

Turbulent Dissipation cm^2/sec^3	Flow Conditions	Height	Reference
80 to 95	Atmospheric wind over water	1 m above water	39
157 to 1656	Atmospheric wind over open field. Velocities 300 to 600 cm/s	2 m above ground	54
186 to 43,200	Colorado State University wind tunnel. Smooth surface	1.3 to 51 cm	9
761	Oregon State University wind tunnel. Smooth surface	0.6 cm	

Larger eddies can exist away from the boundary layer. Some indication of the size of these eddies can be determined from the scale of turbulence (44):

$$L = \int_0^{h/2} R(Z)dZ \tag{3.1}$$

Here we define $R(Z)$ as the correlation function of the velocity fluctuations at two neighboring points 1 and 2 in the flow field:

$$R_c = \frac{\overline{u_1' u_2'}}{\sqrt{\overline{u_1'^2}}\sqrt{\overline{u_2'^2}}} \tag{3.2}$$

The scale of turbulence for the wind tunnel is approximately $L = 10$ cm. This is an estimate of the average size of the turbulent eddies. Taylor (49) made measurements and found a relation:

$$L \approx 0.14\left(\frac{h}{2}\right) \tag{3.3}$$

Applied to the wind tunnel this would be $L = 8.6$ cm, a reasonable check on the measurement.

Modifications of the Wind Tunnel to Obtain Similarity to Atmospheric Boundary Layer Flow

The five conditions of similarity mentioned in the Objective and Description of Test are:

a. geometric

b. Reynolds number

c. Reynolds stress, correlation coefficients, and Kolmogorov similarity hypothesis all related to turbulence

d. approach flows have similar mean and turbulent velocities

e. approach flow with zero longitudinal pressure gradient.

In the same section, the subject of geometric and Reynolds number similarity was discussed in detail. This section will discuss the methods and measurements to obtain similarity of items (c) and (d).

The approach flow similarity is the most critical and has a dominant effect on the model. Therefore, it will be discussed first. The characteristics of the tunnel boundary layer were mentioned in the previous section on Wind Characteristics in the Wind Tunnel. A comparison of the velocity profiles of the bare tunnel, tunnel with boundary layer thickener, and atmospheric flow over the ocean (43) is shown in Figure 3.4. The smooth floor is limited to a scaled height of 45 m while the rough floor has a scaled height of 80 m. Depending on terrain, the atmospheric boundary layer is 100 m to 1000 m (38). Over the ocean, the thickness is closer to 100 m. Another factor considered is the tower height is 45 m in the log-linear velocity profile range in the model to match the prototype. The logarithmic law of Prandtl, mentioned in Appendix A, equation (A1.52), fits a significant amount of observed data in the atmosphere (38). Ruggles (43) fitted the majority of velocity profiles measured over the ocean to this relation. The wind tunnel boundary layer also conforms to the logarithmic law, Figure 3.5.

Plate (38) has indicated that to obtain independence from Reynolds number similarity, the following relation is necessary:

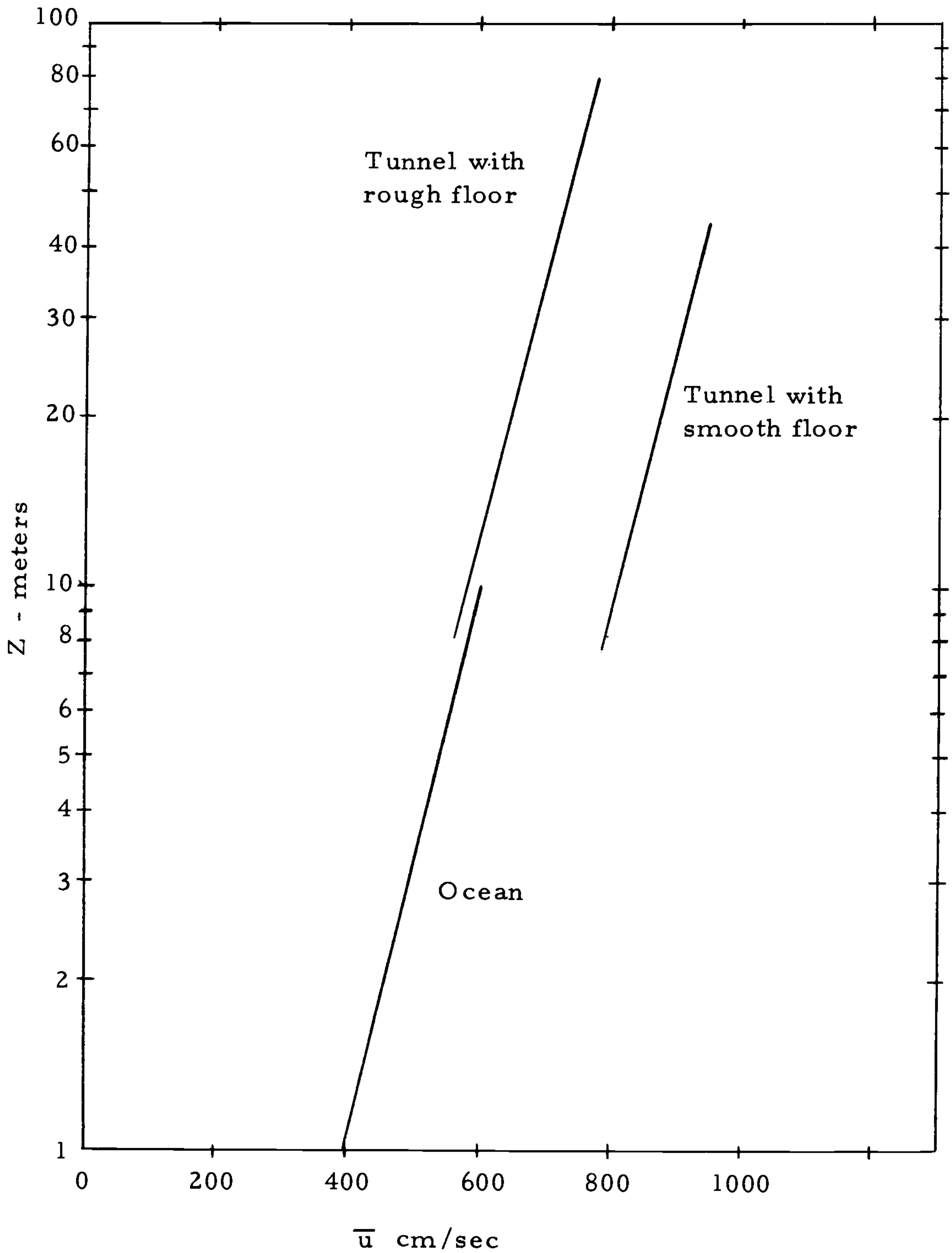

Figure 3.4. Velocity profiles over the ocean and in the wind tunnel (scaled at 300:1).

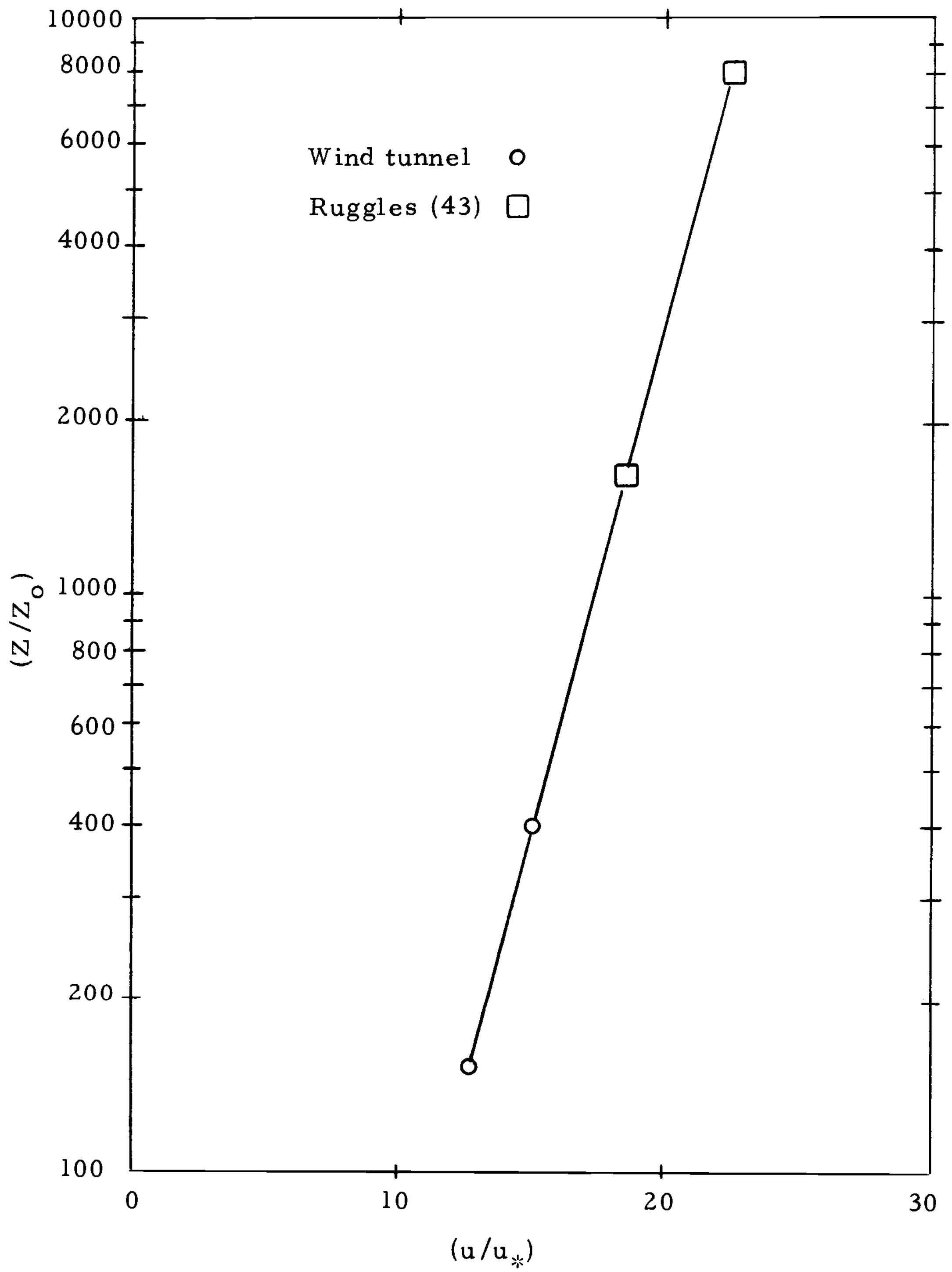

Figure 3.5. Wind tunnel and ocean boundary layer comparisons for the logarithmic velocity relation: $u/u_* = 1/k \ln(Z/Z_o)$.

$$\frac{u_* Z_o}{\nu} > 70$$

For a tunnel value of $Z_o = 1$ cm at a $u_* = 56$ cm/s, the value of the ratio is:

$$\frac{u_* Z_o}{\nu} = \frac{56 \times 1}{0.145} = 386$$

This removes the requirement for Reynolds number similarity. Implicit in the above relation is the fact that the shear velocity, u_*, and the aerodynamic roughness, Z_o, must be related in model and prototype. Plate states that the u_* and the ratio (Z_c/Z_o) are the same in model and prototype. The symbol Z_c is a scaling height. For Ruggles data at a $Z_c = 1$ m, the ratio varies from 10 to 3000 due to variation in wave heights. In the wind tunnel, at $Z_c = 1$ m, the ratio is 10. The shear velocity from Ruggles data varies from 2 cm/sec to 60 cm/sec. These values were determined by solving the logarithmic equation at two elevations. In the wind tunnel, two methods were used. One was the use of the logarithmic relation. This gave values of shear velocity between 34 cm/sec and 98 cm/sec. Lumley and Panofsky (38) have indicated that, with the exception of regions very close to the ground, the shear velocity has an empirical relation:

$$u_*^2 = \overline{-u_i'u_j'}$$

This value was measured with a pair of hot film anemometer sensors in the wind tunnel. Values of shear velocity varied from 4 cm/s to 55 cm/s for heights above the tunnel floor of 38 cm to 1 cm respectively. Confining the height on the same scale relation as used by Ruggles (1 m to 10 m) the shear velocity remains constant at 55 cm/s. These appear to be acceptable relations for similarity (9).

The modification of the tunnel floor required a compromise between increasing the thickness of the boundary layer and similarity of Reynolds stress. Small blocks of wood increased the boundary layer height but at the same time distorted the velocity profile in such a fashion that it did not fit the logarithmic relation, equation (A 1.52). Also, the shear velocities increase to values greater than 100 cm/sec, preventing this type similarity. It was found that the use of 18 x 14 mesh screen with wire size of 0.229 mm arranged as shown in Figure 3.6, thickened the boundary layer as shown in Figure 3.4 with the Reynolds stress or shear velocity mentioned in the previous paragraph. The screen height is approximately 7.6 cm and extends the full width of the wind tunnel.

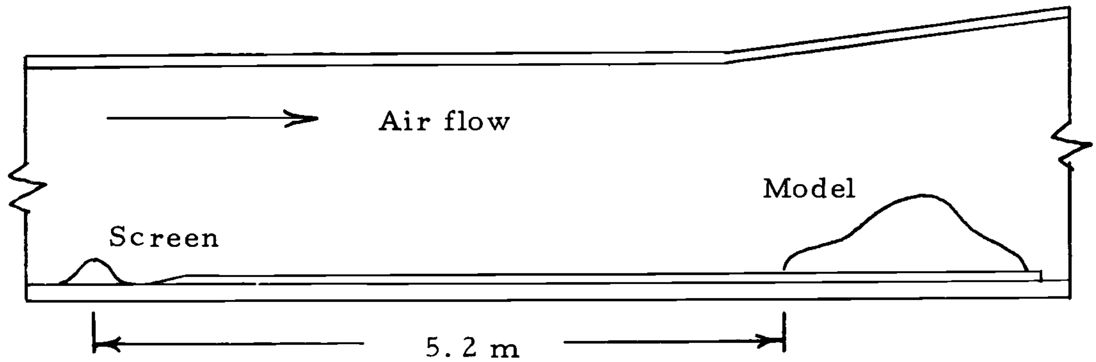

Figure 3.6. Boundary layer thickening screen in the wind tunnel.

Model Test Procedure

A grid was layed out on the model with its origin at the light house and extending in increments of 30 m in four directions, beginning at north and progressing in 90° increments. The intersections of the grids served as the reference points for measuring vertical velocity profiles. This data is presented in Appendix D. The change in profile when flowing over a blunt body has the general characteristics of acceleration and separation as a function of geometry which we would expect from aerodynamic experience (44). The two dominant flow directions were recorded (north and south). The variation of wind direction of ±30° from these directions did not show any discernable effect on velocity profiles.

Turbulence measurements were made, as necessary, over the approach flow at vertical distances of 1 cm, 2 cm, 5 cm, 10 cm, 25 cm and 38 cm. These same distances were used over the tower site and a location 10 cm south of the tower site. The measurement of Reynolds stress, cross correlation, and turbulence intensity was from data presented by the correlator and RMS meter associated with the hot-film anemometer mentioned in the equipment description in the section on the Model Study.

The determination of Kolmogorov similarity and the turbulent energy dissipation required further analysis.

Turbulence is a stochastic process and therefore requires statistical analysis. We are interested in the probability of a varying velocity, $u(t)$, falling below a value, u. We define an indicator function $\phi(u,t)$ that indicates when $u(t) < u$. The probability of this occurrence is:

$$P(u;t) = \phi(u;t)$$

The probability density is defined as:

$$\beta(u;t) = \frac{\partial P(u;t)}{\partial u}$$

From Fourier transform theory, we define a characteristic function:

$$F(K;t) = \int_{-\infty}^{+\infty} e^{iKu} \beta(u;t) du$$

Here, K is the inverse of wavelength. The moments determine the series expansion of F.

$$F(K;t) = \sum_{n=0}^{\infty} \frac{\overline{u^n(t)}}{n!} (iK)^n$$

The above definitions are necessary to an understanding of the physical process of the analysis. The simultaneous occurrence of velocities at any two times requires extension of the previous analysis to define joint moments:

$$u^n(t_1)u^m(t_2) = \iint_{-\infty}^{+\infty} u_1^n u_2^m \beta_2(u_1, u_2; t_1, t_2) du_1 du_2$$

These definitions depend on assumptions of a stationary process, fitting in with the desire to determine properties of the process. One important property or cross moment as defined above is the autocovariance, $\overline{u(t_1)u(t_2)}$. This results in an autocorrelation function:

$$\rho(t_2 - t_1) = \rho(t) = \frac{\overline{u'(t_1)u'(t_2)}}{\overline{u'^2}}$$

In turbulence, it is useful to describe a waveform in terms of its spectral characteristics in the frequency domain. The spectrum of a random signal consists of a continuous distribution of energy with respect to frequency. The frequency content of a random signal is usually described in terms of power density versus frequency of power-spectral density:

$$\phi(\omega) = \frac{1}{2\pi} \int_{-\infty}^{+\infty} e^{-i\omega t} \rho(t) \overline{u'^2}\, dt$$

From this brief series of definitions, it can be seen that the analysis of turbulence to obtain the power-spectral density requires band pass filters, squarers, and integrators. The system used in this experiment is a Saicor model SAI - 52B Spectrum Analyzer. The input to the analyzer is a fluctuating voltage representing velocity as a function of time. With the proper selection of frequency range of the filter network, summing intervals, and attenuation, the output of the analyzer is in terms of $(cm/s)^2$ per hertz versus frequency. This is plotted on an X-Y recorder similar to the unit described under the Model Study equipment for velocity measurement. A typical plot is shown in Figure 3.7. The ordinate of the plotter is the decible (dB) relation of the ratio of output power (P_o) to input power (P_1)

$$dB = 10 \log\left(\frac{P_o}{P_I}\right)$$

The plotter chart records -5 dB for each inch on the ordinate, starting at the top. The value of the power-spectral density in $(cm/s)^2$ per

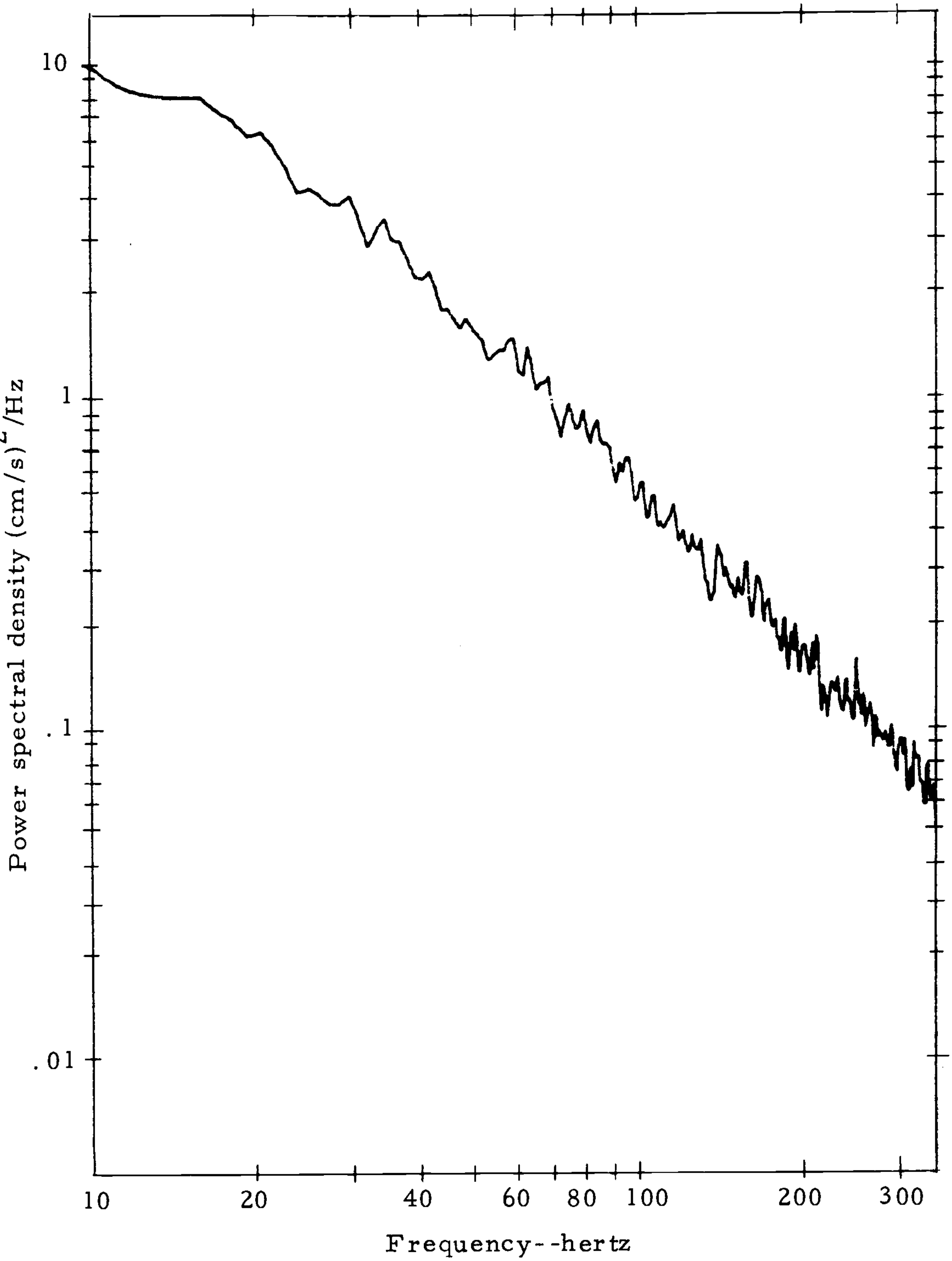

Figure 3.7. Example of power spectral density output from the spectrum analyzer.

hertz is determined by calibration of the spectrum analyzer with a wide band noise generator, such as a General Radio, GR 1381. This provides the reference calibration resulting in the logarithmic scale of power-spectral density shown on the figure.

The energy dissipation in isotropic turbulence is

$$\epsilon = 15\nu \overline{\left(\frac{\partial u'}{\partial x}\right)^2}$$

Using Taylor's hypothesis, the space derivative can be transformed to a time derivative:

$$\epsilon = 15\nu \frac{1}{\bar{U}^2} \overline{\left(\frac{\partial u'}{\partial t}\right)^2}$$

Now ϵ can be expressed as a function of the spectrum of $(\partial u'/\partial t)$ in the familiar form (54):

$$\epsilon = 15\nu \int_0^\infty K^2 \phi(k) dK$$

Once this value is determined, the data may be computed for the normalized function then compared to published information on spectra such as was shown in Figure 3.3. This will validate that the method of test meets the Kolmogorov similarity hypothesis.

IV. RESULTS

Comparison of Model and Prototype

Typical velocity profiles over the model are shown in Figure 4.1. Further velocity profiles over the model are shown in Appendix D. Typical velocity data from Yaquina Head is tabulated in Table 4.1. The complete velocity data from the tower is tabulated in Appendix B. Not all of the data in Appendix B shows a constant or increasing velocity from 20 m to 27.5 m. In some cases the velocity at 27.5 m is less than at 20 m. These profiles that do not fit with generally accepted theory of surface boundary flow were noted at Risø, Denmark, by Petersen (37) and eliminated from analysis. Only velocities greater than 600 cm/sec were of interest in this study. Also, only data for steady flow conditions, i.e., velocities greater than 600 cm/sec for two hours or more, was considered. In the case of winds from the south, these conditions were relaxed since this direction is not dominant for the summer period, but a comparison was needed.

Panofsky (33) has discussed the flow in the atmospheric boundary layer over a terrain change as separating into two parts, air that has been affected by the terrain change and air that has not been affected. The interface between these two flows is an inflection point in the velocity profile. This is shown for both the prototype and

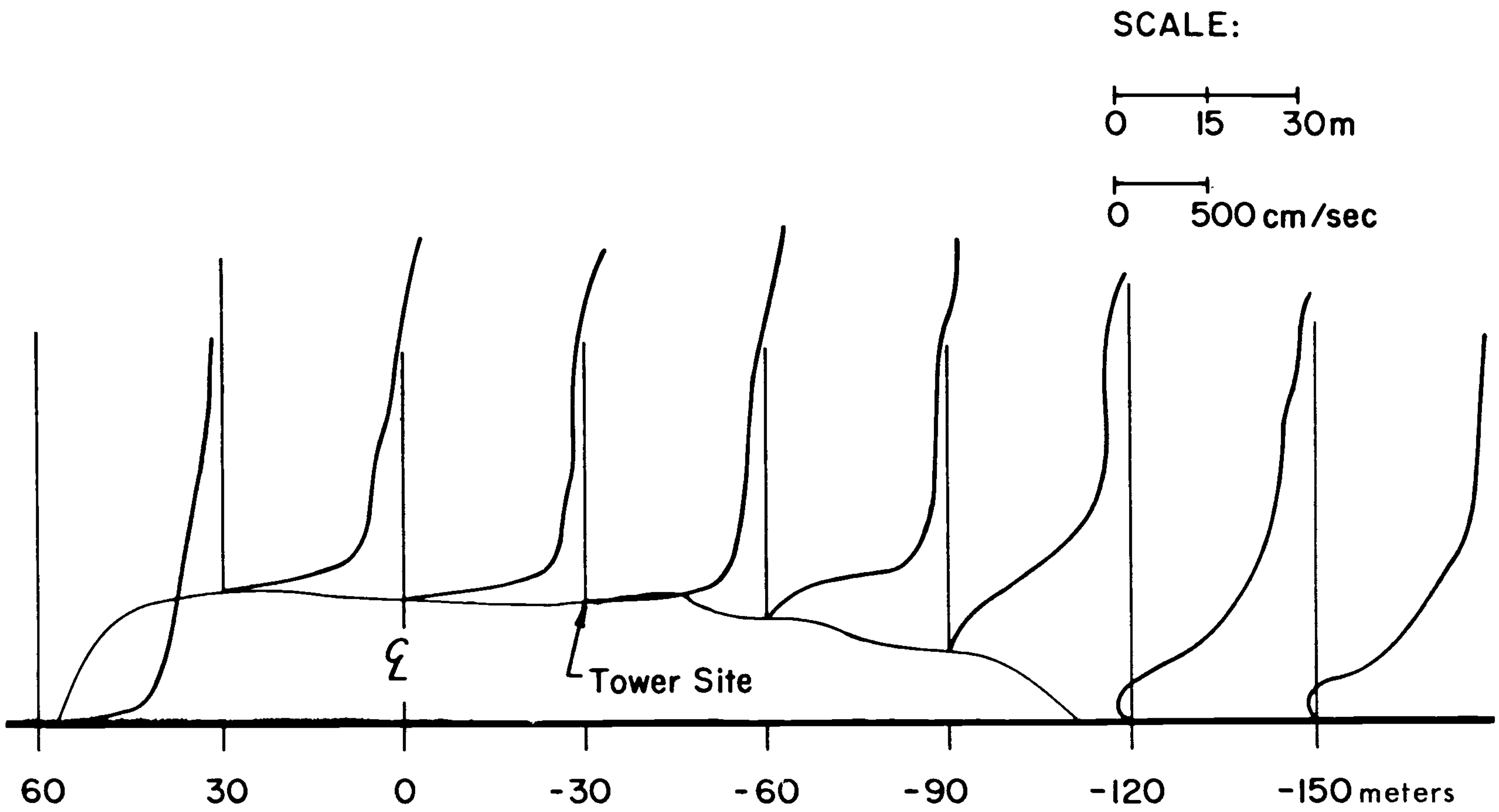

Figure 4.1. Typical velocity profiles through a north-south section of the model at 180 m (scaled) east of the lighthouse.

the model (scaled) in Figure 4.2. These inflection points in velocity profiles on the model are apparent in the figures of Appendix D, also. The profiles for wind flow from the south are shown in Figure 4.3. Present change-of-terrain theories propose that the disturbance causing inflection points at the interface between the flow caused by the roughness change and the approach flow, rises at a maximum rate of one-in-ten (38). The map, Figure 1.1, indicates the tower is approximately 120 m from both the north and south beaches. This would place the inflection point at 12 m. The model shows an inflection at 19 m from north wind and 18 m from south winds. The Yaquina data shows inflections at approximately 20 m for both north and south winds. It is obvious from the complex structure of the north shore in comparison to the south that the one-in-ten rule cannot be applied without these topographical considerations. However, as a rough approximation, the model shows good agreement. No doubt there are some three dimensional turbulent flow effects that were not measured in this experiment. These effects are not considered in the one-in-ten rule.

Some indication of turbulence characteristics of the flow and how they change when flow is from smooth to rough surfaces will be analyzed for possible clues of the disturbance affecting velocity profiles.

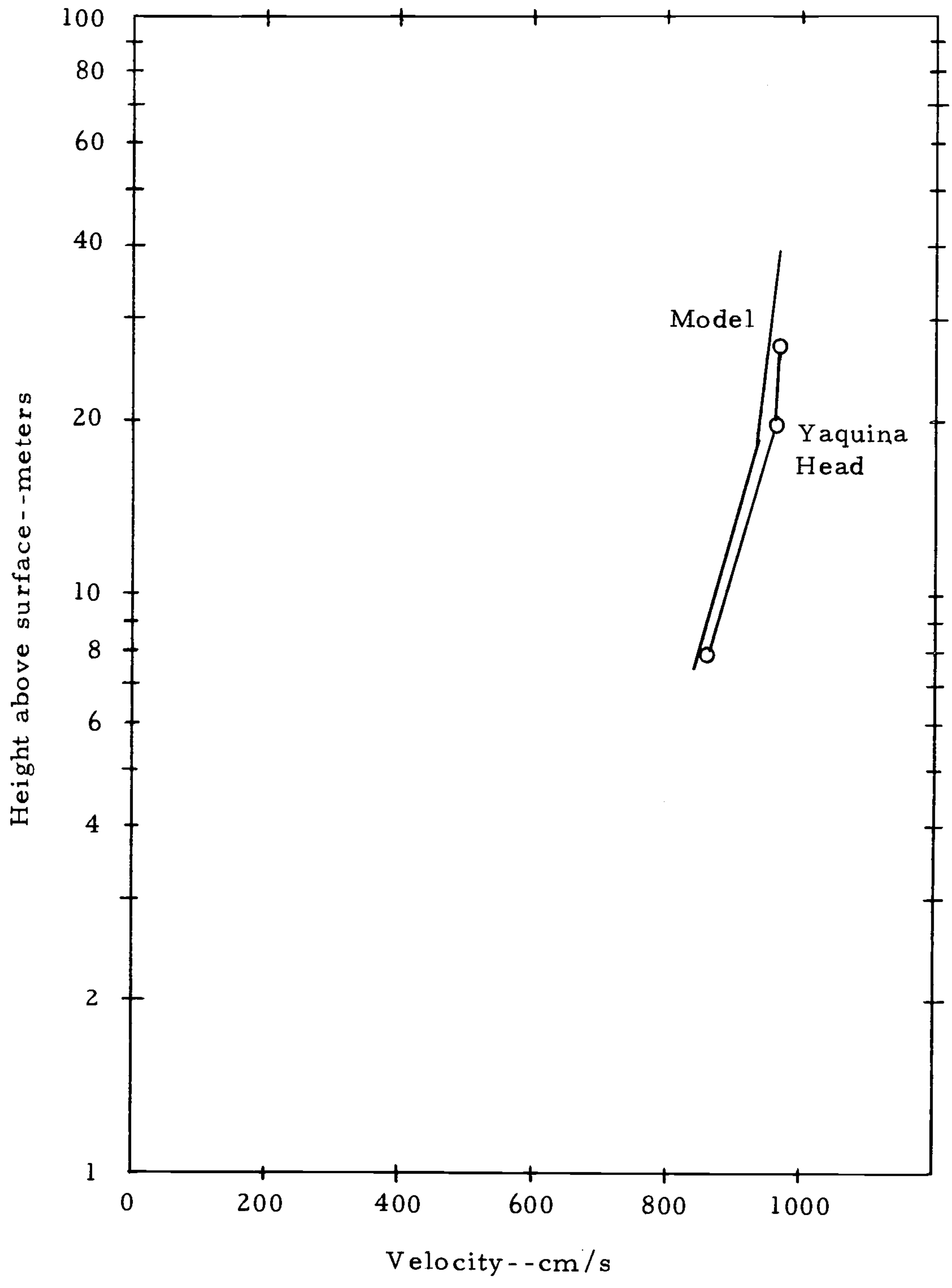

Figure 4.2. Comparison of velocity profiles at Yaquina Head test tower and the wind tunnel model (scaled). Wind from the north.

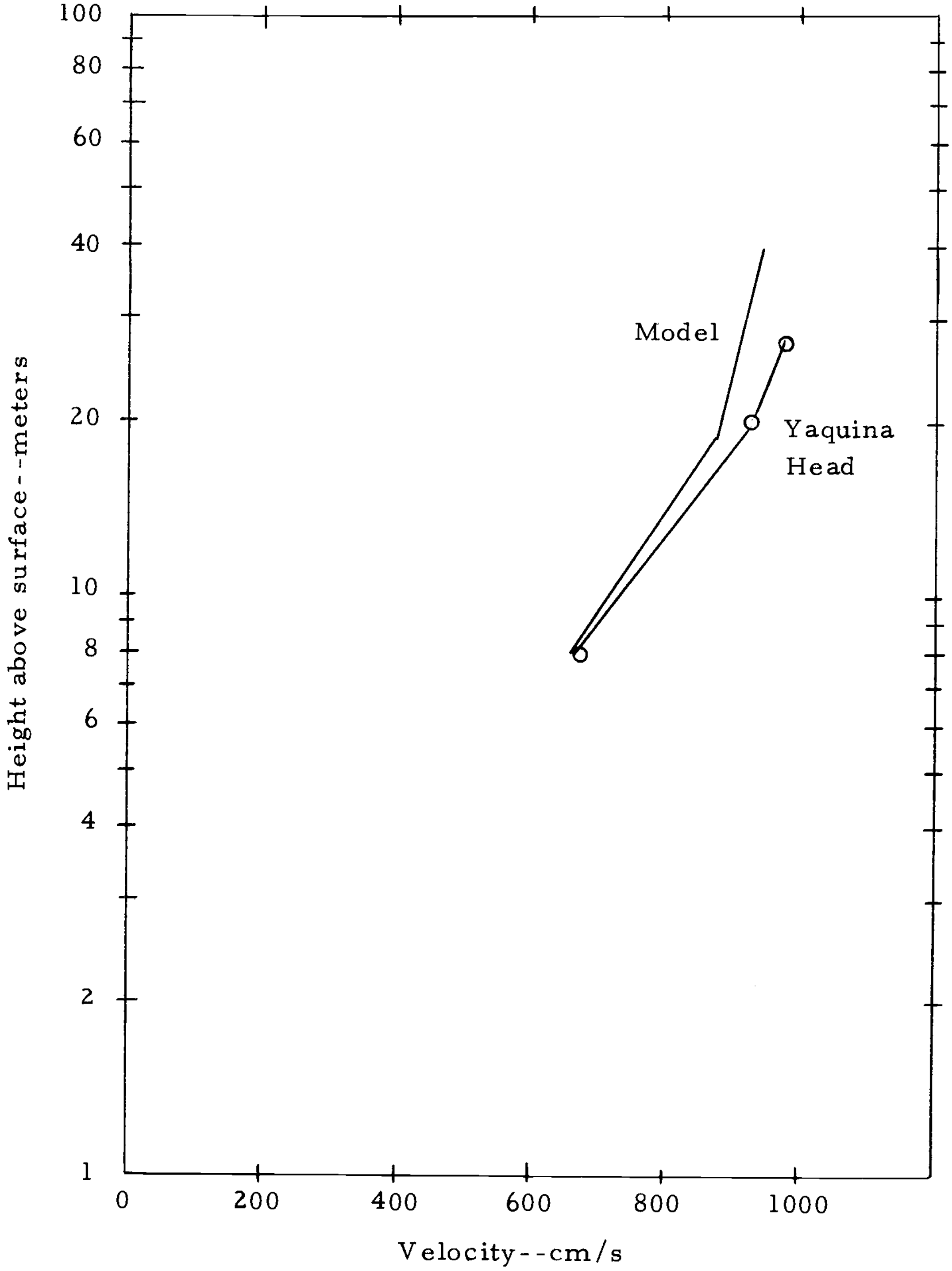

Figure 4.3. Comparison of velocity profiles at Yaquina Head test tower and the wind tunnel model (scaled). Wind from the south.

Table 4.1. Velocity (cm/s) data sample from the Yaquina Head test tower, July 21, 1975.

Anemometer Location	Pacific Daylight Time										
Z Meters	8	9	10	11	12	13	14	15	16	17	18
8	224	492	581	715	626	536	626	626	626	581	581
13	224	586	671	805	626	626	671	671	715	581	626
20	268	581	715	849	671	626	715	715	760	626	671
27.5	268	581	626	805	671	581	671	671	671	581	581

Table 4.2. Turbulence intensity.

Height Above Surface			Wind Tunnel	Wind Tunnel	Yaquina Head Tower Site	
cm	Scaled Meter	Wind Tunnel	Approach Flow	Tower Site	Z Meter	
1	(3)	.08	.15	.38	3	.16
2.5	(7.5)	.07	.12	.09	7.5	.11
5	(15)	.06	---	.08		
10	(30)	.04	---	.08		
12.7	(38)	---	.09	---		
15	(45)	.005	.06	.07		
25	(75)	.0027	.006	.03		
38	(114)	---	---	.008		
51	(153)	---	---	.005		

In Table 4.2, the turbulence intensity is seen to decrease with height, as expected. The approach flow has a higher intensity as explained under Method of Test. With increased roughness, the intensity increases. However, there was no sharp drop of intensity at the elevation equivalent to the velocity profile inflection point. For comparison, the scale relation of intensity in the prototype and model is about one to two at the 3 m level and about one to one at the 7.5 m level. Similarity of this parameter has not been investigated extensively (9).

The Reynolds stress data is tabulated in Table 4.3. The approach flow has a fairly constant stress in the boundary layer. Over the rough terrain, there is a sharp increase of stress as expected. At the elevation of velocity profile inflection, the stress increases, then drops off as we approach the top of the turbulent boundary layer. This indicates increased mean momentum transfer due to turbulence. Since the velocity begins to increase after 30 m in the model, this momentum transfer may be partially responsible. Scaling of model and prototype indicates the model is 10^2 to 10^3 greater than the prototype, which is the inverse of the geometry scale.

The correlation coefficient is an indication of the correlation between longitudinal and lateral turbulent velocities. The low values in atmospheric flows are expected for random processes. In the wind tunnel, Schlichting (44) has reported data of less than 0.5 at the wall, and decreasing to zero at the center line. Scaling appears to be one-to-one. This would seem to indicate the same degree of randomness in model and prototype flow. The change in correlation at the altitude of velocity profile inflection may indicate some three dimensional effect. These effects were not considered in this experiment.

Table 4.3. Reynolds stress. $((1.02/\rho)\mathrm{Pa})10^{-3}$.

Height Above Surface			Wind Tunnel	Wind Tunnel	Yaquina Head Tower Site	
cm	Scaled Meter	Wind Tunnel	Approach Flow	Tower Site	Z Meter	
1	(3)	1.43	1.01	5.44	3	.005
2.5	(7.5)	1.3	1.01	1.0	7.5	.008
5	(15)	.86	--	1.3		
10	(30)	.43	--	1.73		
12.7	(38)	--	.86	--		
15	(45)	.008	--	1.04		
25	(75)	.002	--	.31		
38	(114)	--	.004	.02		
51	(153)	0	--	.004		

Friction or shear velocity (u_*^2) is equal to Reynolds stress at low viscosity.

A comparison of the turbulence parameters of Tables 4.2, 4.3, and 4.4 at two different locations on the model is presented in Table 4.5. Since there is a difference of velocity profile inflection height at these two points, it was thought that one of the turbulence parameters would be shown to be more sensitive to both height and displacement, therefore indicating its value as a disturbance measure. The Reynolds stress shows an increase at the inflection height, and a lower value at the lower inflection height. Methods of closure in analytical modeling have used closure relations involving Reynolds stresses and mean wind distribution (37).

The turbulent energy dissipation is tabulated in Table 4.6. Lumley and Panofsky (28) listed data from several authors who have

Table 4.4. Correlation coefficient.

Height Above Surface: cm	Height Above Surface: Scaled Meter	Wind Tunnel	Wind Tunnel Approach Flow	Wind Tunnel Tower Site	Yaquina Head Tower Site: Z Meter	Yaquina Head Tower Site
1	(3)	0.61	0.36	0.37	3	0.3
2.5	(7.5)	0.56	0.32	0.19	7.5	0.2
5	(15)	0.45	--	0.30		
10	(30)	0.46	--	0.35		
12.7	(38)	--	0.17	--		
15	(45)	0.30	--	0.26		
25	(75)	0.26	0.48	0.35		
38	(114)	--	0.25	0.49		
51	(153)	--	--	0.19		

Table 4.5. Turbulence characteristics: comparison of two locations on the wind tunnel model.

Height Above Surface cm	Turbulence Intensity: Tower Site	Turbulence Intensity: 10 cm South	Reynolds Stress $((1.02/\rho)Pa)10^{-3}$: Tower Site	Reynolds Stress $((1.02/\rho)Pa)10^{-3}$: 10 cm South	Correlation Coefficient: Tower Site	Correlation Coefficient: 10 cm South
1	.38	.25	5.44	10.9	.37	.7
2.5	.09	---	1.0	---	.19	---
5	.08	.096	1.3	1.15	.30	.27
10	.08	.09	1.73	1.58	.35	.31
15	.07	.074	1.04	1.04	.26	.25
25	.03	.035	.31	.29	.35	.33
38	.008	.008	.02	.02	.49	.42
51	.005	.005	.004	.003	.19	.2

estimated dissipation. Between 1 m and 10 m the value of dissipation varies from 1000 to 10 cm^2/s^3. Experimental data from other sources was shown in Table 3.1. Values of 80 cm^2/s^3 to 1656 cm^2/s^3 were measured in the atmospheric boundary layer at less than 2 m. The measurements at Yaquina Head were within this range.

Table 4.6. Comparison of turbulent dissipation between the model and Yaquina Head.

Height Above Surface		Wind Tunnel Approach Site	Wind Tunnel Tower Site	Yaquina Head Tower Site
cm	Scaled Meter	cm^2/s^3	cm^2/s^3	cm^2/s^3
1	(3)	---	1431	685
2.5	(7.5)	533	1479	1570
5	(15)	459	1675	
10	(30)	463	1533	
18	(51)	905	724	

The approach flow of the model simulates flow over the ocean where dissipation values of 80 cm^2/s^3 have been measured in the atmosphere.

The scaling factor: $\epsilon_{\text{wind tunnel}}/\epsilon_{\text{atmosphere}}$, is approximately 7, which is within the range reported by Cermak (10). Comparing the same levels above MSL on the model tower and ocean requires adding 5 cm to the ocean height. There is an increase of over 300% in dissipation when flowing from smooth to rough surfaces for the same height above sea level. However, at a scale height between 15 m and 30 m (profile inflection point), the dissipation increase drops to less than 170%. In a steady, homogeneous, pure shear flow, energy production equals energy dissipation. The reduced energy dissipation could indicate less energy production with a resulting decrease of energy into the flow having a corresponding effect on the momentum.

The scale of turbulence was defined in equations (3.1). Indications of this length are that it rises from 12.8 cm over the approach flow to 17 cm over the model. The increased roughness increases the size of the turbulent eddies with a resultant increase in turbulent energy production. The estimate of scale of turbulence at Yaquina Head could only be made up to 8 m due to the limits of equipment, as mentioned. The size of eddies in that elevation were 5.7 m. Using the same scaled elevation limit on the model, an estimate of eddy size for 8 m elevation would be 0.9 m. This gives a scaled ratio of turbulent eddies of approximately 6 to 1. Using this factor, we could estimate turbulent eddies on the prototype as having a maximum size of six times the maximum over the model, or about 20 m at the height of the tower. Although this is a very rough estimate, it does have a relation to the topography at Yaquina Head, where the bluff intercepting the wind is approximately 20 m in height. In the studies of turbulence in wind tunnels (44), turbulent eddy size is related to the size of the cylinder interrupting the flow. We can hypothesize here that the turbulent energy production that affects the mean flow is affected by both the elevation of the roughness as well as the one-in-ten rule for the horizontal length of the roughness.

One of the five conditions of similarity mentioned in the Design of Experiment was the Kolmogorov similarity hypothesis. The first hypothesis mentioned in Appendix A was the dependence of the average properties of small scale components of turbulence at large Reynolds number on kinematic viscosity of the fluid and the average rate of dissipation of energy per unit mass of fluid. The demonstration of this dependence from measurements in the atmosphere, tidal channel, and wind tunnels was indicated in Figure 3.3. Verification of this hypothesis at Yaquina Head is shown in Figure 4.4. This indicates the importance of this similarity in the wind tunnel model.

In the discussion of Model Studies of Atmospheric Boundary Layer Flow, mention was made of the Richardson number as one of the similarity parameters. Large Richardson numbers at low wind speeds was noted at Yaquina Head, as shown in Table 4.7. The experimental design condition was for velocities over 600 cm/s as previously mentioned. For these conditions, the Richardson number drops to less than $|0.2|$, the range of sustained turbulence.

The near-neutral condition of $|Ri| \leq 0.03$ appears to be approached when high velocities are sustained for greater than two

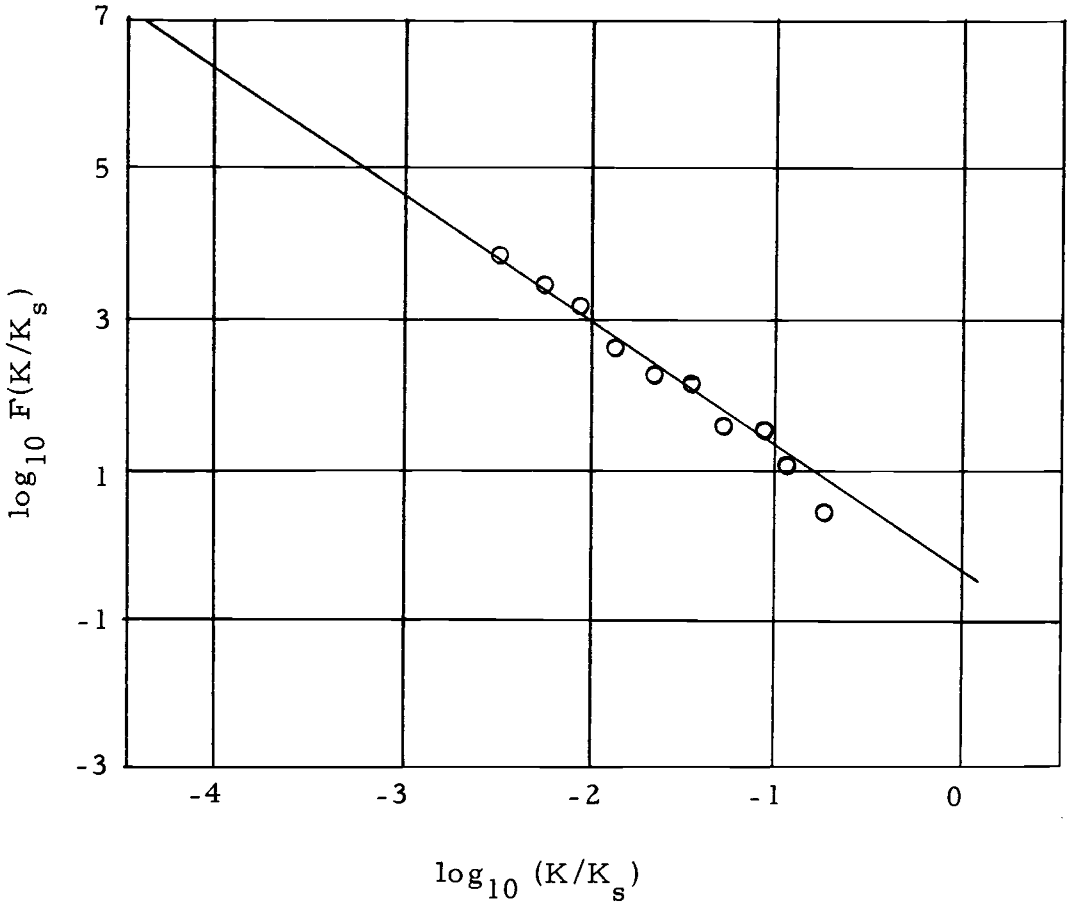

Figure 4.4. Comparison of spectra measurement of Yaquina Head data with Kolmogorov hypothesis.

hours. This additional condition was imposed on selection of data from the test tower for comparison to wind tunnel data, as in Figures 4.2 and 4.3.

Table 4.7. Ground level gradient Richardson number.

Time Pacific Daylight	Average Velocity cm/s	Ambient Temperature °K	Gradient Richardson Number Ri
800	50	284	22.36
1000	224	284	5.36
1200	760	284	0.125
1400	760	286	0.062
1600	1073	285	0.028
1800	1341	284	0.0078

V. CONCLUSIONS AND RECOMMENDATIONS

The objective of this experiment was to simulate the atmospheric boundary layer flow in a wind tunnel. Using the similarity parameters of the equations of motion and continuity, the approach flow in the wind tunnel was modified to be similar to the atmosphere. In addition, it was demonstrated that the turbulent energy dissipation, Reynolds stress, and Kolmogorov similarity hypothesis could be modeled in a wind tunnel approach flow. The change-of-terrain velocity profile inflections observed in atmospheric boundary layer flow (34) were duplicated in the wind tunnel, Figures 4.2 and 4.3.

The variation in the turbulence characteristics for the smooth-to-rough boundary layer flow were measured to observe any relationship to the average velocity profile changes. The Reynolds stress plays a dominant role in mean momentum transfer by turbulent motion. It was demonstrated on the model that the elevation near the velocity profile inflection point was also the maximum Reynolds stress outside of the viscous region.

Validation of model velocity profile changes for flow from smooth-to-rough-terrain was demonstrated by velocity measurements made on a 27.5 m tower at Yaquina Head, Figures 4.2 and 4.3.

There is an extensive amount of theoretical analysis demonstrating the importance of turbulent energy effects on the mean flow (26, 34). More data is needed on the relationship of turbulent energy to mean flow. The turbulent energy dissipation is considered the most dominant term in the boundary layer close to the ground (less than 100 m). Data has been presented on the changes in the turbulent energy dissipation for smooth and rough flow in a wind tunnel. Comparison to values measured at Yaquina Head indicate a range of scaling ratios of approximately:

$$1 \leq \frac{\epsilon_{\text{wind tunnel}}}{\epsilon_{\text{prototype}}} < 2.$$

The significance of the scaling ratio is not clearly known, however, the demonstration of the sharp drop in turbulent energy dissipation at the inflection point in the velocity profile is considered as an indication of the importance of considering this energy in wind tunnel modeling. Time did not allow development of the instrumentation, data translation, and analysis of the other terms of the turbulent energy budget equation (A1.72). Theoretical estimates (28) have been made of their relative strength in high Reynolds number boundary layer flow.

The viscous dissipation is due to small scale turbulence while energy production is due to large scale turbulence. The direct measure of the large scale energy production and the development of instruments to measure the turbulent pressure diffusion as functions of various roughness configurations would supply useful data to the significance of these energy sources in both wind tunnel modeling and theoretical analysis.

It is recommended that further development and experimentation be given to:

(1) Instrumentation to measure the turbulent pressure diffusion, $(1/\rho)(\partial \overline{u'_j p'}/\partial x_j)$, of the turbulent energy equation (Al.72). Roughness geometry in the wind tunnel could be designed and controlled to allow observation during high Reynolds number flow of the variation in turbulent pressure diffusion as compared to turbulent dissipation and production.

(2) After the development and operation of the turbulent pressure diffusion instrumentation and analysis is completed in the wind tunnel, further tests of simple prototype topographies should be conducted to compare to the wind tunnel models. This will supply useful information on the relative importance of the various turbulent energies that are dominant in high Reynolds number flow as well as offer scaling ranges for further improvement of similarity conditions in wind tunnel model studies.

BIBLIOGRAPHY

1. Ailleret, P. "L'energie Éo lienne: Sa Valeur et la prospection des sites", Revué Genérale D'électricité (1946).

2. Archibald, E. D. "The increase in the velocity of the wind with the altitude", Nature, Vol. 27 (1883).

3. Batchelor, G. K. "Note on free turbulent flows, with special reference to the two-dimensional wake", Journal of Aeronautical Sciences, Vol. 17, 441 (1950).

4. Batchelor, G. K. "The conditions for dynamical similarity of motions of a frictionless perfect-gas atmosphere", Quarterly Journal of the Royal Meteorological Society, 79, 224 (1953).

5. Batchelor, G. K. "The theory of homogeneous turbulence", Cambridge Univ. Press (1953).

6. Bourke, R.H., Glenne, B. and Adams, B.W. "The nearshore physical oceanographic environment of the Pacific N.W. coast", OSU Dept. of Oceanography Ref. 74-45, Corvallis, OR. (1971).

7. Bradley, E.F. "A micrometeorological study of velocity profiles and surface drag in the region modified by a change in surface roughness", Quarterly Journal of the Royal Meterological Society, 94, 361 (1968).

8. Bradshaw, P. "The understanding and prediction of turbulent flow", Aeronautical Journal of the Royal Aeronautical Society, 76, 403 (1972).

9. Cermak, J.E. "Simulation of atmospheric motion by wind tunnel flows", CER66JEC-VAS-EJP GJB-HC-RNM-SI17 Colorado State University, Fort Collins, Colo. (1966).

10. Cermak, J.E. "Wind tunnel simulation of atmospheric flow and dispersion", Proceedings from Workshop on Inadvertant Weather Modification, Utah State Univ. (1973).

11. Davenport, A.G. "The relationship of wind structure to wind loading." Symposium No. 16, Wind effects on buildings and structures Vol. 1, Her Majesty's Stationery Office, London (1965).

12. Donaldson, C. "Calculation of turbulent shear flows for atmospheric and vortex motion", Journal of the American Institute of Aeronautics and Astronautics, 10, 4, (1972).

13. Elliott, W.P. "The growth of the atmospheric internal boundary layer", Transactions of the American Geophysical Union, 38, p. 1048 (1958).

14. Field, J.H. and Warden, R. "A survey of air currents in the Bay of Gibralter", Geophysical Memoirs, No. 59, Published by Her Majesty's Stationery Office (1929).

15. Frenkiel, J. "Wind flow over hills in relation to wind power utilization", Technion Research and Development Foundation Ltd. Haifa, Israel (1961).

16. Friedlander, S.K. and Topper, L. (editors) "Turbulence: Classical papers on statistical theory", Interscience, New York (1962).

17. Georgii, W. "Beitrag zum Stromfeld der Luft im Luv von Gebirgen", Veioffder Forschungs-Institut. No. 1 (1926).

18. Giblett, M.A. "The structure of wind over level country", Meteorological Office Geophysical Memoir, No. 54, Vol. VI (1932).

19. Gibson, M.M. "Spectra of turbulence at high Reynolds number", Nature, 195, p. 1281 (1962).

20. Gibson, M.M. "Spectra of turbulence in a round jet", Jr. of Fluid Mechanics, 15, p. 161 (1963).

21. Golding, E.W. "The generation of electricity by wind power", Philosophical Library, Inc., New York (1955).

22. Grant, H.L., Stewart, R.W. and Moilliet, A. "Turbulence spectra from a tidal channel", Jr. of Fluid Mechanics 12, p. 241 (1962).

23. Hellmann, G. "Uber die Bewegung der Luft in den untersten Schichten der Atmosphare", Meteorologie Zeitschrift, Vol. 34, 273 (1917).

24. Hewson, E.W. "Generation of power from the wind", Bulletin of the Am. Meteor. Society, Vol. 56, No. 7, D 660 (1975).

25. Hewson, E.W., Baker, R.W. and Brownlow, R.W. "Wind power potential in selected areas of Oregon", Oregon State University Report PUD 75-3 Corvallis, OR (1975).

26. Launder, B.E., Reece, G.J. and Rodi, W. "Progress in the development of the Reynolds stress closure", Journal of Fluid Mechanics, 68, pt 3, 537 (1975).

27. Lettau and Davidson. "Exploring the atmosphere's first mile", Vol. 2, Pergamon Press, London (1957).

28. Lumley and Panofsky. "The tructure of urbulence", Interscience Division of John Wiley and Sons Ltd., New York (1964).

29. Monin, A.S. and Obukhov, A.M. "Basic laws of turbulent mixing in the atmosphere near the ground", Akademia Nauk SSR, Trudy Inst. Teoreticheskoi Geofiziki, No. 24, 163, (1954).

30. Ogawa, Y., Griffiths, R. and Hoydysh, W.G. "A wind tunnel study of sea breeze effects", Boundary Layer Meteorology, 8, No. 2, 141 (1975).

31. Organization for European Economic Cooperation, Vol. II of the Final Report of the Proceedings of the Working Group No. 2 Wind Power (1954).

32. Paeschke, W. "Experimentelle Untersochungen Zum Rauhigkeits-und Stabilitäts-problem", Beitrage vur Physik freien Atmosphäre Vol. 24, 163 (1937).

33. Panofsky, H.A. "The atmospheric boundary layer below 150 meters", Annual Review of Fluid Mechanics, Vol. 6 (1974).

34. Petersen, E.W. "Modification of mean flow and turbulence energy by a change in surface roughness under conditions of neutral stability", Quarterly Jr. of the Royal Met. Soc., 95, 561 (1969).

35. Petersen, E. W. and Taylor, P. A. "Some comparisons between observed wind profiles at Risø and theoretical predictions for flow over inhomogeneous terrain", Quarterly Journal of the Royal Meteorological Society, 99, 329 (1973).

36. Petersen, E. W. "The Risø profiles: a study of wind and temperature data from the 123 m tower at Risø, Denmark", Quarterly Journal of the Royal Meteorological Society, 101, 107 (1975).

37. Petersen, E. W., Kristensen, L. and Chang-Chun Su. "Some observations and analysis of wind over non-uniform terrain", to be published in the Quarterly Journal of the Royal Meteorological Society - after April 1976.

38. Plate, E. J. "Aerodynamic characteristics of atmospheric boundary layers", U.S. Atomic Energy Commission, Oak Ridge, Tennessee (1971).

39. Pond, S., Stewart, R. W. and Burling, R. W. "Turbulence spectra in wind over waves", Journal of Atmospheric Science 20, p. 319 (1963).

40. Prandtl, L. "Uber die ausgebildete Turbulenz", Zeitschrift für angewandte Mathematik und Mechanik, Berlin, Germany, 5, 136-139 (1925).

41. Prandtl, L. "Uber ein neus Formelsystem der ausgebildeten Turbulenz", Nachr. Akad. Wiss. Göttingen 6-19 (1945).

42. Putnam, P. C. "Power from the wind", D. Van Nostrand Co., Inc., New York (1948).

43. Ruggles, K. W. "Observations of the wind field in the first ten meters of the atmosphere above the ocean", Ph. D. Thesis, Massachusetts Inst. of Technology, Cambridge, Mass. 1969.

44. Schlichting, H. "Boundary layer theory", McGraw-Hill Book Co., Inc., New York (1968).

45. Shir, C. C. "A numerical computation of air flow over a sudden change of surface roughness", Journal of the Atmospheric Sciences, 29, 304 (1972).

46. Steiner, R. and Severe, R.H. "Some measured characteristics of severe storm turbulence", American Meteorological Society Severe Storms Conference, Norman, Okla. Feb. 13-15 (1962).

47. Sutton, O.G. "Micrometeorology", McGraw-Hill Book Co., Inc., New York (1953).

48. Taylor, G.I. "Statistical theory of turbulence", Proceedings of the Royal Society of London, A151, p. 421 (1935).

49. Taylor, G.I. "Correction measurements in a turbulent flow through a pipe", Proceedings of the Royal Society of London, A157, p. 537 (1936).

50. Tennekes, H. and Lumley, J.L. "A first course in turbulence", The MIT Press, Cambridge, Mass. (1972).

51. Thuillier, R.H. and Lappe, U.O. "Wind and temperature profile characteristics from observations on a 1400 ft. tower", Jr. of Applied Meteorology, Vol. 3 (1964).

52. Weiler, H.S. and Burling, R.W. "Direct measurements of stress and spectra of turbulence in the boundary layer over the sea", Journal of The Atmospheric Sciences, 24, p. 653 (1967).

53. Welty, J.R., Wicks, C.E. and Wilson, R.E. "Fundamentals of momentum, heat and mass transfer", John Wiley and Sons, Inc., New York (1969).

54. Williams, R.M. Jr. "High frequency temperature and velocity fluctuations in the atmospheric boundary layer", Ph.D. Thesis, Oregon State Univ., Corvallis, Oregon (1974).

55. Wyngaard, J.C. "Modeling the planetary boundary layer, extension to the stable case", Boundary Layer Meteorology, 9, No. 4, 441, 1975.

56. Wyngaard, J.C., Cote, O.R. and Rao, K.S. "Modeling the atmospheric boundary layer", Advances in Geophysics, 18A, 193 (1974).

APPENDICES

APPENDIX A

Aerodynamic Characteristics of the Atmospheric Boundary Layer

The Atmosphere at Rest

The atmosphere consists of a hypothetical gas known as clean dry air and the gas water vapor. Other impurities such as gases produced by man and suspended matter will not be considered. This allows application of ideal gas mixture relations with good correlation to atmospheric phenomena.

The static atmosphere can be defined in terms of density, pressure, and absolute temperature as functions of height. Combining the hydrostatic equation:

$$\frac{dp}{dz} = -g\rho \tag{A1.1}$$

and the ideal gas relation for a dry atmosphere:

$$\rho = \frac{p}{RT} \tag{A1.2}$$

we obtain the variation of pressure with height:

$$p = p_o \exp\left(- \frac{g}{R} \int_0^Z \frac{dz}{T} \right) \tag{A1.3}$$

and the variation of density with height:

$$\frac{1}{\rho}\frac{d\rho}{dz} = - \frac{1}{T}\left[\frac{g}{R} + \frac{dT}{dz}\right] \tag{A1.4}$$

The variation of temperature with height cannot be expressed directly in a general equation but must be considered in terms of simple limiting conditions. A volume of dry air in a static atmosphere will have the variables of temperature, pressure, and density controlled by the equation of state (Al. 2). The temperature may be changed by variation in pressure, entrainment of external air during motion of the volume, conduction of heat to or from the volume, and by radiation. This problem can be considerably simplified without any large error if we consider adiabatic changes only. This allows the change in temperature to become a function of pressure changes. Beginning with the first law of thermodynamics:

$$\delta Q = C_v dT + pd(\frac{1}{\rho}) \qquad (A1.5)$$

and using the equation of state (Al. 2):

$$\delta Q = C_p dT - \frac{dp}{\rho} \qquad (A1.6)$$

For adiabatic processes, this reduces to:

$$C_p dT = \frac{dp}{\rho} = RT(\frac{dp}{p}) \qquad (A1.7)$$

With time rate of change:

$$\frac{C_p}{T}\left(\frac{dT}{dt}\right) = \left(\frac{R}{P}\right)\frac{dp}{dt} \tag{A1. 8}$$

results in the expression:

$$C_p d \ln T = Rd \ln p \tag{A1. 9}$$

which can be integrated:

$$\frac{T_o}{T} = \left(\frac{P_o}{P}\right)^{R/C_p} \tag{A1. 10}$$

This expression is valid for dry air brought adiabatically from its existing pressure to a standard pressure. From this, we define potential temperature (θ) using a standard surface pressure P_o = 1000 mb:

$$\theta = T\left(\frac{1000}{P}\right)^{R/C_p} \tag{A1. 11}$$

The rate at which temperature decreases vertically in the atmosphere is called "lapse rate" (Γ). In micrometeorology an approximation for potential temperature in the surface layers (less than 100 m) is:

$$\theta = T + \Gamma Z \tag{A1. 12}$$

The discussion up to now has concerned dry air. When the vapor pressure of moist air reaches the saturation vapor pressure, the relative humidity is defined as 100%.

The conditions of this experiment will be considered for relative humidity less than 100%. The specific heat at constant pressure of unsaturated moist air is only slightly higher than the specific heat for dry air. Therefore, equation (A1. 11) will be used.

The conditions postulated in the previous analysis are approached when there is a moderate or high wind and the radiation energy exchange between ground and air is low due to cloud cover. In the case of this experiment, we must consider the ocean-land heat exchange continuum. The heat exchange on a clear day over the sea near the Oregon coast is positive (heat transfer to the sea) during the summer months and negative during winter months (6).

Over land, during summer daylight, there is a transfer of heat to the air (27). The variables of relative mass and surface area of sea and land, wind velocities, turbulence and moisture content all affect heat transfer exchange at this complex interface. To determine if vertical movements of the air are caused by dynamic instability rather than buoyancy, we observe the temperature gradient with reference to the adiabatic lapse rate. When they approach each other, the conditions of the analysis are sustained. This condition was observed for this experiment.

The Atmosphere in Laminar Motion

Before developing the fluid equations necessary for this model, we must define the conditions. The dynamic atmosphere can be more conveniently modeled by defining layers dominated by friction or geostrophic relationships (Coriolis force and pressure gradient force). The surface boundary layer (about 100 m) is the region of constant shear stress with wind structure determined by the nature of the surface and the vertical gradient of temperature (47). Above this is a transition region where the shear stress is a variable and Coriolis force affects the wind structure (up to 1000 m). Finally, the free atmospheric layer has air motion that is inviscid and in geostrophic balance. This experiment is limited to the surface boundary layer. Panofsky (33) has pointed out that turning of the wind (Ekman spiral) can be neglected in this layer.

The primitive equations of fluid flow, relative to this experiment, result from three principles:

1. The conservation of mass
2. Newtons second law of motion
3. The first law of thermodynamics.

The application of the first and second principles results in the Navier-Stokes equations for laminar, compressible flow with constant viscosity. Application of the third principle results in the thermal energy equation. Development and discussion of the use of this equation will be delayed to later in this section.

The Navier-Stokes equations for a Cartesian coordinate system are:

$$\rho\left(\frac{\partial u}{\partial t} + u\frac{\partial u}{\partial x} + v\frac{\partial u}{\partial y} + w\frac{\partial u}{\partial z}\right) = \rho X - \frac{\partial p}{\partial x} + \mu\left(\frac{\partial^2 u}{\partial x^2} + \frac{\partial^2 u}{\partial y^2} + \frac{\partial^2 u}{\partial z^2}\right) \quad \text{(A1. 13a)}$$

$$\rho\left(\frac{\partial v}{\partial t} + u\frac{\partial v}{\partial x} + v\frac{\partial v}{\partial y} + w\frac{\partial v}{\partial z}\right) = \rho Y - \frac{\partial p}{\partial y} + \mu\left(\frac{\partial^2 v}{\partial x^2} + \frac{\partial^2 v}{\partial y^2} + \frac{\partial^2 v}{\partial z^2}\right) \quad \text{(A1. 13b)}$$

$$\rho\left(\frac{\partial w}{\partial t} + u\frac{\partial w}{\partial x} + v\frac{\partial w}{\partial y} + w\frac{\partial w}{\partial z}\right) = \rho Z - \frac{\partial p}{\partial z} + \mu\left(\frac{\partial^2 w}{\partial x^2} + \frac{\partial^2 w}{\partial y^2} + \frac{\partial^2 w}{\partial z^2}\right) \quad \text{(A1. 13c)}$$

The X, Y, and Z terms are the components of external forces per unit mass in the x, y, and z coordinate directions, respectfully. The equation of continuity for a homogeneous, incompressible fluid is:

$$\frac{\partial u}{\partial x} + \frac{\partial v}{\partial y} + \frac{\partial w}{\partial z} = 0 \quad \text{(A1. 14)}$$

In the transition region, the external force terms are gravity and Coriolis:

$$X = +g\frac{\partial h}{\partial x} - 2\omega(w \sin\phi - v \sin\phi) \quad \text{(A1. 15a)}$$

$$Y = +g\frac{\partial h}{\partial y} - 2\omega\, u \sin\phi \quad \text{(A1. 15b)}$$

$$Z = -g \frac{\partial h}{\partial z} - 2\,\omega\, u \cos \phi \qquad \text{(A1. 15c)}$$

The axes system used in the above equations is fixed to the earth and oriented so that the positive directions are: the "x" axis horizontal toward the east, the "y" axis horizontal toward the north, and the "z" axis vertical outward from the earth surface. The latitude of the air particle is ϕ and the earth's angular velocity of rotation is ω. Vertical distance is "h".

The form of the Navier-Stokes equations for the transition layer, using vector notation is:

$$\rho \frac{D\underline{V}}{Dt} = \rho g - \rho 2\omega \underline{K} \times \underline{V} - \nabla p + \mu \nabla^2 \underline{V} \qquad \text{(A1. 16)}$$

and for the surface boundary layer:

$$\rho \frac{D\underline{V}}{Dt} = \rho \underline{g} - \nabla p + \mu \nabla^2 \underline{V} \qquad \text{(A1. 17)}$$

<u>Development of Similarity Parameters for the Momentum Equation</u>

The Coriolis term contains the unit vector $(\underline{K})$ in the direction of the axis of rotation. Casting these equations in a form for dynamic similitude requires defining dimensionless parameters:

$$\omega_i^* = \frac{\omega_i}{\omega_o}$$

$$\underline{V}^* = \frac{\underline{V}_i}{V}$$

$$P^* = \frac{p}{\rho_o V^2}$$

$$t^* = \frac{tV}{L}$$

$$x_i^* = \frac{X}{L}$$

$$\underline{g}_i^* = \frac{g_i}{g_o}$$

$$\rho^* = \frac{\rho}{\rho_o}$$

Inserting these terms in equation (A1. 16), will form a dimensionless expression convenient for system analysis and model studies.

$$\left(\frac{V^2}{L}\right) \frac{D\underline{V}_i^*}{Dt^*} = \frac{\Delta\gamma}{\gamma_o} g_o \underline{g}^* - \omega_o V(2\omega^* \underline{K} \times \underline{V}^*) - \frac{V^2}{L} \frac{\nabla^* P^*}{\rho^*} + \left(\frac{V\nu}{L^2}\right) \nabla^{*2} \underline{V}^* \tag{A1. 18a}$$

Multiply through by L/V^2:

$$\frac{D\underline{V}_i^*}{Dt^*} = \frac{Lg_o}{V^2}\left(\frac{\Delta\gamma}{\gamma_o}\right) \underline{g}^* - \left(\frac{\omega_o L}{V}\right) 2\omega^* \underline{K} \times \underline{V}^* - \frac{1}{\rho^*} \nabla^* P^* + \left(\frac{\nu}{LV}\right) \nabla^{*2} \underline{V}^* \tag{A1. 18b}$$

$$\frac{D\underline{V}_i^*}{Dt^*} = \frac{1}{Fr}\,\underline{g}^* - \frac{1}{Ro}\,2\omega^*\underline{K} \times \underline{V}^* - \frac{1}{\rho^*}\,\nabla^* P^* + \frac{1}{Re}\,\nabla^{*2}\underline{V}^* \qquad \text{(A1. 18c)}$$

The nondimensional numbers in equation (A1. 18c) are:

$$Fr = \frac{V^2}{g_o L(\Delta\gamma/\gamma_o)} \qquad \text{(A1. 19a)}$$

$$Ro = \frac{V}{L\omega_o} \qquad \text{(A1. 19b)}$$

$$Re = \frac{VL}{\nu} \qquad \text{(A1. 19c)}$$

The specific weight (γ) is primarily a function of temperature for the vertical distances in the boundary layer. This allows the Froude number to be:

$$Fr = \frac{-(V/L)^2}{g_o/T_o(\Delta T/L)} \qquad \text{(A1. 20)}$$

When considering an atmospheric layer of finite thickness, we can write the nondimensional gradient Richardson number (9, 38):

$$Ri = \frac{g_o}{T_o}\,\frac{(\Delta T/L)}{(V/L)^2} \qquad \text{(A1. 21)}$$

This is clearly related to the Froude number. Prandtl has shown that the stability of stratified flows depends on the Richardson number (44), in addition to the Reynolds number, since it is the ratio of buoyant forces to inertial forces. Richarson number similarity requires temperature gradient control in the wind tunnel for all conditions except near-neutral.

The near-neutral condition has been defined (28) as: $|Ri| \leq .03$. Observed values of Richardson number between 1 and 5 meters over the ocean meet the near-neutral condition (43). Yaquina Head extends about 1.5 Km from the mainland and, due to its relatively small land area compared to the surrounding water, is dominated by the inertial force of the ocean wind over the buoyant force caused by thermal gradients over land. Measurements of Richardson number at Yaquina Head for winds greater than 6 m/s (range of interest for wind power (21)) indicate the near-neutral condition is satisfied (Table 4.7).

The Rossby number is the ratio of the magnitude of acceleration compared to the Coriolis force. For large Rossby numbers, Coriolis effects can be ignored. Local accelerations dominate Coriolis accelerations for flows over distances less than 150 Km (9). This is important for model studies since it allows small error due to unequal Rossby numbers when model flow scales are less than 150 Km.

The Reynolds number is the ratio of momentum forces to viscous forces. For laminar flows, the ratio of prototype to model is typically 10^2 to 10^4. This appears to be an insurmountable problem until we determine the dominant flow characteristics. For the range of average velocities useful for wind power, the flow is turbulent. The turbulent contribution to shear stress is much greater than the molecular contribution, except near the surface (53). Therefore, greater possibilities exist for Reynolds similarity in turbulent flow.

Thermal Energy Equation

The thermal energy equation for the surface boundary layer is derived from the first law of thermodynamics:

$$\frac{\delta Q}{\partial t} - \frac{\delta W}{\partial t} = \iint_{CS} (e + \frac{p}{\rho})\rho(\underline{V}\cdot\underline{n})dA + \frac{\partial}{\partial t}\iiint_{CV} e\rho dV_L \qquad (A1.22)$$

where Q is heat flux, W is shear work, e is potential, kinetic, and internal energy, A is control surface area and V_L is the control volume.

More specifically, we define terms as follows:

Conduction into a control volume:

$$\frac{\delta Q}{\partial t} = \iint_{CS} (K_T \nabla T\cdot\underline{n})dA \qquad (A1.23)$$

where K_T is thermal conductivity.

Work terms including shear and normal stress:

$$-\frac{\delta W}{\partial t} - \iint_{CS} p(\underline{V} \cdot \underline{n}) dA = \iint_{CS} (\underline{V} \cdot \underline{\tau}) dA \tag{A1.24}$$

where $\underline{\tau}$ is the stress tensor.

The energy terms collectively are:

$$\iint_{CS} e\rho(\underline{V} \cdot \underline{n}) dA + \frac{\partial}{\partial t} \iiint_{CV} e\rho dV_L \tag{A1.25}$$

Defining a stress function for each coordinate to simplify notation we have:

$$\underline{f}_1 = \tau_{xx}\,\underline{x} + \tau_{yx}\,\underline{y} + \tau_{zx}\,\underline{z} \tag{A1.26a}$$

$$\underline{f}_2 = \tau_{xy}\,\underline{x} + \tau_{yy}\,\underline{y} + \tau_{zy}\,\underline{z} \tag{A1.26b}$$

$$\underline{f}_3 = \tau_{xz}\,\underline{x} + \tau_{yz}\,\underline{y} + \tau_{zz}\,\underline{z} \tag{A1.26c}$$

This allows rewriting (1.24):

$$\iint_{CS} (\underline{V} \cdot \underline{\tau}) dA = \iint_{CS} (u\underline{f}_1 + v\underline{f}_2 + w\underline{f}_3) \cdot \underline{n} dA \tag{A1.27}$$

Applying the divergence theorem to equations (A1.23), (A1.27) and the first term of (A1.25) then substituting the result into (A1.22) we obtain:

$$\iiint_{CV} [-\nabla \cdot K_T \nabla T - \nabla \cdot (u\underline{f}_1 + v\underline{f}_2 + w\underline{f}_3) + \nabla \cdot e\rho \underline{V} + \frac{\partial}{\partial t} e\rho] dV_L = 0 \tag{A1.28}$$

This equation requires the integrand vanish for a finite volume:

$$e[\frac{\partial \rho}{\partial t} + \nabla \cdot \rho \underline{V}] + \rho[\frac{\partial e}{\partial t} + \underline{V} \cdot \nabla e] - \nabla \cdot K_T \nabla T$$

$$- [u\nabla \cdot \underline{f}_1 + V\nabla \cdot \underline{f}_2 + w\nabla \cdot \underline{f}_3] - [\underline{f}_1 \cdot \nabla u + \underline{f}_2 \cdot \nabla v + \underline{f}_3 \cdot \nabla w] = 0 \tag{A1.29}$$

Expanding the x-component of the fourth term:

$$u\underline{\nabla} \cdot \underline{f}_1 = u[\frac{\partial \tau_{xx}}{\partial x} + \frac{\partial \tau_{yx}}{\partial y} + \frac{\partial \tau_{zx}}{\partial z}] \tag{A1.30}$$

Which, according to equation (A1.13) is:

$$u(\rho \frac{Du}{Dt} - \rho g_x) \tag{A1.31}$$

Similar relations hold for the y and z components resulting in the fourth term of (A1.29) appearing as:

$$\rho \frac{D}{Dt} (\frac{V^2}{2}) - \rho \underline{V} \cdot \underline{g} \tag{A1.32}$$

Using this information and noting that conservation of mass requires the first term of (A1.29) to equal zero, we write (A1.29) with energy term (e) divided into its components as:

$$\rho\left[\frac{DE}{Dt} + \frac{D}{Dt}\left(\frac{V^2}{2}\right) - \underline{V}\cdot\underline{g}\right] - \nabla\cdot K_T\nabla T - \rho\frac{D}{Dt}\frac{V^2}{2} + \rho\underline{V}\cdot\underline{g}$$

$$- [\underline{f}_1\cdot\nabla u + \underline{f}_2\cdot\nabla v + \underline{f}_3\cdot\nabla w] = 0 \qquad \text{(A1.33)}$$

Here, internal energy is E. Simplifying (A1.33) further:

$$\rho\frac{DE}{Dt} - \nabla\cdot K_T\nabla T - [\underline{f}_1\cdot\nabla u + \underline{f}_2\cdot\nabla v + \underline{f}_3\cdot\nabla w] = 0 \qquad \text{(A1.34)}$$

Using the stress relations of equations (A1.24) and (A1.25) for f_1, f_2, f_3, equation (A1.34) reduces to the final form of the thermal energy equation:

$$\rho\frac{DE}{Dt} = \nabla\cdot K_T\nabla T - p\nabla\cdot\underline{V} + \mu\Phi \qquad \text{(A1.35)}$$

The dissipation function is:

$$\Phi = -\frac{2}{3}(\nabla\cdot\underline{V})^2 + 2\left[\left(\frac{\partial u}{\partial x}\right)^2 + \left(\frac{\partial v}{\partial y}\right)^2 + \left(\frac{\partial w}{\partial z}\right)^2\right]$$

$$+ \left[\left(\frac{\partial u}{\partial y} + \frac{\partial v}{\partial x}\right)^2 + \left(\frac{\partial v}{\partial z} + \frac{\partial w}{\partial y}\right)^2 + \left(\frac{\partial w}{\partial x} + \frac{\partial u}{\partial z}\right)^2\right] \qquad \text{(A1.36)}$$

The first and second terms of (A1.36) represent the viscous part of the normal stresses, and the third bracketed term represents the shear stress. For incompressible flow, $\nabla\cdot\underline{V} = 0$, the first term is omitted and the dissipation function is designated Φ'.

For the conditions of constant heat capacity and constant thermal conductivity, equation (A1.35) will be:

$$\rho C_p \frac{DT}{Dt} = K_T \nabla^2 T - p \nabla \cdot \underline{V} + \mu \Phi \tag{A1.37}$$

In order to apply the principle of similarity, we define a dimensionless temperature:

$$\theta^* = \frac{T - T_\infty}{T_w - T_\infty} = \frac{T - T_\infty}{(\Delta T)_o} \tag{A1.38}$$

Denoting the other dimensionless quantities by asterisks, the steady flow, two dimensional form of equation (A1.37) is:

$$\rho^*(u^* \frac{\partial \theta^*}{\partial x^*} + V^* \frac{\partial \theta^*}{\partial y^*}) = \frac{K_T}{\rho_o C_p U_o L} (\frac{\partial^2 \theta^*}{\partial x^{*2}} + \frac{\partial^2 \theta^*}{\partial y^{*2}})$$

$$+ \frac{U_o^2}{C_p (\Delta T)_o} [u^* \frac{\partial P^*}{\partial x^*} + v^* \frac{\partial P^*}{\partial y^*}] + \frac{\mu U_o}{\rho_o C_p L (\Delta T)_o} \Phi^*$$

(A1.39)

The dimensionless dissipation function is here defined by:

$$\Phi^* = 2[(\frac{\partial u^*}{\partial x^*})^2 + (\frac{\partial v^*}{\partial y^*})^2] + (\frac{\partial u^*}{\partial y^*} + \frac{\partial v^*}{\partial x^*})^2 + (\frac{\partial v^*}{\partial z^*})^2 + (\frac{\partial u^*}{\partial z^*})^2$$

Development of Similarity Parameters for the Thermal Energy Equation

The solution of equation (A1.39) depends on the three non-dimensional quantities:

a. $\dfrac{K_T}{\rho_o C_p U_o L}$

b. $\dfrac{U_o^2}{C_p(\Delta T)_o}$

c. $\dfrac{\mu U_o}{\rho_o C_p L(\Delta T)_o}$

Quantity (a) can be rearranged:

$$\frac{K_T}{\rho_o C_p U_o L} = \frac{\alpha}{U_o L} = \left(\frac{\alpha}{\nu}\right)\frac{\nu}{U_o L} = \frac{1}{Pr}\,\frac{1}{Re}$$

Here, thermal diffusivity is defined as:

$$\alpha = \frac{K_T}{\rho_o C_p}$$

and Prandtl number as:

$$Pr = \frac{\nu}{\alpha} = \frac{\mu C_p}{K_T}$$

For air, $Pr = 0.7$ in the temperature and pressure range of this experiment and quantity (a) reduces to:

$$\frac{1.43}{Re}$$

Quantity (b) is the Eckert number:

$$Ec = \frac{U_o^2}{C_p(\Delta T)_o}$$

The Eckert number leads directly to the temperature increase through adiabatic compression and is only significant at velocities approaching the speed of sound (44).

Quantity (c) can be simplified by separating terms into Eckert and Reynolds numbers:

$$\frac{\mu U_o}{\rho_o C_p L(\Delta T)_o} = \frac{\mu}{U_o L \rho_o} \frac{U_o^2}{C_p(\Delta T)_o} = \frac{Ec}{Re} \qquad \text{(A1. 40)}$$

Now, the dimensionless form of the two dimensional, steady flow, constant properties, thermal energy equation for air is:

$$U^* \frac{\partial \theta^*}{\partial x^*} + V^* \frac{\partial \theta^*}{\partial y^*} = \frac{1}{Pr\ Re} \left(\frac{\partial^2 \theta^*}{\partial x^{*2}} + \frac{\partial^2 \theta^*}{\partial y^{*2}} \right) \qquad \text{(A1. 41)}$$

Summary of Equations

Momentum

$$\frac{DV_i^*}{Dt^*} = \frac{1}{Re} \nabla^{*2} V_i^* - \frac{1}{\rho^*} \nabla^* P_i^* \qquad \text{(A1.42)}$$

Continuity

$$\nabla V_i^* = 0 \qquad \text{(A1.43)}$$

Thermal energy (two dimensional and steady)

$$u^* \frac{\partial \theta^*}{\partial x^*} + w^* \frac{\partial \theta^*}{\partial z^*} = \frac{1}{Pr\ Re} \left(\frac{\partial^2 \theta^*}{\partial x^{*2}} + \frac{\partial^2 \theta^*}{\partial z^{*2}} \right) \qquad \text{(A1.44)}$$

Further simplifications can be made by examining the order of magnitude of the terms in these equations. For two-dimensional motion, equations (A1.42) and (A1.43) are explicitly expressed as follows:

$$\frac{\partial u^*}{\partial t^*} + u^* \frac{\partial u^*}{\partial x^*} + w^* \frac{\partial u^*}{\partial z^*} = \frac{1}{Re} \left(\frac{\partial^2 u^*}{\partial x^{*2}} + \frac{\partial^2 u^*}{\partial z^{*2}} \right) - \frac{1}{\rho^*} \frac{\partial P^*}{\partial x^*} \qquad \text{(A1.45)}$$

$$\frac{\partial w^*}{\partial t^*} + u^* \frac{\partial w^*}{\partial x^*} + w^* \frac{\partial w^*}{\partial z^*} = \frac{1}{Re} \left(\frac{\partial^2 w^*}{\partial x^{*2}} + \frac{\partial^2 w^*}{\partial z^{*2}} \right) - \frac{1}{\rho^*} \frac{\partial P^*}{\partial z^*} \qquad \text{(A1.46)}$$

$$\frac{\partial u^*}{\partial x^*} + \frac{\partial w^*}{\partial z^*} = 0 \qquad \text{(A1.47)}$$

For the steady state, the results are Prandtl's equations for the boundary layer in steady flow (47):

$$u^* \frac{\partial u^*}{\partial x^*} + w^* \frac{\partial u^*}{\partial z^*} = \frac{1}{Re} \frac{\partial^2 u^*}{\partial z^{*2}} - \frac{1}{\rho^*} \frac{\partial P^*}{\partial x^*} \tag{A1.48}$$

$$\frac{\partial P^*}{\partial z^*} = 0 \tag{A1.49}$$

$$\frac{\partial u^*}{\partial x^*} + \frac{\partial w^*}{\partial z^*} = 0 \tag{A1.50}$$

The equations of laminar flow for steady, incompressible, viscous conditions are (A1.44), (A1.48), (A1.49) and (A1.50). The problems of modeling these equations in the wind tunnel were previously mentioned for the momentum equation. However, a set of parameters useful in aerodynamics can be used to describe wind profiles in the atmospheric boundary layer. These parameters are the shear velocity, u_*, and roughness height Z_o. The shear velocity is obtained from the wall shear stress τ_o with the relation:

$$u_* = (\tau_o / \rho)^{1/2} \tag{A1.51}$$

In meteorology, the parameters u_* and Z_o are determined from measured velocity profiles by assuming the profiles to be described by the logarithmic law of Prandtl:

$$\ln(z) = \left(\frac{k}{u_*} \right) u(z) + \ln(Z_o) \tag{A1.52}$$

where z is the height above the boundary, V(z) the mean wind at height z, and k is von Karman's constant, approximately equal to 0.4 (38). The validity of this law for flow over the ocean was demonstrated up to Z = 10 meters (43). The method of modifying the wind tunnel to obtain similar profiles was described in the section on test method. Both adiabatic and superadiabatic conditions were considered for these profiles.

Equation (A1.52) is applicable for adiabatic conditions, i.e., equation (A1.10).

For superadiabatic conditions, i.e., a lapse rate greater than 1°C/100 m, the Monin-Obukhov expansion of (A1.52) is:

$$u = \frac{u_*}{k} \left(\ln \frac{z}{Z_o} + \alpha \frac{z}{L} \right) \tag{A1.53}$$

where α is an empirical constant and:

$$L = - \frac{\rho u_*^3 C_p T}{kgH} \tag{A1.54}$$

T = absolute average temperature

H = average heat flux

For the wind conditions near the ground of interest to wind power generation, the value of $\alpha(z/L)$ is small in comparison with $\ln(z/Z_o)$ so that superadiabatic wind profiles do not differ greatly from the adiabatic (51).

Further conditions for boundary layer flow related to this atmospheric model were the large forced flow forces compared to the weaker buoyancy forces and the assumption that $\partial P/\partial x$ is very small relative to momentum forces. This results in the final form of the laminar boundary layer equations (dropping the asterisk):

$$u\frac{\partial u}{\partial x} + w\frac{\partial u}{\partial z} = \frac{1}{Re}\frac{\partial^2 u}{\partial z^2} \qquad \text{(A1.55a)}$$

$$u\frac{\partial \theta}{\partial x} + w\frac{\partial \theta}{\partial z} = \frac{1}{Pr\ Re}\frac{\partial^2 \theta}{\partial z^2} \qquad \text{(A1.55b)}$$

$$\frac{\partial u}{\partial x} + \frac{\partial w}{\partial z} = 0 \qquad \text{(A1.55c)}$$

A final consideration will simplify the equations necessary for modeling in the wind tunnel.

If we differentiate equation (A1.11) with respect to altitude, we obtain:

$$\frac{1}{\theta}\frac{\partial \theta}{\partial z} = \frac{1}{T}\frac{\partial T}{\partial z} - \frac{R}{C_p p}\frac{\partial p}{\partial z} \qquad \text{(A1.56)}$$

The lapse rate was previously mentioned. It is defined as:

$$\Gamma = -\frac{\partial T}{\partial z}$$

Using the hydrostatic equation (Al. 1) and the adiabatic lapse rate Γ_A in equation (Al. 55b) we arrive at the relation:

$$\frac{\partial \theta}{\partial z} = \frac{\theta}{T}(\Gamma - \Gamma_A) \qquad \text{(Al. 57)}$$

For neutral conditions: $\Gamma = \Gamma_A$ and therefore:

$$\frac{\partial \theta}{\partial z} = 0$$

For the neutral conditions of this experiment, equation (Al. 55b) will not apply.

The Atmosphere in Turbulent Motion

Except for special conditions at low Reynolds number, the wind in the boundary layer is turbulent. Because of the randomness characteristic of turbulent flow, we must use statistical methods.

We define the instantaneous velocity as the sum of a mean velocity and a deviation from the mean:

$$u = u + u' \qquad \text{(Al.58a)}$$

$$v = v + v' \qquad \text{(Al.58b)}$$

$$w = w + w' \qquad \text{(Al.58c)}$$

Before applying these expressions in the momentum and continuity equations. some simplification can be made. Since air has a low viscosity, frictional effects are only significant in a thin layer near a rigid boundary. The velocity gradients in this layer are large. The expressions on the right side of equations (A1. 13) (without the external force term) are the normal and tangential stresses on a fluid element:

$$\rho \frac{Du}{Dt} = \frac{\partial \tau_{xx}}{\partial x} + \frac{\partial \tau_{yx}}{\partial y} + \frac{\partial \tau_{zx}}{\partial z} \qquad \text{(A1.59a)}$$

$$\rho \frac{Dv}{Dt} = \frac{\partial \tau_{xy}}{\partial x} + \frac{\partial \tau_{yy}}{\partial y} + \frac{\partial \tau_{zy}}{\partial z} \qquad \text{(A1.59b)}$$

$$\rho \frac{Dw}{Dt} = \frac{\partial \tau_{xz}}{\partial x} + \frac{\partial \tau_{yz}}{\partial y} + \frac{\partial \tau_{zz}}{\partial z} \qquad \text{(A1.59c)}$$

The normal stresses (for a monotonic gas) are:

$$\tau_{xx} = -p + 2\mu \frac{\partial u}{\partial x} - \frac{2}{3} \mu \nabla \cdot \underline{V} \qquad \text{(A1.60a)}$$

$$\tau_{yy} = -p + 2\mu \frac{\partial v}{\partial y} - \frac{2}{3} \mu \nabla \cdot \underline{V} \qquad \text{(A1.60b)}$$

$$\tau_{zz} = -p + 2\mu \frac{\partial w}{\partial z} - \frac{2}{3} \mu \nabla \cdot \underline{V} \qquad \text{(A1.60c)}$$

The tangential stresses are:

$$\tau_{yz} = \mu\left(\frac{\partial w}{\partial y} + \frac{\partial v}{\partial z} \right) \qquad \text{(A1.61a)}$$

$$\tau_{zx} = \mu\left(\frac{\partial u}{\partial z} + \frac{\partial w}{\partial x}\right) \tag{A1.61b}$$

$$\tau_{xy} = \mu\left(\frac{\partial v}{\partial x} + \frac{\partial u}{\partial y}\right) \tag{A1.61c}$$

Now equations (A1.59) may be arranged as follows:

$$\rho\frac{\partial u}{\partial t} = \frac{\partial}{\partial x}(\tau_{xx}-\rho u^2) + \frac{\partial}{\partial y}(\tau_{yx}-\rho vu) + \frac{\partial}{\partial z}(\tau_{zx}-\rho wu) \tag{A1.62a}$$

$$\rho\frac{\partial v}{\partial t} = \frac{\partial}{\partial x}(\tau_{xy}-\rho uv) + \frac{\partial}{\partial y}(\tau_{yy}-\rho v^2) + \frac{\partial}{\partial z}(\tau_{zy}-\rho wv) \tag{A1.62b}$$

$$\rho\frac{\partial w}{\partial t} = \frac{\partial}{\partial x}(\tau_{xz}-\rho uw) + \frac{\partial}{\partial y}(\tau_{yz}-\rho vw) + \frac{\partial}{\partial z}(\tau_{zz}-\rho w^2) \tag{A1.62c}$$

Inserting the instantaneous velocities and simplifying according to the properties of the operation of averaging:

$$\rho\frac{\partial \bar{u}}{\partial t} = \frac{\partial}{\partial x}(\bar{\tau}_{xx}-\rho\bar{u}^2-\rho\overline{u'^2}) + \frac{\partial}{\partial y}(\bar{\tau}_{yx}-\rho v\bar{u}-\rho\overline{v'u'})$$
$$+ \frac{\partial}{\partial z}(\bar{\tau}_{zx}-\rho\bar{w}\bar{u}-\rho\overline{w'u'}) \tag{A1.63a}$$

$$\rho\frac{\partial \bar{v}}{\partial t} = \frac{\partial}{\partial x}(\bar{\tau}_{xy}-\rho\bar{u}\bar{v}-\rho\overline{u'v'}) + \frac{\partial}{\partial y}(\bar{\tau}_{yy}-\rho\bar{v}^2-\rho\overline{v'^2})$$
$$+ \frac{\partial}{\partial z}(\bar{\tau}_{zy}-\rho\bar{w}\bar{v}-\rho\overline{w'v'}) \tag{A1.63b}$$

$$\rho \frac{\partial \bar{w}}{\partial t} = \frac{\partial}{\partial x}(\bar{\tau}_{xz} - \rho\bar{u}\bar{w} - \rho\overline{u'w'}) + \frac{\partial}{\partial y}(\bar{\tau}_{yz} - \rho\bar{v}\bar{w} - \rho\overline{v'w'})$$

$$+ \frac{\partial}{\partial z}(\bar{\tau}_{zz} - \rho\bar{w}^2 - \rho\overline{w'^2}) \qquad \text{(A1. 63c)}$$

Development of the above statistical form of the Navier-Stokes equations has been reviewed to show the relation between average viscous stresses (i. e., $\bar{\tau}_{xx}$, $\bar{\tau}_{yx}$, etc.) and the fluctuating terms (i. e., $\rho\overline{u'^2}$, $\rho\overline{v'w'}$, etc.). These terms are called Reynolds Stress and generally are more dominant than viscous stresses in turbulent motion (47).

We now define the Reynolds stresses:

$$T_{xx} = -\rho\overline{u'u'};\quad T_{yx} = -\rho\overline{v'u'};\quad T_{zx} = -\rho\overline{w'u'}$$

$$T_{xy} = -\rho\overline{u'v'};\quad T_{yy} = -\rho\overline{v'v'};\quad T_{zy} = -\rho\overline{w'v'}$$

$$T_{xz} = -\rho\overline{u'w'};\quad T_{yz} = -\rho\overline{v'w'};\quad T_{zz} = -\rho\overline{w'w'}$$

These stresses are symmetric:

$$T_{yx} = T_{xy},\quad T_{zx} = T_{xz},\quad T_{yz} = T_{zy}$$

Finally, we can identify the Reynolds stress tensor:

$$\begin{vmatrix} T_{xx} & T_{xy} & T_{xz} \\ T_{xy} & T_{yy} & T_{yz} \\ T_{xz} & T_{yz} & T_{zz} \end{vmatrix} \qquad \text{(A1. 64)}$$

The physical interpretation of these stresses is as follows: the diagonal components are normal stresses representing the additional dynamic pressure caused by the fluctuating velocity. The off-diagonal components are shear stresses. These play a dominant role in mean momentum transfer by turbulent motion.

The Energy Budget Equations

Equations (A1.63) are the statistical form of the Navier-Stokes equations, as mentioned, or sometimes known as the turbulent field equations. To identify the various forms of turbulent energy, an energy budget equation may be formed from equations (A1.13), the

For steady, incompressible flow, equation (A1.63) appears as:

$$\rho \bar{u}_j \frac{\partial \bar{u}_i}{\partial x_j} = \frac{\partial}{\partial x_j} (\bar{\tau}_{ij} + T_{ij}) \tag{A1.65}$$

where the expression $(\bar{\tau}_{ij} + T_{ij})$ is:

$$\bar{\tau}_{ij} + T_{ij} = -p\delta_{ij} + \mu\left(\frac{\partial \bar{u}_i}{\partial x_j} + \frac{\partial \bar{u}_j}{\partial x_i}\right) - \rho\overline{u_i' u_j'} \tag{A1.66}$$

Multiplying equation (A1.65) by $\bar{u}_i$:

$$\rho \bar{u}_j \frac{\partial(\frac{1}{2}\bar{u}_i \bar{u}_i)}{\partial x_j} = \frac{\partial}{\partial x_j} (\bar{\tau}_{ij} + T_{ij})\bar{u}_i + (\bar{\tau}_{ij} + T_{ij}) \frac{\partial \bar{u}_i}{\partial x_j} \tag{A1.67}$$

Define the mean rate of strain:

$$S_{ij} = \frac{1}{2}\left(\frac{\partial \bar{u}_i}{\partial x_j} + \frac{\partial \bar{u}_j}{\partial x_i}\right)$$

Using this expression in (A1.66) and then substituting (A1.66) in (A1.67), we arrive at the kinetic energy equation for the mean flow:

$$\bar{u}_j \frac{\partial(\frac{1}{2}\bar{u}_i\bar{u}_i)}{\partial x_j} = \frac{\partial}{\partial x_j}\left(-\frac{p}{\rho}\bar{u}_j + 2\nu\bar{u}_i S_{ij} - \overline{u_i'u_j'}\,\bar{u}_i\right)$$

$$+ 2\nu S_{ij}S_{ij} + \overline{u_i'u_j'}\,S_{ij} \qquad \text{(A1.68)}$$

Defining a fluctuating rate of strain:

$$s_{ij} = \frac{1}{2}\left(\frac{\partial u_i'}{\partial x_j} + \frac{\partial u_j'}{\partial x_i}\right)$$

Now substitute the mean rate of strain in equation (A1.13) for steady, incompressible flow to obtain:

$$u_j\frac{\partial u_i}{\partial x_j} = \frac{1}{\rho}\frac{\partial}{\partial x_j}\left(-p\delta_{ij} + 2\mu S_{ij}\right) \qquad \text{(A1.69)}$$

Multiplying (A1.69) by u_i :

$$u_j \frac{\partial(\frac{1}{2} u_i u_i)}{\partial x_j} = \frac{1}{\rho} \frac{\partial}{\partial x_j} (-p\, u_i \delta_{ij} + 2\mu u_i\ S_{ij})$$

$$+ \frac{1}{\rho} (-p\delta_{ij} + 2\mu S_{ij}) \frac{\partial u_i}{\partial x_j} \qquad \text{(A1.70)}$$

Taking the average of (A1.70):

$$u_j \frac{\partial}{\partial x_j} \left(\frac{1}{2} \overline{u_i' u_i'} + \frac{1}{2} \overline{u_i u_i} \right) = 2\nu (S_{ij} S_{ij} - \overline{s_{ij} s_{ij}})$$

$$- \frac{\partial}{\partial x_j} \left[\frac{1}{\rho} (u_j' p' + \overline{P}\overline{u}_j) + \frac{1}{2} (\overline{u_i' u_i' u_j'}) \right.$$

$$\left. - 2\nu (u_i S_{ij} + \overline{u_i' s_{ij}}) \right]$$

$$- \frac{\partial}{\partial x_j} (\overline{u_i' u_j' \overline{u}_i}) \qquad \text{(A1.71)}$$

Finally, subtracting the kinetic energy equation for mean flow (A1.68) from equation (A1.71):

$$\overline{u}_j \frac{\partial}{\partial x_j} \left(\frac{1}{2} \overline{u_i' u_i'} \right) + \frac{\partial}{\partial x_j} \left(\frac{1}{\rho} \overline{u_j' p'} + \frac{1}{2} \overline{u_i' u_i' u_j'} - 2\nu \overline{u_i' s_{ij}} \right)$$

$$= -2\nu \overline{s_{ij} s_{ij}} - \overline{u_i' u_j'}\, S_{ij} \qquad \text{(A1.72)}$$

Equation (A1.72) is known as the turbulent energy budget equation. This equation separates and defines the parameters affecting the turbulent energy. Beginning on the left of the equal sign we have:

$$\begin{Bmatrix}\text{Local rate of}\\ \text{change of}\\ \text{turbulent energy}\end{Bmatrix} + \begin{Bmatrix}\text{Turbulent}\\ \text{pressure}\\ \text{diffusion}\end{Bmatrix} + \begin{Bmatrix}\text{Turbulent}\\ \text{kinetic}\\ \text{diffusion}\end{Bmatrix} + \begin{Bmatrix}\text{Turbulent}\\ \text{viscous}\\ \text{diffusion}\end{Bmatrix}$$

$$= \begin{Bmatrix}\text{Turbulent}\\ \text{energy}\\ \text{dissiptation}\end{Bmatrix} - \begin{Bmatrix}\text{Turbulent}\\ \text{energy}\\ \text{production}\end{Bmatrix}$$

In a steady, homogeneous, pure shear flow, equation (A1.72) reduces to the expression:

$$2\nu\ \overline{s_{ij}s_{ij}} = -\overline{u_i'u_j'}\ S_{ij} \tag{A1.73}$$

or:

$$\epsilon = -\overline{u_i'u_j'}\ S_{ij} \tag{A1.74}$$

In summary, this section has introduced the atmospheric boundary layer equations necessary for analysis of flow in that regime. Based on the conditions of the model, certain equations will apply. For homogeneous, thin shear layers, Prandtl's analysis, equation (A1.52), proves to be adequate in predicting velocity profiles. This conclusion is arrived at from many observations (44) and especially some atmospheric conditions related to this experiment (43). For those conditions of atmospheric boundary layer flow involving high Reynolds numbers and a diverse range of eddies, as observed over irregular surfaces, the turbulent kinetic energy equation must be considered. Implicit in this equation is the spectral distribution of turbulent energy and its dominant effect on average velocity. This applies for flow from the ocean over the headland in this experiment.

Turbulence is nonlinear as indicated in equation (A1.72). To be more specific, the energy transfer from one size eddy to another can take place only in a nonlinear manner. In addition, turbulence is a stochastic or random process. The velocity field cannot be precisely defined. However, we do not need information on the details of flow, but we wish to predict the probability of flow characteristics. This directs us to the use of a statistical description.

The indication of the three dimensional effect of turbulence is by degree of correlation between two variables where we define:

Correlated when $\overline{u_i' u_j'} \neq 0$

Uncorrelated when $\overline{u_i' u_j'} = 0$

This degree of correlation is the "correlation coefficient", C_{ij}:

$$C_{ij} = \frac{\overline{u_i' u_j'}}{(\overline{u_i'^2}\ \overline{u_j'^2})^{1/2}} \qquad \text{(A1.75)}$$

The magnitude and sign of C_{ij} depend mainly on the mean value of $\overline{u_i' u_j'}$. The Reynolds stresses, $-\rho\overline{u_i' u_j'}$, will differ from zero if a correlation exists between corresponding pairs of eddy velocities at a point. Another valuable indication derived from the correlation coefficient when comparing wind speeds at different levels is that the smaller the eddies, the less the correlation (28).

In analyzing the energy in random functions, we resort to the frequency function called "power spectral density". This represents the distribution of power with respect to frequency. Defining the auto correlation coefficient $\rho(t)$ as:

$$\rho(t) = \frac{\overline{u'(t_1)u'(t_2)}}{\overline{u'^2}} \qquad \text{(A1.76)}$$

we can express the power spectral density, $\phi(\omega)$ as:

$$\phi(\omega) = \frac{1}{2\pi} \int_{-\infty}^{\infty} e^{-i\omega t} \rho(t)\overline{u^2} dt \qquad \text{(A1.77)}$$

The spectra is presented as $\ln \phi$ versus $\ln \omega$ since the frequency appears over several decades and the spectral values over the same range are useful. The method of obtaining the power spectral density will be discussed under Method of Testing. The value of the spectrum at a given frequency or wave length is the mean energy in that wave. Spectra presents information about the energy exchange between eddies (or waves) of different sizes. Turbulence receives its energy at large scales but the viscous dissipation of energy occurs at very small scales. There is a range of eddy sizes that are not directly affected by energy maintenance and dissipation known as the inertial subrange.

A. N. Kolmogorov proposed two similarity hypothesis in 1941 (16). The first is related to the conservation of energy with the condition that the mean level of turbulent energy is constant. Then the small eddies must convert into heat all the energy passed down to them by the break up of larger eddies. Kolmogorov's first similarity hypothesis states (47):

> The average properties of the small-scale components of any turbulent motion at high Reynolds number are determined uniquely by the kinematic viscosity of the fluid and the average rate of dissipation of energy per unit mass of fluid (ϵ). (Equation (A1.74).)

Dimensional arguments lead to the following universal spectral form:

$$\phi(K) = \epsilon^{1/4}\nu^{5/4}F(K/K_s) \tag{A1.78}$$

K_s = Kolmogorov wave number = $(\epsilon/\nu^3)^{1/4}$

K = wave number = $2\pi f/\bar{u} = \omega/\bar{u}$

ν = kinematic viscosity

$F(K/K_s)$ = Kolmogorov universal function

Kolmogorov's second fundamental hypothesis applies to conditions of very large Reynolds number. As the Reynolds number increases, the viscous dissipation will shift more toward the smaller eddies which are being created. In time, the largest eddies of the range covered by the first hypothesis will tend to become independent of the process of viscous dissipation by which the energy is passed to the molecules. Inertia forces will dominate. Kolmogorov's second similarity hypothesis states that (47):

> For sufficiently large Reynolds numbers, there is a subrange of the range of small eddies in which average properties are determined solely by the average rate of dissipation of energy per unit mass of the fluid (ϵ).

Dimensional arguments result in the following spectral form:

$$\phi(K) = \alpha\epsilon^{2/3}K^{-5/3} \tag{A1.79}$$

α = Kolmogorov universal constant

The best confirmation of the minus five-thirds law comes from the measurements of Pond et al. (39) who determined the spectra both in the inertial and dissipation subranges over water by hot-wire anemometry (Figure 1.2). The same law was confirmed in cumulus clouds by Steiner and Rhyn (46), in the ocean by Grant, Stewart and Moilliet (22) and in laboratory experiments by Gibson (19, 20). Accordingly, the Kolmogorov constant (α) of equation (A1.79) should be absolute, independent of the fluid or of the nature of the mean flow. Values of α range from 0.48 to 0.55 (54). Based on information from Williams (54), the value of $\alpha = 0.52$ was used.

Similarity conditions in model flows of turbulent boundary layer phenomena require application of Kolmogorov similarity hypothesis. The modifications to the wind tunnel to obtain this similarity will be explained under the Description of Test.

APPENDIX B

Velocity and Aximuth Data from the Test Tower at Yaquina Head

Anemometer Locations:

#1 at Z = 8 m above the pad

#2 at Z = 13 m above the pad

#3 at Z = 20 m above the pad

#4 at Z = 27.5 m above the pad

Velocity in cm/sec

Time in Pacific Daylight Time

Ambient conditions given in table

Anemometer location	1	2	3	4	5	6	7	8	9	10	11	12	13	14	15	16	17	18	19	20	21	22	23	24
Date, 20 July 75; Sky condition, Clear; Temp - ^{o}K (Time) Max (18) 290 Min (5) 285; Relative humidity % (Time) Max (5) 85 Min (18) 72																								
1	45	179	134	89	0	0	0	45	89	134	224	313	805	939	939	1162	1296	1162	1341	1386	1296	1252	1028	1073
	--	--	--	--	--	--	--	220	10	20	10	20	5	10	10	10	10	10	10	10	10	10	10	10
2	89	179	134	89	45	45	45	45	89	179	268	402	849	983	983	1252	1296	1207	1386	1430	1386	1341	1073	1073
	20	40	30	20	50	110	30	210	360	20	30	30	5	5	5	5	5	10	10	10	10	10	10	10
3	--	--	--	--	--	--	--	--	--	--	--	492	1028	1162	1162	1430	1475	1341	1475	1520	1475	1430	1162	1162
												20	20	20	20	20	360	10	10	5	5	10	10	10
4	134	268	224	134	89	0	0	89	134	179	313	492	849	1073	1073	1341	1341	1252	1430	1430	1386	1386	1162	1162
	360	10	360	360	30	210	360	210	330	350	360	360	340	340	340	340	340	350	350	350	350	350	350	350
Date, 21 July 75; Sky condition, Clear; Temp - ^{o}K (Time) Max (17) 290 Min (6) 285; Relative humidity % (Time) Max (20) 88 Min (16) 75																								
1	849	671	536	536	536	313	224	224	492	581	715	626	536	626	626	626	581	581	581	671	671	671	626	581
	10	10	10	10	10	20	10	20	10	10	10	10	10	10	10	10	10	10	10	10	10	10	10	10
2	894	715	626	626	581	313	268	224	536	671	805	626	626	671	671	715	581	626	671	715	715	760	671	671
	5	10	10	5	10	20	20	20	5	10	10	10	5	5	5	10	10	10	10	10	10	5	10	5
3	983	760	671	671	626	358	313	268	581	715	849	671	626	715	715	760	626	671	715	760	760	805	715	715
	10	10	10	5	10	10	10	10	360	10	360	360	360	360	360	5	5	5	5	10	5	5	10	10
4	939	715	581	581	581	358	313	268	581	626	805	671	581	671	671	671	581	581	671	715	671	760	671	715
	350	360	350	350	350	360	360	350	350	360	350	350	340	340	340	350	350	350	350	350	350	350	350	350

Date, 22 July 75; Sky condition, clear; Temp - ^{o}K (Time) Max (18) 288 Min (6) 284;
Relative humidity % (Time) Max (1) 87 Min (17) 74

Anemometer location	1	2	3	4	5	6	7	8	9	10	11	12	13	14	15	16	17	18	19	20	21	22	23	24
1	581	626	671	134	89	0	45	0	224	715	760	939	1162	1252	1475	1386	1252	1386	1386	1341	1252	671	134	179
	10	10	10	60	130	0	20	10	20	10	10	10	10	5	5	10	10	10	10	10	10	10	10	10
2	671	715	715	134	45	0	89	0	268	760	849	1028	1207	1296	1475	1386	1341	1430	1430	1341	1341	626	134	179
	5	5	10	60	150	340	50	360	30	5	10	5	360	360	5	10	10	10	5	5	5	10	10	10
3	715	760	715	224	89	0	179	89	402	849	983	1162	1341	1386	1565	1565	1475	1609	1565	1520	1475	894	224	268
	10	10	10	70	120	350	30	350	20	360	360	360	360	360	360	5	5	5	5	5	5	360	10	10
4	715	715	671	224	89	89	179	134	358	760	939	1118	1296	1386	1565	1520	1430	1520	1520	1430	1430	894	224	224
	350	350	350	60	120	320	20	330	10	350	350	350	340	340	350	350	350	350	350	350	350	350	360	360

Date, 23 July 75; Sky condition, Cloudy; Temp - ^{o}K (Time) Max (9) 289 Min (24) 285;
Relative humidity % (Time) Max (18) 89 Min (8) 79

Anemometer location	1	2	3	4	5	6	7	8	9	10	11	12	13	14	15	16	17	18	19	20	21	22	23	24
1	0	67	0	0	45	89	0	89	0	224	268	268	313	358	536	536	447	402	536	536	447	402	268	224
	0	20	50	220	180	40	130	10	280	40	30	20	20	10	20	10	20	10	10	10	10	10	20	20
2	0	89	0	0	45	134	0	89	0	224	224	268	313	358	623	623	492	402	626	581	447	402	268	224
	40	40	60	360	180	40	170	30	230	50	40	30	30	30	30	5	20	10	10	10	10	10	20	20
3	45	179	45	45	134	268	45	179	45	358	402	402	402	536	671	760	671	626	760	715	581	581	402	358
	10	30	30	70	150	50	50	40	160	50	40	30	30	20	20	360	10	360	10	10	10	10	10	360
4	45	179	89	89	134	179	0	134	0	268	358	358	358	447	581	715	581	492	671	581	447	402	313	224
	30	20	20	180	150	30	30	10	160	20	20	0	0	0	0	340	350	340	350	350	350	0	0	0

Anemometer location	1	2	3	4	5	6	7	8	9	10	11	12	13	14	15	16	17	18	19	20	21	22	23	24
Date, 24 July 75; Sky condition, Clear; Temp - °K (Time) Max 18) 288 Min (8) 284; Relative humidity % (Time) Max (3) 90 Min (12) 82																								
1	313	179	0	0	45	0	89	224	134	268	224	581	581	224	671	447	626	581	358	402	268	313	268	224
	20	10	180	220	30	180	10	10	10	10	20	10	10	10	10	20	10	10	20	10	10	20	20	10
2	313	179	0	0	89	0	134	179	134	268	224	581	626	224	715	447	715	671	402	402	224	313	268	224
	30	30	170	10	40	180	360	20	10	10	30	10	5	30	5	30	10	5	30	20	30	20	20	30
3	447	268	45	45	89	45	224	313	313	447	402	805	805	358	849	626	849	849	626	536	358	447	447	358
	30	40	110	200	50	200	330	30	10	360	20	5	10	20	360	20	360	360	20	10	30	20	20	10
4	358	224	45	45	89	89	224	268	224	358	358	715	715	313	715	581	760	760	536	402	313	358	313	268
	0	30	0	190	30	180	320	20	0	340	0	350	350	0	350	0	350	350	0	0	0	0	0	0
Date, 25 July 75; Sky condition, Cloudy AM, Clear PM; Temp - °K (Time) Max (19) 288 Min (9) 284; Relative humidity % (Time) Max (8) 91 Min (19) 72																								
1	224	224	402	313	671	715	402	626	179	492	715	1386	1520	1386	1520	1609	1700	1609	1565	1565	1430	1386	1252	1028
	10	10	20	20	10	10	10	10	20	10	10	10	10	10	10	10	10	10	10	10	10	10	10	10
2	268	268	402	492	805	760	402	671	224	536	760	1430	1520	1340	1565	1654	1740	1654	1610	1610	1475	1430	1340	1073
	20	30	30	20	10	10	30	10	40	10	360	5	5	10	10	5	5	5	5	10	5	10	10	10
3	358	447	626	626	894	983	581	894	313	939	1073	1610	1699	1520	1700	1788	1922	1788	1788	1788	1654	1610	1520	1207
	10	20	20	20	5	10	10	360	40	360	350	360	360	360	360	360	360	360	360	360	360	360	360	5
4	313	358	581	581	805	939	536	805	313	894	1073	1565	1654	1475	1700	1743	1833	1788	1788	1743	1654	1565	1430	1207
	0	0	0	0	350	350	0	340	20	350	340	340	0	0	0	0	0	0	0	0	0	350	350	350

Anemometer location	1	2	3	4	5	6	7	8	9	10	11	12	13	14	15	16	17	18	19	20	21	22	23	24
Date, 26 July 75; Sky condition, Clear; Temp - °K (Time) Max (15) 285 Min (7) 284; Relative humidity % (Time) Nax (21) 90 Min (14) 80																								
1	1028	1162	760	805	134	134	224	45	313	313	626	1073	1028	1252	1475	1118	1162	1207	1296	1207	1073	894	983	1073
	10	10	10	10	20	5	5	10	10	20	10	10	10	5	5	10	20	10	10	10	10	10	10	10
2	1162	1162	805	849	179	179	268	89	402	313	715	1162	1162	1341	1520	1252	1207	1207	1296	1296	1118	983	1028	1162
	10	10	10	10	30	10	10	10	20	30	20	5	5	360	5	10	10	10	10	10	10	10	5	5
3	1341	1475	1073	1028	268	268	313	179	536	447	849	1386	1296	1520	1610	1386	1296	1341	1386	1430	1207	1118	1162	1340
	360	360	360	10	20	10	360	360	20	30	20	350	350	350	350	360	5	5	5	5	5	5	5	5
4	1252	1386	983	939	179	134	224	179	358	402	805	1341	1296	1475	1609	1386	1207	1341	1341	1341	1162	1073	1162	1207
	350	350	0	0	0	0	0	0	0	0	350	330	340	340	340	0	0	0	0	0	0	0	0	0
Date, 27 July 75; Sky condition, Cloudy AM, Clear PM; Temp - °K (Time) Max (15) 286 Min (5) 284; Relative humidity % (Time) Max (6) 90 Min (14) 85																								
1	1160	894	1028	1162	939	939	805	626	626	581	671	849	447	336	581	805	671	805	760	760	760	760	671	671
	10	10	10	10	10	10	10	10	10	10	10	10	20	20	10	5	10	10	10	10	10	10	10	10
2	1207	1028	1073	1162	1028	983	894	715	760	671	715	894	536	358	611	849	760	894	805	805	849	849	805	805
	5	5	5	10	5	5	5	10	20	10	5	5	10	20	5	360	10	10	10	10	10	10	20	10
3	1341	1162	1207	1386	1162	1162	1073	939	939	894	894	1073	760	581	805	1073	894	1073	983	939	1073	1028	939	1028
	5	360	5	5	360	360	360	10	10	360	360	360	350	360	360	350	360	360	5	5	360	5	10	5
4	1386	1118	1207	1296	1118	1118	1028	894	805	760	760	1028	715	447	715	1028	805	1028	894	939	1028	1028	894	1028
	360	360	360	360	350	350	350	0	0	350	350	340	340	340	340	340	350	0	0	0	0	0	0	0

Anemometer location	1	2	3	4	5	6	7	8	9	10	11	12	13	14	15	16	17	18	19	20	21	22	23	24
Date, 28 July 75; Sky condition, Cloudy - Rain; Temp - °K (Time) Max (7) 286 Min (18) 283; Relative humidity % (Time) Max (13) 91 Min (19) 78																								
1	224	313	45	89	89	0	179	849	805	1073	1162	1252	1430	1252	1296	1162	626	671	671	402	313	179	0	0
	20	20	20	30	20	10	20	10	10	10	10	10	10	10	10	10	10	10	10	10	20	10	10	190
2	268	268	134	134	89	0	224	894	849	1118	1162	1341	1430	1296	1341	1252	715	671	760	536	313	179	45	0
	20	30	30	40	30	10	20	5	5	5	5	10	10	5	10	10	10	5	5	10	30	30	10	10
3	447	447	224	179	134	0	313	1073	1028	1252	1296	1386	1654	1430	1430	1341	849	939	894	626	447	224	134	0
	20	30	20	30	30	30	20	360	5	5	360	10	5	5	10	10	360	360	360	30	30	30	30	20
4	402	402	224	224	179	89	313	1073	983	1162	1207	1296	1475	1341	1341	1207	671	805	760	671	402	224	134	0
	0	20	360	20	20	360	360	360	360	360	350	360	350	360	360	360	360	350	350	340	360	360	360	330
Date, 29 July 75; Sky condition, Cloudy; Temp - °K (Time) Max (16) 289 Min (4) 282; Relative humidity % (Time) Max (3) 88 Min (16) 72																								
1	0	179	45	89	179	179	45	89	134	179	134	179	224	224	268	224	134	224	0	0	179	134	268	224
	130	130	180	180	170	140	180	140	170	180	190	180	180	180	180	180	180	10	20	170	180	160	160	160
2	0	224	89	89	179	224	89	89	134	134	134	179	179	179	268	224	179	224	0	0	179	134	268	268
	180	180	180	180	180	160	180	160	170	180	200	180	180	180	190	180	210	10	50	210	180	160	170	170
3	0	268	179	179	268	268	224	224	268	268	224	268	313	268	358	358	268	402	0	0	224	268	402	358
	160	160	150	150	160	140	150	140	160	170	200	180	180	180	190	180	200	10	60	230	190	160	160	160
4	0	224	134	134	268	268	224	179	224	224	224	268	268	268	358	268	179	358	89	89	224	224	268	313
	180	170	160	170	170	150	170	160	170	180	190	180	180	180	180	180	190	350	350	180	180	170	170	180

Anemometer location	1	2	3	4	5	6	7	8	9	10	11	12	13	14	15	16	17	18	19	20	21	22	23	24

Date, 30 July 75; Sky condition, Cloudy AM, Clear PM; Temp - ^{o}K (Time) Max (15) 290 Min (6) 284;
Relative humditiy % (Time) Max (3) 89 Min (18) 73

1	224	224	89	268	179	224	179	179	268	179	89	0	45	0	89	89	268	179	224	313	224	89	89	0
	170	130	150	170	180	160	160	180	170	180	180	220	220	10	20	10	10	10	10	10	20	30	30	180
2	224	224	89	268	179	224	224	224	313	224	45	0	0	0	45	89	268	179	224	313	224	89	89	0
	180	130	160	170	190	170	180	190	180	190	190	240	240	10	20	20	5	10	20	10	30	30	30	30
3	313	268	268	402	313	358	313	313	447	268	89	45	45	0	45	179	358	313	358	447	358	268	224	0
	180	150	160	170	140	160	170	180	170	200	170	230	230	340	20	10	360	360	20	360	20	20	20	20
4	268	224	224	268	268	313	224	268	402	268	89	89	89	89	134	134	313	268	313	358	358	268	268	0
	180	140	180	180	180	180	180	180	150	190	190	240	240	330	350	340	350	350	0	350	0	0	0	20

Date, 31 July 75; Sky condition, Clear; Temp - ^{o}K (Time) Max (18) 287 Min (6) 283;
Relative humidity % (Time) Max (22) 90 Min (3) 75

1	0	0	0	0	0	0	0	89	134	224	671	760	805	760	849	1073	1028	1341	1207	1296	1341	1252	1207	1296
	20	180	180	160	180	60	360	10	20	20	360	10	10	10	10	10	10	10	10	10	10	10	10	10
2	0	0	0	0	0	0	0	45	89	134	760	805	849	805	849	1162	1073	1341	1252	1341	1430	1341	1207	1341
	30	130	280	280	180	90	360	360	40	30	360	5	5	5	5	5	5	10	10	10	10	10	10	10
3	0	0	0	0	0	0	45	179	224	313	894	983	1073	983	1073	1296	1207	1475	1430	1475	1520	1430	1386	1520
	20	20	20	20	20	20	20	360	30	20	350	360	360	360	360	360	10	10	10	10	10	10	10	10
4	134	0	0	0	0	0	134	179	179	268	894	983	1028	939	1028	1296	1118	1430	1430	1386	1430	1341	1341	1430
	360	330	300	0	300	350	10	330	350	360	340	340	340	350	350	350	350	350	360	350	360	360	360	350

Date, 1 Aug 75; Sky condition, Cloudy AM, Clear PM; Temp - °K (Time) Max (18) 285 Min (7) 283;
Relative humidity % (Time) Max (24) 92 Min (18) 79

Anemometer location	1	2	3	4	5	6	7	8	9	10	11	12	13	14	15	16	17	18	19	20	21	22	23	24
1	1207	492	983	492	581	715	849	805	760	894	1073	1252	1252	1430	1341	1386	1341	1475	1386	1296	1207	1252	1252	1162
	10	10	10	10	10	10	10	20	10	5	5	10	10	10	10	10	10	5	10	10	10	5	10	10
2	1252	536	1028	536	715	760	894	894	849	983	1162	1252	1296	1475	1386	1430	1430	1520	1475	1341	1252	1296	1296	1207
	10	20	10	10	10	5	5	10	5	5	360	5	5	5	5	5	5	5	5	5	10	10	10	10
3	1341	671	1162	715	760	894	983	983	939	1073	1252	1430	1430	1565	1565	1520	1520	1654	1565	1520	1430	1430	1386	1386
	10	10	360	360	360	360	360	10	360	360	360	360	360	360	360	10	10	360	10	10	10	10	10	360
4	1296	671	1073	626	715	760	939	939	894	1073	1252	1430	1430	1565	1475	1430	1430	1565	1475	1430	1341	1341	1296	1341
	350	10	360	360	360	350	350	360	350	350	350	350	350	350	350	350	350	350	350	350	350	350	350	350

Date, 2 Aug 75; Sky condition, Cloudy AM, Clear PM; Temp - °K (Time) Max (17) 286 Min (5) 283;
Relative humidity % (Time) Max (4) 91 Min (18) 79

Anemometer location	1	2	3	4	5	6	7	8	9	10	11	12	13	14	15	16	17	18	19	20	21	22	23	24
1	1207	1073	894	626	715	671	760	715	849	1073	1028	1118	1073	760	715	715	849	939	894	894	805	805	536	447
	10	10	10	10	10	10	10	10	10	10	5	5	10	10	10	10	10	10	10	10	10	10	10	20
2	1296	1162	983	671	760	715	849	805	894	1162	1073	1207	1162	894	760	805	939	1118	939	983	894	894	671	536
	10	10	10	10	10	5	10	10	5	5	360	5	10	5	10	10	10	10	10	10	5	5	10	20
3	1386	1341	1073	849	805	849	983	939	1073	1386	1252	1296	1296	1028	939	1028	1118	1252	1073	1162	1073	1118	760	715
	10	360	10	10	10	360	360	360	360	360	360	360	360	360	360	360	360	360	360	360	360	360	10	10
4	1296	1296	983	760	715	760	939	939	983	1252	1207	1296	1296	1028	894	1028	1073	1118	1073	1073	1028	1073	671	715
	350	350	360	350	360	350	350	350	350	340	340	350	350	350	350	350	350	350	350	350	350	350	350	350

Anemometer location	1	2	3	4	5	6	7	8	9	10	11	12	13	14	15	16	17	18	19	20	21	22	23	24

Date, 3 Aug 75; Sky condition, Clear; Temp - °K (Time) Max (18) 286 Min (6) 283;
Relative humidity % (Time) Max (5) 91 Min (17) 79

Anemometer location	1	2	3	4	5	6	7	8	9	10	11	12	13	14	15	16	17	18	19	20	21	22	23	24
1	536	671	224	45	179	45	0	45	179	268	358	671	849	1028	1341	1341	1341	1386	1296	1207	1073	939	849	402
	20	10	20	20	140	40	220	30	30	20	20	20	10	10	5	5	5	5	360	10	10	10	10	10
2	581	849	268	48	179	0	0	45	179	268	358	760	894	1207	1430	1430	1386	1475	1430	1341	1252	1118	983	536
	20	10	30	50	160	40	40	40	40	30	30	20	10	360	5	5	5	5	360	5	5	5	360	10
3	715	894	358	134	268	0	45	89	268	358	447	894	1073	1296	1565	1520	1520	1609	1520	1520	1386	1207	1162	581
	20	10	20	30	150	170	40	30	40	30	20	30	360	350	350	360	360	360	360	360	360	360	360	20
4	671	894	358	134	179	0	89	89	224	358	402	715	1073	1296	1520	1475	1475	1565	1430	1430	1296	1162	1118	492
	360	350	0	20	170	10	20	360	20	20	360	360	340	330	330	340	350	340	350	350	350	350	350	360

Date, 4 Aug 75; Sky condition, Cloudy; Temp - °K (Time) Max (14) 289 Min (4) 283;
Relative humidity % (Time) Max (4) 90 Min (18) 75

Anemometer location	1	2	3	4	5	6	7	8	9	10	11	12	13	14	15	16	17	18	19	20	21	22	23	24
1	0	268	0	358	89	179	0	89	0	45	45	179	89	134	200	313	313	358	358	179	179	268	313	358
	10	20	0	10	20	20	10	30	10	10	10	20	20	30	10	10	10	20	20	20	20	20	20	10
2	45	358	89	358	89	224	0	134	0	45	0	179	45	134	224	447	447	402	447	179	268	313	313	492
	350	20	360	20	30	30	10	60	180	20	10	20	360	40	10	350	360	10	30	30	20	30	30	10
3	134	447	179	536	268	358	0	179	45	134	45	358	224	313	358	626	626	626	581	224	358	358	536	671
	330	360	350	10	30	20	30	50	50	350	360	10	340	20	340	340	350	350	20	360	10	20	20	350
4	179	402	179	402	268	358	89	179	134	179	134	313	224	268	358	447	581	581	492	224	268	268	402	581
	330	350	350	360	10	360	300	20	360	350	360	360	310	350	330	330	360	330	360	330	350	360	360	340

Date, 5 Aug 75; Sky condition, Broken clouds; Temp - °K (Time) Max (13) 298 Min (6) 284;
Relative humidity % (Time) Max (0) 88 Min (13) 70

Anemometer location	1	2	3	4	5	6	7	8	9	10	11	12	13	14	15	16	17	18	19	20	21	22	23	24
1	179	224	224	224	45	0	0	45	224	447	671	447	894	983	983	894	805	1073	1118	1118	1162	1162	1118	1073
	10	20	20	20	20	40	220	10	20	20	5	30	10	10	10	10	20	10	10	20	10	10	10	10
2	179	224	313	224	89	0	0	89	224	492	849	313	983	1073	983	939	894	1162	1162	1207	1296	1296	1207	1207
	30	40	30	30	20	300	160	340	30	20	360	30	360	5	5	10	12	10	10	10	10	10	10	10
3	268	447	358	358	224	0	0	224	402	626	983	447	1118	1252	1162	1028	1028	1252	1341	1341	1341	1386	1341	1296
	10	30	20	20	20	320	320	330	20	10	350	10	360	360	360	10	10	350	350	350	350	360	350	360
4	224	402	313	313	179	89	0	224	358	402	939	402	1073	1162	1073	1028	983	1207	1296	1296	1296	1341	1296	1207
	360	10	360	360	350	350	350	330	360	340	330	360	350	350	350	360	360	360	360	360	360	360	360	360

Date, 6 Aug 75; Sky condition, Clear; Temp - °K (Time) Max (16) 286 Min (5) 283;
Relative humidity % (Time) Max (24) 87 Min (7) 77

Anemometer location	1	2	3	4	5	6	7	8	9	10	11	12	13	14	15	16	17	18	19	20	21	22	23	24
1	1028	1028	760	358	179	45	268	268	760	805	894	983	1073	1028	805	626	849	358	45	89	0	224	224	313
	10	10	10	20	10	10	10	20	10	10	10	10	10	10	10	10	10	10	30	270	170	180	170	170
2	1118	1073	805	402	179	89	313	224	805	894	1028	1118	1118	1118	849	671	894	402	45	89	0	224	224	358
	10	10	10	20	10	30	10	30	10	5	360	10	5	5	5	10	10	350	30	300	200	190	180	180
3	1252	1252	983	536	224	224	402	268	983	1073	1118	1207	1296	1252	983	849	1028	536	45	224	0	358	358	447
	360	360	360	20	10	30	360	20	360	360	360	360	360	360	350	360	360	340	350	280	200	190	180	170
4	1118	1162	894	492	224	268	313	268	939	983	1118	1118	1207	1162	939	805	983	536	89	224	0	268	268	402
	360	350	350	360	360	20	350	360	350	350	340	350	350	350	340	350	350	330	350	270	170	180	170	170

Anemometer location	1	2	3	4	5	6	7	8	9	10	11	12	13	14	15	16	17	18	19	20	21	22	23	24
Date, 7 Aug 75; Sky condition, Cloudy; Temp - °K (Time) Max (12) 288 Min (4) 284; Relative humidity % (Time) Max (23) 89 Min (10)70																								
1	313	358	402	402	358	313	358	402	492	626	671	581	581	581	671	536	492	581	447	581	492	536	536	313
	150	160	170	170	180	160	160	170	180	180	180	180	180	180	180	180	180	180	180	180	180	180	190	190
2	313	402	402	447	268	313	402	447	536	671	805	671	671	715	805	626	626	671	581	671	536	671	626	402
	160	170	180	170	190	160	170	180	180	190	180	180	180	180	180	180	180	190	190	180	190	180	180	190
3	447	447	581	626	536	447	536	626	715	805	939	760	715	805	894	671	671	805	626	805	715	715	715	536
	150	160	170	170	180	160	160	180	170	180	180	180	180	170	180	180	180	180	180	170	180	180	180	180
4	402	402	447	581	447	447	447	581	715	805	983	715	715	715	849	671	581	849	626	715	715	671	671	447
	160	160	180	170	180	160	170	170	180	180	180	180	180	180	180	180	180	180	180	170	180	180	180	180
Date, 8 Aug 75; Sky condition, Clear; Temp - °K (Time) Max (16) 286 Min (5) 284; Relative humidity % (Time) Max (8) 88 Min (22) 74																								
1	45	179	224	0	45	0	0	0	56	179	536	626	671	671	715	715	894	939	849	894	894	939	581	0
	200	40	30	200	220	45	10	220	40	30	10	10	10	10	10	20	20	20	20	20	20	20	30	200
2	45	224	268	0	45	0	0	0	89	224	626	760	805	760	805	805	983	1028	939	983	983	1028	626	0
	200	30	40	210	200	60	150	150	40	30	5	5	5	5	5	10	10	10	10	10	10	10	20	10
3	179	313	313	0	134	0	0	0	224	402	715	849	939	894	983	983	1073	1162	1073	1118	1073	1073	715	0
	200	30	30	30	200	10	30	30	20	350	355	360	355	355	360	5	5	5	5	5	5	5	10	5
4	134	358	358	0	134	0	0	0	224	402	626	760	894	805	983	983	1028	1118	1028	1073	1028	1073	626	0
	190	0	10	30	200	340	210	0	350	350	340	350	340	340	350	350	350	350	350	0	350	350	0	330

Anemometer location	1	2	3	4	5	6	7	8	9	10	11	12	13	14	15	16	17	18	19	20	21	22	23	24
Date, 9 Aug 75; Sky condition, Clear; Temp - °K (Time) Max (16) 286 Min (6) 282; Relative humidity % (Time) Max (23) 89 Min (0) 72																								
1	0	0	0	0	0	0	45	0	358	894	1073	1028	849	805	849	849	894	1028	939	849	894	760	760	313
	5	250	10	10	220	70	20	10	10	10	10	10	20	20	20	20	30	20	20	20	10	10	10	30
2	0	0	0	0	0	0	89	0	358	939	1162	1162	894	894	939	939	939	1073	983	894	983	849	849	358
	320	30	10	350	10	60	30	10	20	5	5	5	10	10	10	10	10	5	10	10	5	5	0	20
3	0	0	45	0	0	0	268	0	447	1118	1296	1252	1028	1028	1028	1028	1073	1252	1162	1028	1162	1028	983	581
	5	5	20	10	10	15	10	10	10	5	5	360	5	5	5	5	5	360	5	5	5	360	355	5
4	0	0	89	89	0	89	268	89	358	1118	1296	1252	1028	983	1028	1028	1028	1207	1118	1028	1118	983	939	581
	300	0	0	330	270	10	0	330	10	340	340	350	350	350	350	350	350	350	350	350	350	350	350	350
Date, 10 Aug 75; Sky condition, Clear; Temp - °K (Time) Max (10) 287 Min (4) 283; Relative humidity % (Time) Max (2) 89 Min (8) 78																								
1	358	313	358	224	894	849	358	45	0	89	447	760	805	1118	939	1118	1296	1386	1341	1386	1386	1341	1386	1207
	30	30	30	30	20	20	30	210	220	20	20	20	20	20	20	20	20	20	20	20	20	20	20	20
2	358	358	402	225	939	894	402	0	0	134	447	894	939	1118	1028	1162	1341	1520	1386	1475	1430	1386	1430	1386
	30	30	10	30	10	10	40	1i0	210	0	0	5	10	10	10	10	10	10	10	10	10	10	10	10
3	536	536	581	313	1073	983	536	0	0	268	760	983	1028	1252	1118	1252	1430	1609	1520	1520	1609	1565	1565	1475
	350	5	5	20	360	10	30	150	150	350	340	360	5	5	5	5	5	5	5	5	5	5	5	5
4	626	536	581	313	1073	1028	581	0	0	313	760	894	1028	1207	1118	1252	1430	1520	1430	1520	1565	1475	1520	1386
	350	350	350	0	0	0	10	190	220	330	330	350	350	0	0	0	0	0	0	0	0	0	0	0

Anemometer location	1	2	3	4	5	6	7	8	9	10	11	12	13	14	15	16	17	18	19	20	21	22	23	24
Date, 11 Aug 75; Sky condition, Clear; Temp - ^{o}K (Time) Max (15) 285 Min (4) 283; Relative humidity % (Time) Max (24) 88 Min (8) 78																								
1	1118	1252	1252	1118	447	805	1073	581	626	894	1296	1073	1296	1386	1207	1162	1073	1386	1743	1654	1743	1475	1430	1430
	10	10	10	10	20	20	20	10	10	0	0	0	0	0	0	0	0	5	10	5	0	0	0	0
2	1252	1252	1296	1162	715	849	1118	715	760	983	1296	1207	1341	1430	1296	1207	1252	1430	1788	1699	1788	1520	1520	1475
	10	10	10	10	10	10	10	5	5	360	5	10	5	10	5	10	20	10	10	10	10	10	10	10
3	1341	1386	1430	1341	1296	939	1207	805	894	1073	1475	1341	1520	1565	1341	1296	1341	1520	1967	1877	1877	1609	1609	1565
	5	5	5	5	5	10	5	360	355	355	355	355	360	360	360	5	10	5	5	5	5	5	10	5
4	1296	1341	1341	1252	805	805	1118	805	894	1118	1430	1341	1430	1565	1296	1296	1296	1520	1877	1833	1877	1609	1609	1565
	360	360	360	350	360	360	350	350	350	340	350	350	350	350	350	350	350	350	350	350	350	0	0	0
Date, 12 Aug 75; Sky condition, Cloudy; Temp - ^{o}K (Time) Max (13) 285 Min (6) 283; Relative humidity % (Time) Max (10) 91 Min (13) 88																								
1	1296	1252	1207	939	894	849	715	492	447	492	805	1073	849	760	1028	939	894	849	894	849	849	1028	894	849
	0	0	0	10	0	0	0	10	0	0	0	0	0	0	0	0	5	0	0	10	5	0	5	5
2	1341	1341	1296	1118	1118	983	894	626	626	581	1028	1162	1028	983	1162	1028	1073	1028	1073	1028	894	1162	1028	894
	10	10	10	10	10	10	10	10	0	10	10	10	10	10	10	10	10	5	10	20	10	0	10	10
3	1386	1386	1386	1207	1162	1073	939	671	671	760	1118	1252	1073	1073	1252	1162	1162	1118	1162	1118	1073	1207	1073	1162
	5	5	5	5	5	5	350	5	350	355	360	360	5	10	360	360	360	360	350	10	360	350	0	0
4	1386	1430	1341	1162	1118	1073	939	581	626	760	1118	1252	1073	1073	1252	1118	1118	1073	1073	1028	1028	1162	1073	1118
	0	350	350	350	350	0	0	0	340	355	350	350	350	0	350	350	350	350	350	0	350	350	350	350

Anemometer location	1	2	3	4	5	6	7	8	9	10	11	12	13	14	15	16	17	18	19	20	21	22	23	24
Date, 13 Aug 75; Sky condition, Cloudy; Temp - ^{o}K (Time) Max (15) 286 Min (5) 283; Relative humidity % (Time) Max (6) 91 Min (15) 81																								
1	0	89	0	358	268	402	313	134	492	402	402	179	581	402	313	402	402	358	402	358	224	179	156	179
	10	10	10	5	10	20	20	20	10	5	5	10	0	0	10	10	10	10	10	10	20	10	40	20
2	0	89	0	492	402	492	492	134	715	626	536	268	715	536	492	581	626	581	536	536	313	224	224	358
	30	10	250	10	30	30	30	30	20	10	10	20	10	0	10	5	10	20	10	10	20	40	30	20
3	45	111	0	536	447	626	536	268	805	715	715	536	849	626	626	671	715	715	715	626	536	313	268	425
	10	350	350	0	20	20	20	20	10	0	0	340	0	0	0	0	0	10	0	10	0	0	10	10
4	134	179	134	402	402	581	581	313	760	671	671	715	805	581	581	671	671	626	715	626	536	313	358	402
	0	350	30	360	10	10	10	10	0	350	0	330	350	350	350	350	0	0	350	350	350	350	5	0
Date, 14 Aug 75; Sky condition, Cloudy, Temp - ^{o}K (Time) Max (13) 289 Min (3) 284; Relative humidity % (Time) Max (3) 90 Min (13) 72																								
1	179	156	89	134	89	89	89	179	134	179	134	89	89	89	268	179	134	89	134	89	45	0	45	0
	20	20	20	20	30	20	30	30	20	20	20	10	10	20	10	20	20	20	20	20	30	30	20	10
2	224	179	134	224	89	134	67	313	89	268	224	89	89	45	313	224	89	134	224	112	67	45	0	45
	30	30	40	30	30	30	30	30	40	20	10	30	30	30	20	30	20	30	20	30	30	30	30	30
3	358	358	268	313	200	268	156	425	200	358	358	200	200	156	425	358	425	200	268	200	112	46	156	46
	10	10	20	10	10	20	20	20	20	10	10	30	30	30	350	10	10	10	10	20	30	30	30	20
4	402	358	313	358	268	268	224	447	268	313	358	224	224	224	402	358	402	268	268	224	134	134	224	134
	5	5	350	350	10	0	0	20	5	0	0	0	350	30	350	340	330	10	0	10	20	350	0	10

APPENDIX C

Velocity and Azimuth Frequency Distribution at the Yaquina Head Lighthouse Anemometer Station 1973-1975

Data from Atmospheric Sciences Department,

Oregon State University

WIND SPEED FREQUENCY DISTRIBUTIONS RUN 06/22/76 FOR YAQUINA LIGHTHOUSE

SPEED CATEGORIES (MPS)

PERIOD	CALM TO 2	2 TO 4	4 TO 6	6 TO 8	8 TO 10	10 TO 12	12 TO 14	14 TO 16	16 TO 18	18 TO 20	20 TO 22	22 TO 24	24 TO 26	26 TO 28	28 TO 30	≥ 30	TOTAL OBS	SPEED MEAN	SPEED SD
1973	1235	944	872	604	521	433	283	145	57	19	18	1	0	0	0	0	5192	5.6	4.4
1974	1627	1255	1017	735	624	427	346	171	93	38	27	4	2	1	1	1	6369	5.5	4.5
1975	653	656	764	520	511	281	215	83	52	14	13	7	3	1	2	0	3785	6.1	4.2
JAN	230	274	258	177	162	123	74	63	41	9	16	5	2	1	1	0	1436	6.7	4.9
FEB	247	245	379	249	178	157	90	39	25	5	6	1	3	1	2	0	1628	6.4	4.3
MAR	210	179	[illegible]	164	173	116	63	27	29	10	13	2	0	0	0	0	1191	6.6	4.6
APR	411	334	327	271	240	110	94	10	5	2	0	0	0	0	0	0	1804	5.3	3.7
MAY	559	416	342	228	199	106	91	39	22	6	2	3	0	0	0	0	2113	4.8	4.1
JUN	217	282	304	205	178	124	107	36	14	1	0	0	0	0	0	0	1458	6.2	3.9
JUL	564	362	234	164	180	107	98	76	17	6	6	0	0	0	0	0	1814	5.2	4.5
AUG	280	188	130	93	123	118	107	37	0	0	0	0	0	0	0	0	1076	6.0	4.5
SEP	256	141	104	69	40	32	22	6	1	0	0	0	0	0	0	0	671	3.9	3.6
OCT	238	199	124	65	47	26	19	1	2	0	0	0	0	0	0	0	711	3.9	3.3
NOV	185	129	92	69	52	42	35	27	23	15	6	0	0	0	0	1	676	6.0	5.3
DEC	88	116	154	105	84	80	54	38	22	17	9	1	0	0	0	0	768	7.5	4.9
TOTAL	3535	2855	2653	1859	1656	1141	844	399	202	71	58	12	5	2	3	1	15346	5.7	4.4

DISTRIBUTIONS IN PERCENT

SPEED CATEGORIES (MPS)

PERIOD	CALM TO 2	2 TO 4	4 TO 6	6 TO 8	8 TO 10	10 TO 12	12 TO 14	14 TO 16	16 TO 18	18 TO 20	20 TO 22	22 TO 24	24 TO 26	26 TO 28	28 TO 30	≥ 30	TOTAL OBS
1973	24.9	18.2	16.8	11.6	10.0	8.3	5.5	2.8	1.1	.4	.3	.0	0	0	0	0	5192
1974	25.5	19.7	16.0	11.5	9.8	6.7	5.4	2.7	1.5	.6	.4	.1	.0	.0	.0	.0	6369
1975	17.5	17.3	20.2	13.7	13.5	7.4	5.7	2.2	1.4	.4	.3	.2	.1	.0	.1	0	3785
JAN	16.0	19.1	18.0	12.3	11.3	8.6	5.2	4.4	2.9	.6	1.1	.3	.1	.1	.1	0	1436
FEB	15.2	15.0	23.3	15.3	10.9	9.6	5.5	2.4	1.6	.3	.4	.1	.2	.1	.1	0	1628
MAR	17.6	[illegible]	17.2	13.8	14.5	9.7	5.3	2.3	2.4	.8	1.1	.2	0	0	0	0	1191
APR	22.8	18.5	18.1	15.0	13.3	6.1	5.2	.6	.3	.1	0	0	0	0	0	0	1804
MAY	31.7	19.7	16.2	12.8	9.4	5.0	3.8	1.8	1.0	.3	.1	.1	0	0	0	0	2113
JUN	14.2	19.3	23.9	14.1	12.2	8.5	7.3	2.5	1.0	.1	0	0	0	0	0	0	1458
JUL	31.1	[illegible]	12.9	9.0	9.9	5.9	5.4	4.2	.9	.3	.3	0	0	0	0	0	1814
AUG	26.0	17.5	12.1	8.6	11.4	11.0	9.9	3.4	0	0	0	0	0	0	0	0	1076
SEP	38.2	[illegible]	15.5	10.3	6.0	4.8	3.3	.9	.1	0	0	0	0	0	0	0	671
OCT	33.5	26.5	17.4	9.1	5.6	3.7	2.7	.1	.3	0	0	0	0	0	0	0	711
NOV	27.4	19.1	13.6	10.2	7.7	5.2	5.2	4.0	3.4	2.2	.9	0	0	0	0	.1	676
DEC	11.5	15.1	20.1	13.7	10.9	10.4	7.0	4.9	2.9	2.2	1.2	.1	0	0	0	0	768
TOTAL	23.4	18.6	17.3	12.1	10.9	7.4	5.5	2.6	1.3	.5	.4	.1	.0	.0	.0	.0	15346

WIND DIRECTION FREQUENCY DISTRIBUTIONS RUN 06/22/76 FOR YAQUINA LIGHTHOUSE

DIRECTION CATEGORIES

PERIOD	N	NNE	NE	ENE	E	ESE	SE	SSE	S	SSW	SW	WSW	W	WNW	NW	NNW	CALM	TOTAL OBS
1973	1386	177	22	42	343	288	340	596	582	135	56	107	139	137	100	257	216	4917
1974	1493	351	57	124	242	275	427	621	952	128	93	192	196	141	123	279	323	5997
1975	373	82	24	51	232	302	321	253	357	120	62	124	167	197	481	505	94	3745
JAN	59	40	21	58	195	170	85	214	264	23	17	41	79	41	27	38	23	1395
FEB	127	46	11	18	275	231	145	178	223	43	22	64	52	35	56	57	17	1601
MAR	146	[illegible]	9	19	66	62	68	101	154	69	14	53	69	43	44	77	10	1054
APR	523	94	18	18	47	38	94	102	191	75	35	51	81	65	77	158	81	1748
MAY	343	28	7	18	25	65	89	122	220	60	52	86	101	126	167	235	101	1847
JUN	332	24	6	5	20	39	140	163	141	34	23	38	49	49	147	188	51	1449
JUL	532	48	1	2	15	42	143	136	190	10	9	15	20	50	125	154	143	1738
AUG	507	53	9	3	9	23	81	88	54	9	3	3	8	3	12	61	41	1067
SEP	239	82	9	15	15	12	24	89	71	3	5	2	2	1	3	28	68	660
OCT	174	118	7	21	24	22	55	91	75	4	2	8	6	0	4	18	63	692
NOV	46	16	5	8	50	65	73	104	151	16	7	16	16	18	16	14	34	656
DEC	18	11	2	12	72	94	91	91	157	37	21	46	19	43	26	13	1	752
TOTAL	3246	610	103	197	817	865	1086	1470	1891	383	211	423	502	475	704	1041	633	14659

DISTRIBUTIONS IN PERCENT

DIRECTION CATEGORIES

PERIOD	N	NNE	NE	ENE	E	ESE	SE	SSE	S	SSW	SW	WSW	W	WNW	NW	NNW	CALM	TOTAL OBS
1973	28.1	3.6	.4	.9	7.0	5.9	6.9	12.1	11.8	2.7	1.1	2.2	2.8	2.8	2.0	5.2	4.4	4917
1974	24.9	5.9	1.0	1.7	4.0	4.6	7.1	10.4	15.9	2.1	1.6	3.2	3.3	2.4	2.1	4.7	5.4	5997
1975	10.0	2.2	.6	1.4	6.2	8.1	8.6	6.8	9.5	3.2	1.7	3.3	4.5	5.3	12.8	13.5	2.5	3745
JAN	4.2	2.9	1.5	4.2	14.0	12.2	6.1	15.3	18.9	1.6	1.2	2.9	5.7	2.9	1.9	2.7	1.6	1395
FEB	7.9	2.9	.7	1.1	17.2	14.4	9.1	11.1	13.9	2.7	1.4	4.0	3.2	2.2	3.5	3.6	1.1	1601
MAR	13.9	4.7	.9	1.8	6.3	5.9	6.5	9.6	14.6	6.5	1.3	5.0	6.5	4.1	4.2	7.3	.9	1054
APR	29.9	5.4	1.0	1.0	2.7	2.2	5.4	5.8	10.9	4.3	2.0	2.9	4.6	3.7	4.4	9.0	4.6	1749
MAY	18.6	1.5	.4	1.0	1.4	3.5	4.8	6.6	11.9	3.2	2.8	4.7	5.5	6.8	9.0	12.7	5.5	1847
JUN	22.9	1.7	.4	.3	1.4	2.7	9.7	11.2	9.7	2.3	1.6	2.6	3.4	3.4	10.1	13.0	3.5	1449
JUL	35.4	2.8	.1	.1	1.0	2.4	8.2	7.8	10.9	.6	.5	.9	1.2	2.9	7.2	8.9	8.2	1738
AUG	55.5	5.0	.8	.3	.8	2.2	7.6	8.2	5.1	.8	.3	.3	.7	.3	1.1	5.7	3.8	1067
SEP	36.2	12.4	1.4	2.3	2.3	1.8	3.6	12.1	10.8	.5	.9	.3	.3	.2	.5	4.2	10.3	660
OCT	25.1	17.1	1.0	3.0	3.5	3.2	7.9	13.2	10.8	.6	.3	1.2	.9	.0	.6	2.6	9.1	692
NOV	7.0	2.4	.8	1.2	7.6	10.1	11.1	15.9	23.0	2.4	1.1	2.4	2.4	2.7	2.4	2.1	5.2	656
DEC	2.4	1.5	.3	1.6	9.6	12.5	12.1	12.1	20.9	4.9	2.8	6.1	2.5	5.7	3.5	1.7	.1	752
TOTAL	22.1	4.2	.7	1.3	5.6	5.9	7.4	10.0	12.9	2.6	1.4	2.9	3.4	3.2	4.8	7.1	4.3	14659

WIND ROSES RUN 06/22/75 FOR YAQUINA LIGHTHOUSE

ALL DATA --14659 OBSERVATIONS

	WIND SPEED (MPS)																
DIR	0 TO 2	2 TO 4	4 TO 6	6 TO 8	8 TO 10	10 TO 12	12 TO 14	14 TO 16	16 TO 18	18 TO 20	20 TO 22	22 TO 24	24 TO 26	26 TO 28	28 TO 30	≥ 30	TOTAL	MEAN SPEED
N	2.7	3.1	3.3	2.9	3.5	2.9	2.5	1.0	.2	.0	.0	.0	0	0	0	0	22.1	7.4
NNE	2.1	1.2	.6	.1	.1	.0	.0	0	0	0	0	0	0	0	0	0	4.2	2.5
NE	.4	.2	.1	.0	0	.0	0	0	0	0	0	0	0	0	0	0	.7	2.0
ENE	.8	.3	.1	.1	.1	.1	0	0	0	0	0	0	0	0	0	0	1.3	3.0
E	1.3	1.1	1.2	.9	.6	.4	.1	0	.0	0	0	0	0	0	0	0	5.6	4.9
ESE	1.2	2.1	1.9	.5	.2	.0	.0	.0	.0	0	0	0	0	0	0	0	5.9	3.8
SE	1.7	2.6	1.4	.8	.5	.3	.1	.0	0	0	0	0	0	0	0	0	7.4	4.1
SSE	1.4	2.2	2.0	1.4	1.0	.6	.5	.4	.3	.2	.1	.0	0	.0	.0	0	10.0	6.6
S	1.3	1.7	1.8	1.6	1.5	1.6	1.3	.9	.6	.2	.2	.0	.0	.0	.0	0	12.9	8.5
SSW	.6	.4	.4	.4	.5	.3	.1	.0	.0	.0	.0	0	0	0	0	0	2.6	5.8
SW	.4	.2	.2	.3	.2	.0	.0	.0	0	0	.0	0	0	0	0	0	1.4	5.2
WSW	.7	.6	.7	.6	.2	.0	.0	0	.0	0	.0	0	0	0	0	0	2.9	4.5
W	.7	.5	.8	.6	.3	.3	.1	.0	.0	0	.0	0	0	0	0	0	3.4	5.4
WNW	.6	.7	.8	.5	.3	.2	.1	.0	0	.0	.0	0	0	0	0	0	3.2	5.1
NW	.4	.6	1.0	.7	.9	.6	.3	.1	.1	.0	0	0	0	0	0	0	4.8	7.2
NNW	1.0	1.2	1.4	1.1	1.3	.5	.4	.2	.1	.0	0	0	0	0	0	0	7.1	6.3
CALM	4.3	0	0	0	0	0	0	0	0	0	0	0	0	0	0	0	4.3	0
TOTAL	21.5	18.6	17.7	12.5	11.2	7.7	5.7	2.7	1.3	.5	.4	.1	.0	.0	.0	0	100.0	5.9

APPENDIX D

Velocity Profiles over the Model of Yaquina Head

(Scaled at 300:1)

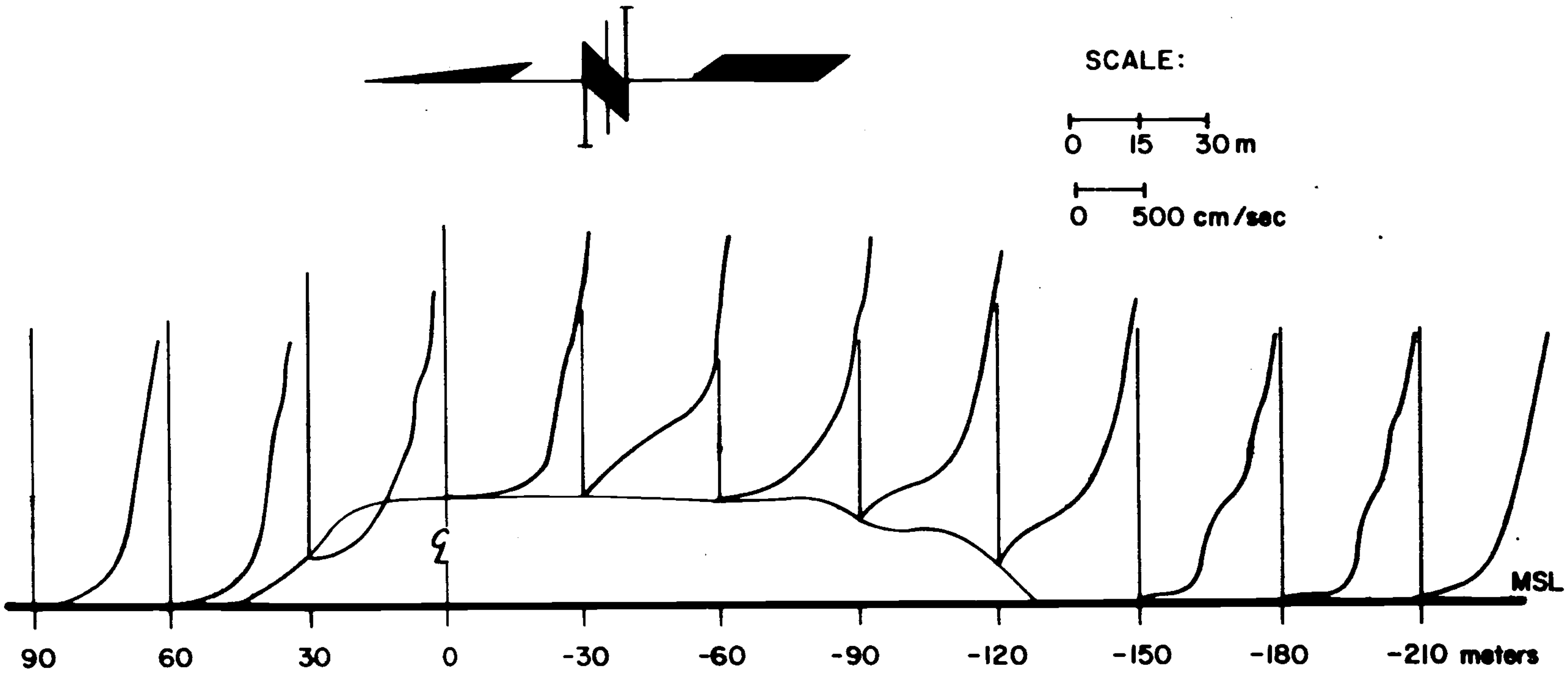

Figure D1. Velocity profiles through a north-south section at the lighthouse.

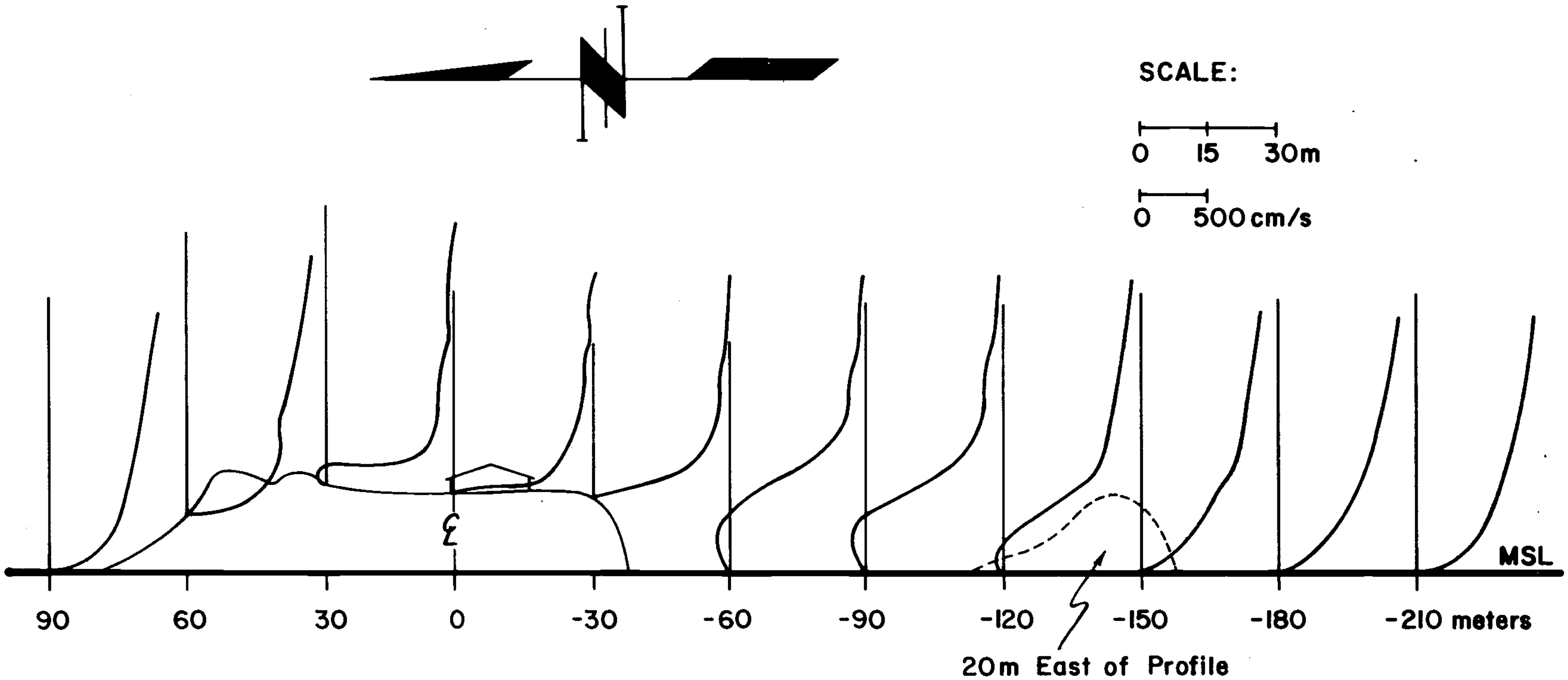

Figure D2. Velocity profiles through a north-south section 60 m east of the lighthouse.

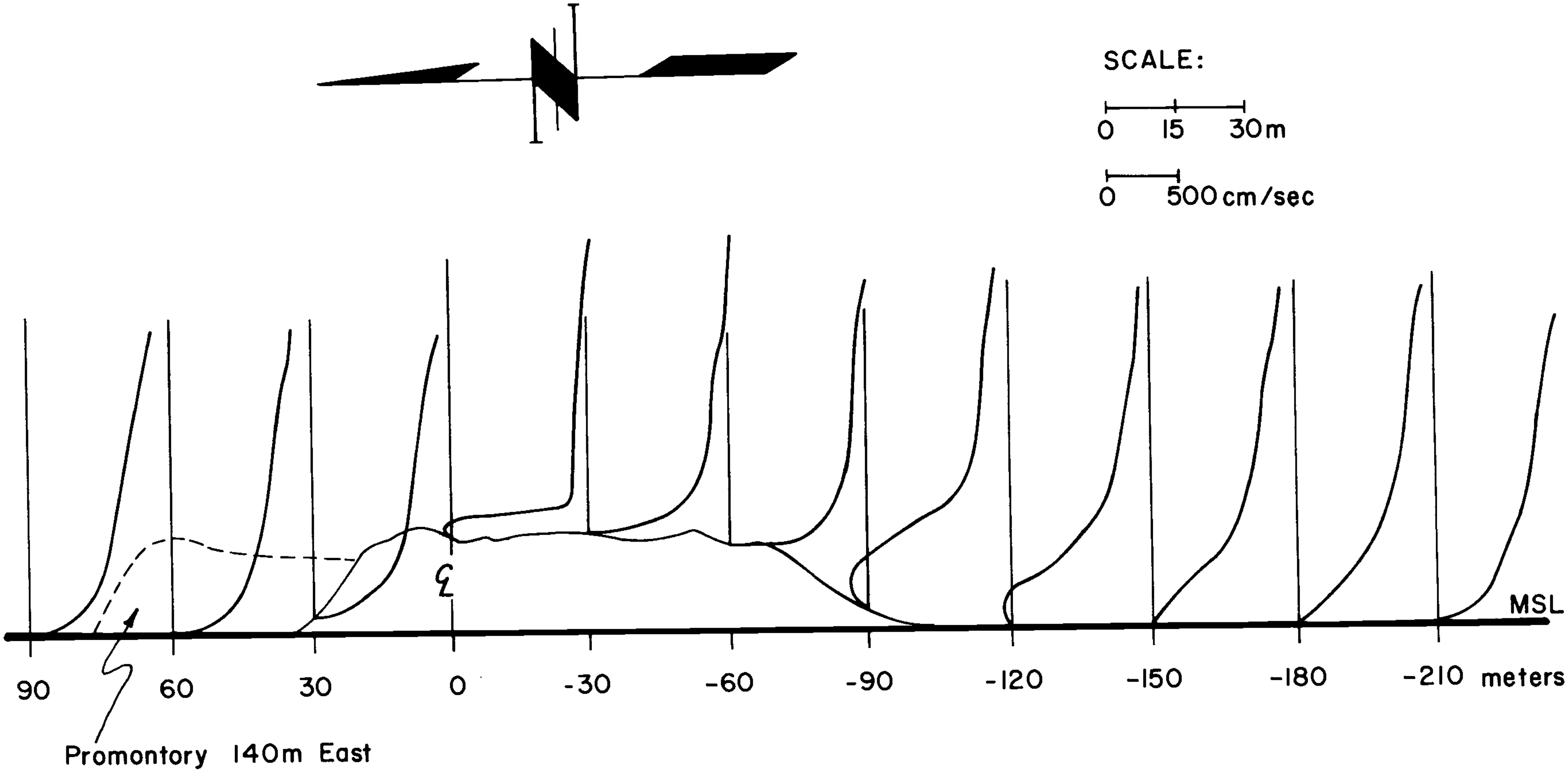

Figure D3. Velocity profiles through a north-south section 120 m east of the lighthouse.

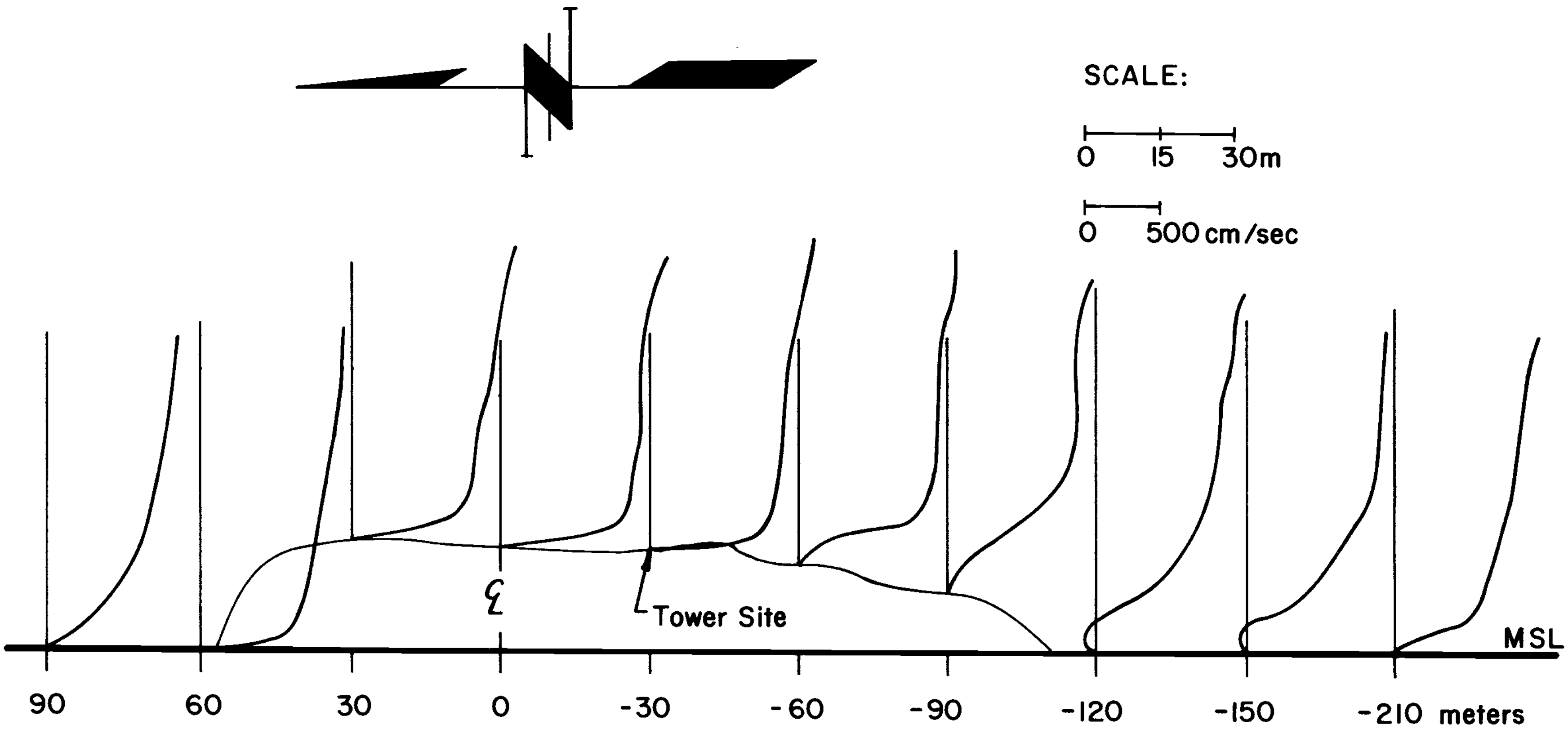

Figure D4. Velocity profiles through a north-south section 180 m east of the lighthouse.

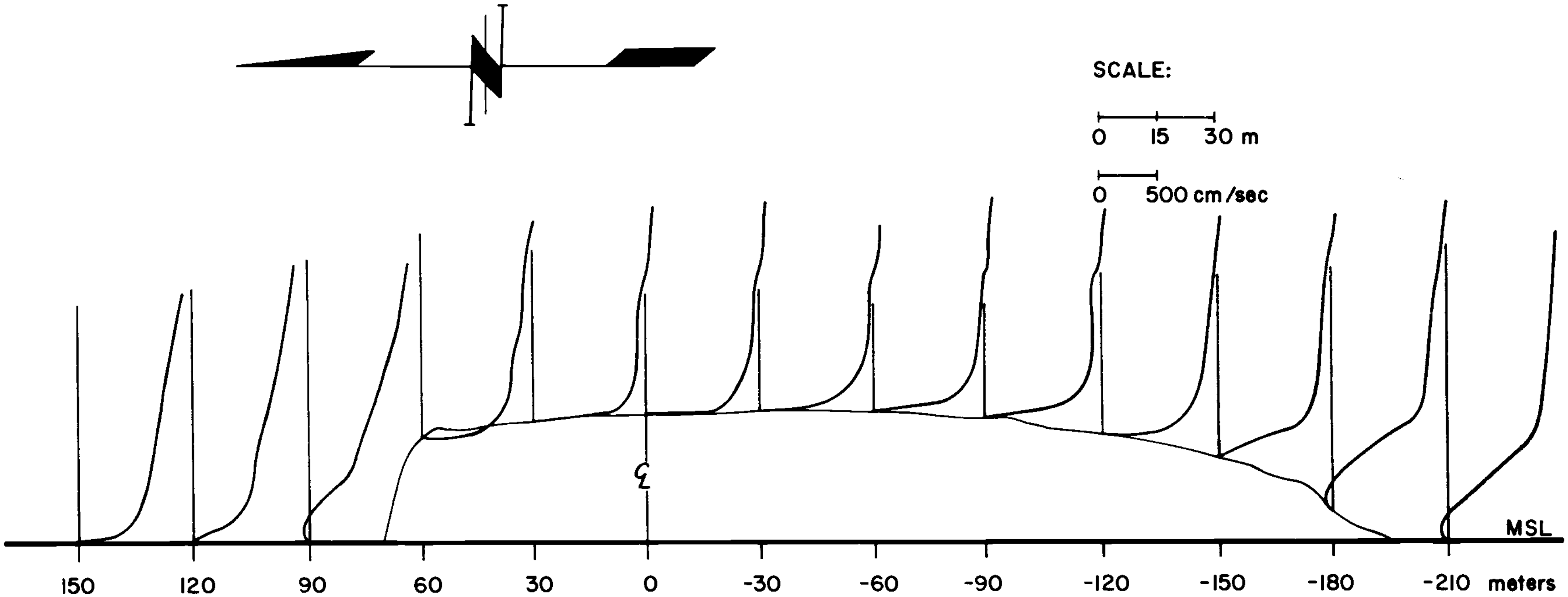

Figure D5. Velocity profiles through a north-south section 240 m east of the lighthouse.

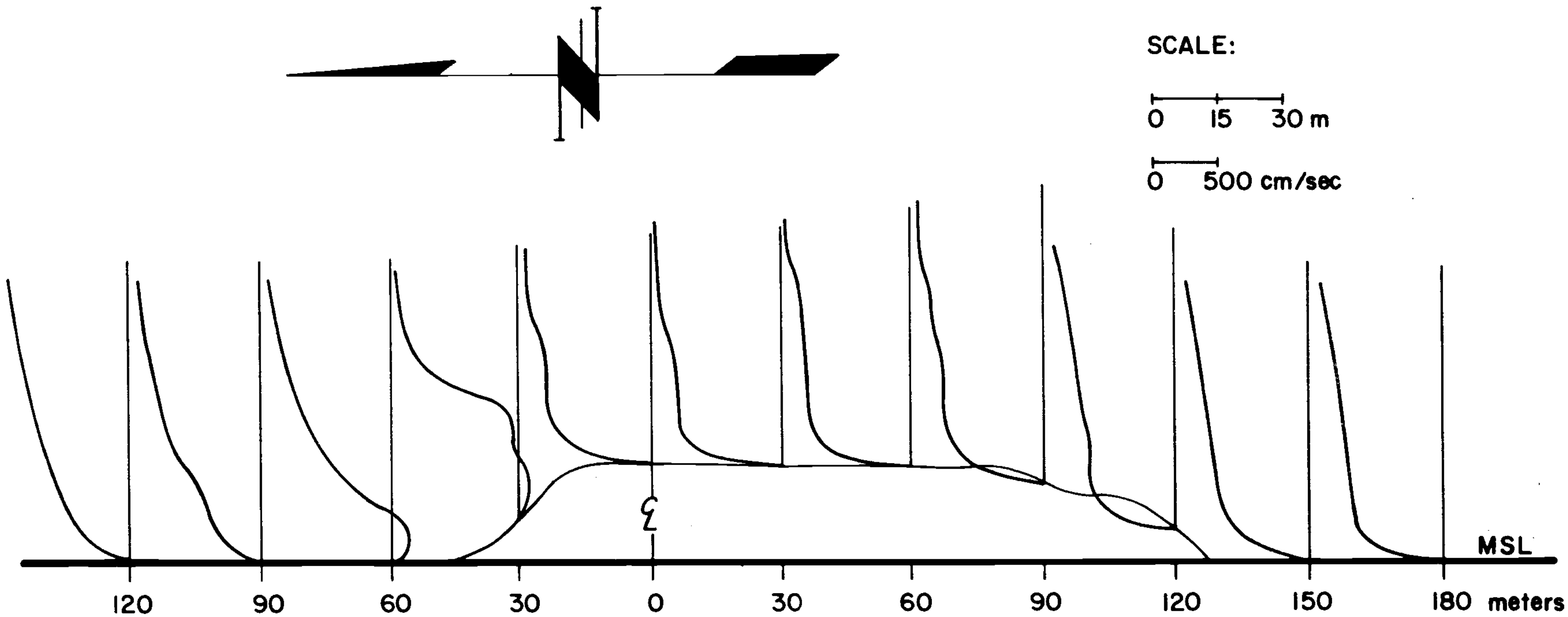

Figure D6. Velocity profiles through a north-south section at the lighthouse.

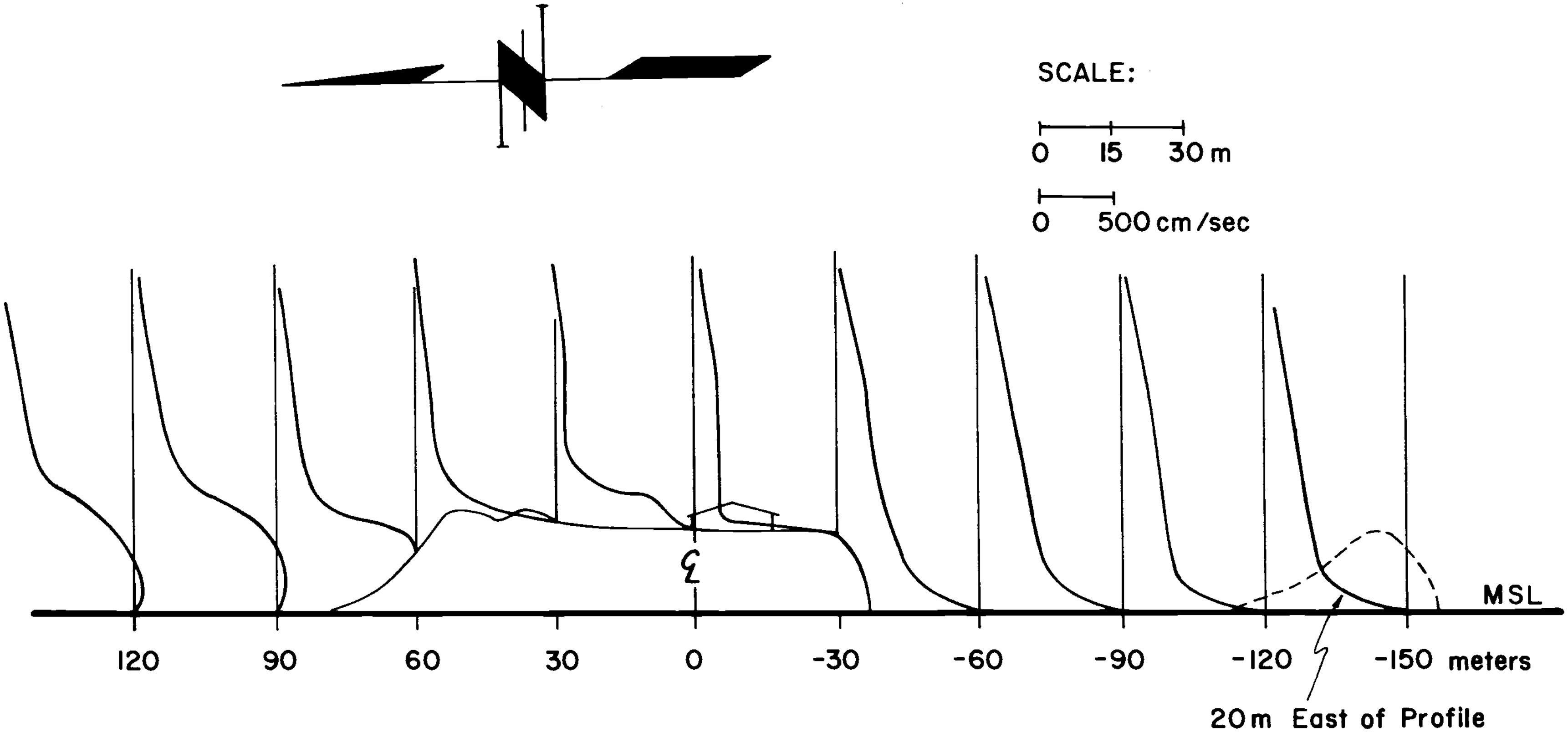

Figure D7. Velocity profiles through a north-south section 60 m east of the lighthouse.

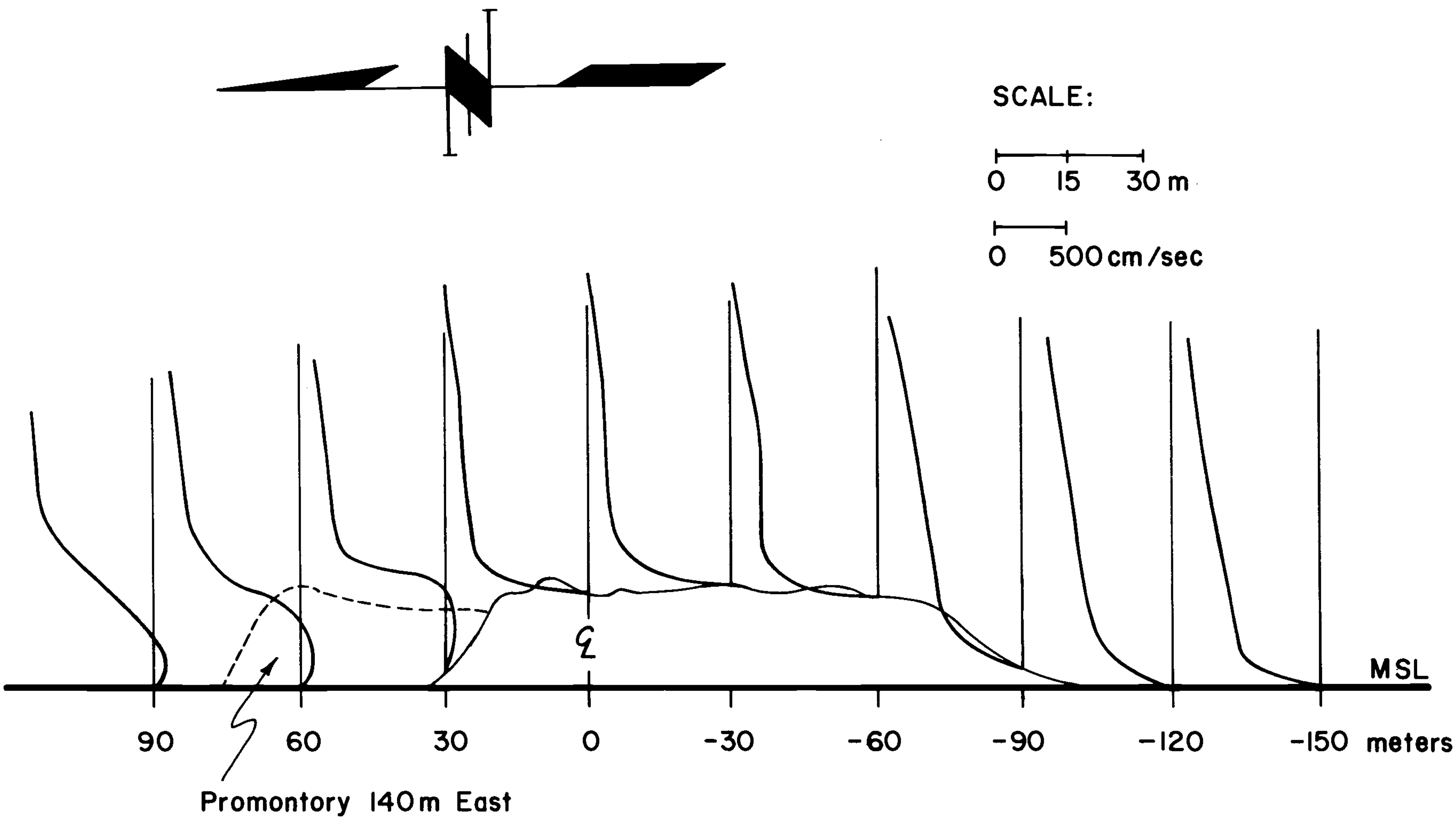

Figure D8. Velocity profiles through a north-south section 120 m east of the lighthouse.

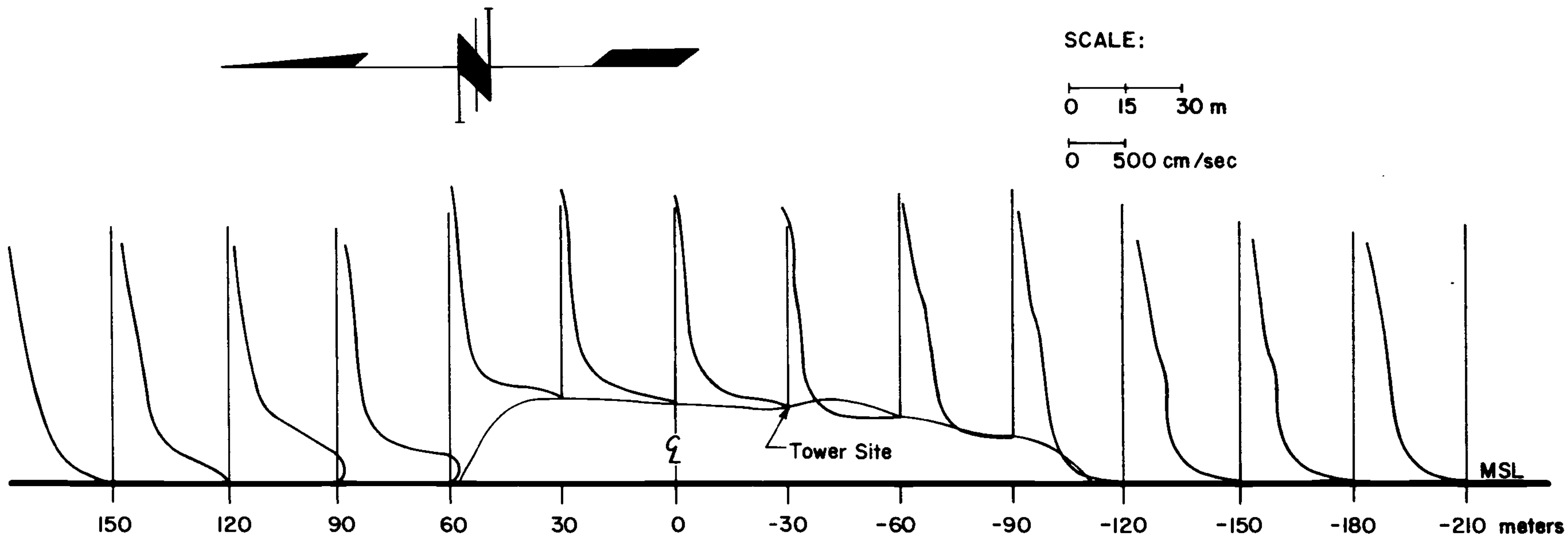

Figure D9. Velocity profiles through a north-south section 180 m east of the lighthouse.

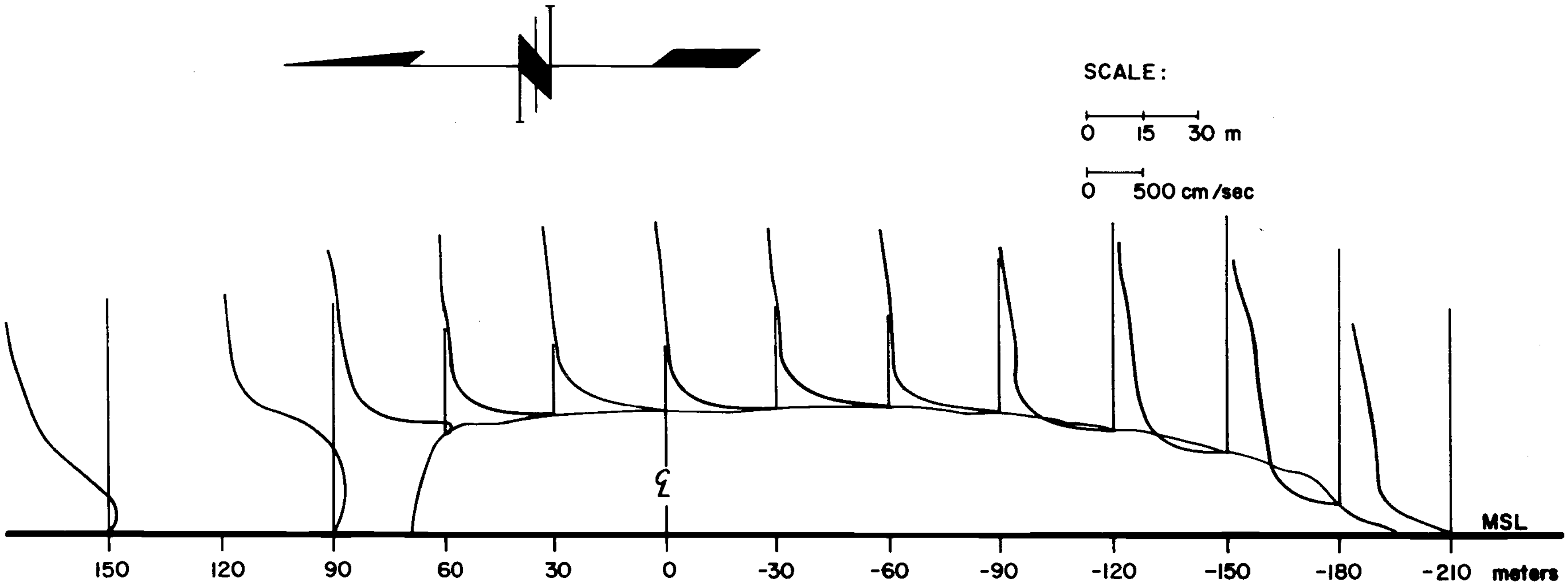

Figure D10. Velocity profiles through a north-south section 240 m east of the lighthouse.

APPENDIX E

Discussion of J. Bitte and W. Frost, "Analysis of Neutrally Stable Atmospheric Flow Over a Two-Dimensional Forward Facing Step" Presented at the AIAA 9th Fluid and Plasma Dynamics Conference, San Diego (1976)

This paper on the analysis of neutrally stable atmospheric flow over a two-dimensional step was presented at the AIAA Conference on July 16, 1976. Because of the similarity to the conditions of this experiment, comparison of results is considered an important addition to the content of the thesis.

The analysis uses the momentum and continuity equations along with the two differential equations of the closure model for the determination of the turbulence properties. The model is based on the turbulence kinetic energy concept proposed by Prandtl (41) and Kolmogorov (16) with a transport equation for the turbulence length scale.

The results of the analysis show a sharp increase in turbulent kinetic energy after the step. At the same location there is an increase in eddy size in the spreading shear layer. This is analogous to the scale of turbulence mentioned in the Yaquina model results where the scale increased from 12.8 cm over the approach flow to 17 cm over the model. Implicit in the energy increase would be some increase in energy dissipation as well as the other energy terms maintaining the turbulent energy equation. In Table 4.5, the energy dissipation is shown to increase for flow from a smooth to a rough surface.

Finally, Bitte and Frost's analysis demonstrate the change of velocity profile for flow from a smooth surface over a step. The inflection in the velocity profile varies from a height of 50% to 100% greater than the step height as the horizontal distance from the step increases. For the prototype scale, this would correspond to a height of 23 m at the tower location. Figures 4.2 and 4.3 show the location as found from the Yaquina Head data to be 20 m and for the model about 19 m.

This comparison of wind tunnel modeling to analytical modeling demonstrates the improvement of analysis with the larger computers as well as validating the results of the wind tunnel model experiment.